

**TOBB UNIVERSITY OF ECONOMICS AND TECHNOLOGY**  
**GRADUATE SCHOOL OF SCIENCE AND ENGINEERING**

**APPLICATION OF EFFICIENT PHOTOELECTRODES PREPARED BY CHALCOGENIDE  
NANOPARTICLE AND CESIUM LEAD BROMIDE PEROVSKITE SENSITIZED 3D-ZNO  
NANOSTRUCTURE IN PHOTOELECTROCHEMICAL SOLAR CELLS**



**MASTER OF SCIENCE THESIS**  
**Mehrdad FARAJI**

**Department of Micro and Nanotechnology**

**Thesis Supervisor: Prof. Dr. Nurdan DEMIRCI SANKIR**

**DECEMBER 2019**



Approval of the Graduate School of Science and Technology

.....  
**Prof. Dr. Osman Erođul**  
Director

I certify that this thesis meets all the requirements of the master's degree.

.....  
**Prof. Dr. Nurdan Demirci Sankir**  
Head of Department

Mehrdad Faraji, a M.Sc. student of TOBB University of Economics and Technology Graduate School of Engineering and Science Student ID 171611027, successfully defended the thesis entitled "APPLICATION OF EFFICIENT PHOTOELECTRODES PREPARED BY CHALCOGENIDE NANOPARTICLE AND CESIUM LEAD BROMIDE PEROVSKITE SENSITIZED 3D-ZNO NANOSTRUCTURE IN PHOTOELECTROCHEMICAL SOLAR CELLS", which he prepared after fulfilling the requirements specified in the associated legislations, before the jury whose signatures are below.

**Thesis Supervisor:** **Prof. Dr. Nurdan Demirci Sankir** .....  
TOBB University of Economics and Technology

**Jury Member:** **Prof. Dr. Mehmet Parlak (Head)** .....  
Middle East Technical University

**Dr. Ogr. Uyesi Zeynep Tutumlu** .....  
TOBB University of Economics and Technology

**Prof. Dr. Nurdan Demirci Sankir** .....  
TOBB University of Economics and Technology



## THESIS NOTIFICATION

I hereby declare that all the information provided in this thesis has been obtained with rules of ethical and academic conduct and has been written in accordance with thesis format regulations. I also declare that, as required by these rules and conduct, I have fully cited and referenced all material and results that are not original to this work.



Mehrdad Faraji



## ÖZET

### FOTOELEKTROKEMİK GÜNEŞ HÜCRELERİNDEKİ KOLOJENİD NANOPARTİKLE VE CESIUM LEAD BROMİD PEROVSKİT SENSİTİZ 3D-ZNO NANOSTRUCTURE'İN HAZIRLAYAN ETKİLİ FOTOELEKTROD UYGULAMALARI

Mehrdad Faraji

TOBB Ekonomi ve Teknoloji Üniversitesi  
Fen Bilimleri Enstitüsü  
Mikro ve Nanoteknoloji

Danışman: Prof.Dr. Nurdan Demirci Sankır

Tarih: Aralık 2019

Bu tezde, kimyasal banyo biriktirme (CBD) yöntemi kullanılarak flor katkılı kalay oksit (FTO) kaplı cam üzerine çiçek ve denizkestanesi benzeri üç boyutlu (3D) morfolojileri olan çinko oksit (ZnO) tabakaları büyütülmüştür. Daha sonra 3D-ZnO üzerine aynı yöntemle nanoyapılı kadmiyum sülfür (CdS) ve kadmiyum selenür (CdSe) tabakası büyütülmüştür. CdS ve CdSe kalkojen yapılara ek olarak, hazırlanan tezde ZnO nanoyapıların kurşun bromür perovskit ( $\text{CsPbBr}_3$ ) ile heteroeklemlerinin oluşturulması üzerine çalışılmıştır. Tüm bu heteroeklem yapılar, fotoelektrokimyasal güneş pillerinde fotoaktif elektrot olarak kullanılmıştır. Tez kapsamında CdSe ve CdS katmanlarını optimize etmek için ZnO / CdSe ve ZnO / CdS / CdSe yapısı 200 ° C'de 2 saat termal tavlama işlemine tabi tutularak performanslarının arttığı saptanmıştır. Üretilen tüm yapılar X-ışını fotoelektron spektroskopisi (XPS), x-ışını kırınım spektroskopisi (XRD), Uv-vis ve fotoluminesans (PL) spektroskopileri, kullanılarak analiz edilmiştir. Bunlara ek olarak üretilen morfolojiler ve kompozisyonları taramalı elektron mikroskopisi (SEM), geçirimli elektron mikroskopisi (TEM) ve enerji dağıtıcı X-ışını (EDX) ile analiz edilmiştir. İncefilmlerin başarı ile büyütüldüğü bu analizler sonucunda kanıtlanmış ve elde edilen buğuların literatüre paralel olduğu görülmüştür.

Son olarak sentezlenen yapılar fotoelektrokimyasal güneş pili su ayırma sisteminde fotoanot olarak kullanılmıştır. Bu sistemin ana amacı güneş ışığını kullanarak suyun elektroliz edilmesi ve hidrojen üretilmesidir. Çıplak ZnO ve ZnO-CdS-CdSe elektrotlarının dış kuantum verimliliği (IPCE) sırasıyla %12 ve %51 olarak hesaplanmıştır. Ayrıca, ZnO- $\text{CsPbBr}_3$  fotoelektrotların maksimum IPCE'si yaklaşık % 37 olduğu saptanmıştır. Bu veriler, çalışmamızda hazırlanan heteroeklem bazlı elektrotların, güneş enerjisi kullanılarak su ayrıştırılması sistemlerinde kullanmaları için çok ümit verici olduğunu göstermiştir.

**Anahtar Kelimeler:** ZnO, CdS, CdS,  $\text{CsPbBr}_3$ , Hidrojen, PEC, IPCE.





## ABSTRACT

### APPLICATION OF EFFICIENT PHOTOELECTRODES PREPARED BY CHALCOGENIDE NANOPARTICLE AND CESIUM LEAD BROMIDE PEROVSKITE SENSITIZED 3D-ZNO NANOSTRUCTURE IN PHOTOELECTROCHEMICAL SOLAR CELLS

Mehرداد Faraji

TOBB University of Economics and Technology  
Graduate School of Science and Technology  
Micro and Nanotechnology

Thesis Advisor: Prof. Dr. Nurdan Demirci Sankir

Date: December 2019

In this thesis, nanostructured zinc oxide (ZnO) layer with flower and urchin-like 3D morphologies have been deposited on fluorine-doped tin oxide (FTO) coated glass using chemical bath deposition (CBD) method. Then a thin layer of nanostructured cadmium sulfide (CdS) and selenide (CdSe) have been deposited on 3D ZnO with the same method. Additionally, a lead bromide perovskite (CsPbBr<sub>3</sub>) layer structure has been fabricated on the ZnO layer via spin coating method with the aim of the utilization of these material in to photoelectrochemical water splitting device as photo anode. Moreover, to modify the cadmium selenide layers, two ZnO/CdSe and ZnO/CdS/CdSe structures have been treated by thermal annealing at 200° C for 2 hours. As a result, the crystalline structure of the photoanodes was modified significantly. The structures also were analyzed using X-ray photoelectron spectroscopy (XPS), x-ray diffraction patters (XRD), Uv-vis and photoluminescence (PL) spectroscopies, finally the morphologies and compositions were analyzed with scanning electron microscopy (SEM) and transmission electron microscopy (TEM), and energy dispersive X-ray (EDX). The substrates were proven by the mentioned analysis and compared with other works in literature.

Then the synthesized structures were used as photoanode in the photoelectrochemical solar cell water splitting system. The aim of the system was the production of hydrogen from splitting water molecules using sunlight. The incident photon-to-charge carrier efficiency (IPCE) efficiency of the bare ZnO and ZnO-CdS-CdSe electrodes have been calculated as 12% and %51, respectively. Moreover, the maximum IPCE of the ZnO-CsPbBr<sub>3</sub> photoelectrode was approximately 37%. These data indicated that the heterojunction based electrodes prepared in this study are very promising in order to utilize them into solar water splitting systems.

**Key Words:** ZnO, CdS, CdS, CsPbBr<sub>3</sub>, Hydrogen, PEC, IPCE.



## ACKNOWLEDGEMENT

Thanks God, which created everything and lead us to the best targets, I would like to express my gratitude to my leader Imam Al-Mahdi the best leader of societies. I believe that my father's soul and older brother's soul become happy by seeing my successes in my life. I would like to thank my lovely mother and sister for their help and wisely advisors for overcoming difficulties. Thanks to dear Prof. Dr. Nurdan Demirci Sankir and Prof. Dr. Mehmet Sankir for their supports and scientific advisors which led this M.Sc. thesis to complete. And also thanks to TOBB University of Economics and Technology for M.Sc. scholarship and financial supports.

December 2019

Mehrdad Faraji  
(Nano Scientist)



## CONTENTS

	<u>Pages</u>
ÖZET.....	vii
ABSTRACT.....	ix
ACKNOWLEDGEMENT .....	xi
CONTENTS .....	xiii
LIST OF FIGURES.....	xvii
LIST OF TABLES .....	xxi
LIST OF ABBREVIATIONS.....	xxiii
LIST OF SYMBOLS.....	xxv
<b>1. INTRODUCTION.....</b>	<b>1</b>
1.1. Technology of Thin Film .....	1
1.2. Zinc Oxide .....	2
1.2.1. Growth methods .....	3
1.2.2. Stability of ZnO .....	3
1.2.3. Post growth treatment.....	4
1.2.4. Properties of ZnO .....	4
1.2.4.1. Electronic and optical properties.....	4
1.2.4.2. Catalytic properties.....	6
1.2.4.3. Hydrophobicity of the ZnO .....	6
1.2.4.4. ZnO field emission characterization .....	7
1.2.4.5. Photonic crystals.....	9
1.2.4.6. Photoluminescence (PL) of ZnO.....	10
1.2.5. Applications of nanostructured ZnO .....	11
1.2.5.1. Electrochromic displays .....	11
1.2.5.2. ZnO structure in field-effect transistors .....	12
1.2.5.3. Sensors.....	13
1.2.5.4. Solar cells applications of ZnO .....	15
1.2.5.5. Hydrogen generation via water splitting .....	16
1.3. Cadmium Chalcogenide Nanostructures.....	17
1.3.1. Cadmium sulphide (CdS) .....	18
1.3.2. Cadmium selenide (CdSe).....	18

1.3.3.	Synthesis of chalcogenide nanostructures.....	18
1.3.3.1.	Colloidal synthesis method.....	19
1.3.3.2.	High temperature injection .....	20
1.3.3.3.	Hydrothermal/Solvothermal process .....	21
1.3.3.4.	Microwave irradiation-assisted synthesis .....	22
1.3.3.5.	Sonochemical process.....	22
1.3.3.6.	Capping-Assisted synthesis.....	23
1.3.4.	Applications of metal chalcogenide nanostructures.....	23
1.4.	Halide Perovskites .....	24
1.4.1.	Properties of perovskites .....	27
1.4.2.	Perovskite nanostructure synthesis .....	29
1.4.3.	Applications of nanostructure perovskites .....	29
1.4.3.1.	Photovoltaics applications of perovskites .....	29
1.4.3.2.	Application beyond photovoltaic.....	31
1.4.3.2.1.	Photodetectors .....	31
1.4.3.2.2.	Light emitting diodes (LEDs) and laser.....	33
1.5.	Principles of Photoelectrochemical (PEC) Cells.....	35
1.5.1.	Thermodynamics of photoelectrochemical and photocatalytic water splitting .....	36
<b>2.</b>	<b>SYNTHESIS AND CHARACTERIZATION OF FABRICATED SEMICONDUCTOR .....</b>	<b>39</b>
2.1.	Chemical Synthesis of Nanostructured Thin Film.....	39
2.2.	Chemical Bath Deposition (CBD) Synthesis Method .....	39
2.3.	Synthesis of the Nanostructured Thin Film Via Spin Coating.....	40
2.4.	Experimental Semiconductor Synthesis.....	41
2.4.1.	Nanostructured ZnO .....	41
2.4.2.	ZnO/CdS structure fabrication .....	42
2.4.3.	ZnO/CdSe and ZnO/CdS/CdSe structures synthesis .....	43
2.4.4.	ZnO/CsPbBr <sub>3</sub> structure synthesis.....	44
2.5.	Thermally Post Treatment of the ZnO/CdS/CdSe and ZnO/CdSe Structures .....	45
2.6.	Photoelectrochemical (PEC) System and Electrolyte .....	46
2.7.	Photoluminescence (PL) and Absorbance Spectroscopy of The Structures .....	46
2.8.	X-ray Photoelectron Spectroscopy (XPS).....	47
2.9.	X-ray Diffraction (XRD) .....	51

2.10. Scanning Electron Microscopy (SEM) and Transmission Electron Microscopy (TEM) .....	56
<b>3. RESULTS AND DISCUSSIONS.....</b>	<b>65</b>
3.1. Photoelectrochemical Device.....	65
3.2. PEC Efficiency .....	66
3.3. Findings .....	68
3.4. IPCE Results .....	71
3.5. Results for Heat Treated Cadmium Chalcogenide Structures.....	72
<b>4. CONCLUSION .....</b>	<b>77</b>
<b>REFERENCES .....</b>	<b>79</b>
<b>CURRCULUM VITAE.....</b>	<b>83</b>







## LIST OF FIGURES

	Page
Figure 1.1. Various ZnO nanostructures under SEM.....	5
Figure 1.2. (a) a spherical water droplet on nanostructure ZnO thin film after (right) and before (left) UV irradiation .....	7
Figure 1.3. (a) synthesized ZnO nanoarrays.....	8
Figure 1.4. The transmission spectrum of the ZnO nanowire arrays for both TE and TM polarizations.....	10
Figure 1.5. (a) Photoluminescence spectrum of nanostructure ZnO fabricated on the Au-coated surface. (b) Photoluminescence spectrum of thin film ZnO and nanostructure ZnO at 4.2 K.....	11
Figure 1.6. (a) The structure of the electrochromic system. (b) pictures of the system (i) before (ii) after applying bias, and (iii) at open circuit stat .....	12
Figure 1.7. (a) nanostructured ZnO transistor structure on a flexible substrate. (b) the nanostructure ZnO under SEM fabricated between the drain and source electrodes. (c) The output properties of nanostructure ZnO transistor with 10 $\mu\text{m}$ channel. The inset depicts the transconductance with respect to the gate voltage .....	14
Figure 1.8. (a) calibration plot for working and reference electrodes in a standard buffer. (b) The pH of the intracellular measurement inside a human fat cell .....	15
Figure 1.9. The diagram shows the charge and the ultrasonic vibration of the piezo potential created on a nanostructure ZnO .....	17
Figure 1.10. Schematic depicts the fabrication of thiol capped CdTe quantum dots Left depicts the formation of CdTe precursor by $\text{H}_2\text{Te}$ gas. Right depicts growth of CdTe QDs by reflux .....	20
Figure 1.11. Depicts the hot injection approach in organo-metallic fabrication of QDs nanostructures .....	21
Figure 1.12. The classification of biomedical applications of QDs.....	24

- Figure 1.13. (a) perovskite unit cell and ions. (b) schematic of a perovskite quantum dot and oleate ligands on the surface. (c) typical high-resolution (HRTEM) image of  $\text{MAPbBr}_3$  QDs perovskite d-g) TEM images of the  $\text{CsPbX}_3$  perovskite QDs with different structures, (d) nanocubes, (e) nanorods, (f) nanowires, (g) hexagonal nanoplates . 25
- Figure 1.14. (a) Representation of dielectric effects on electronic states in (i) cubic bulk perovskite and (ii) nanoplatelets. (b) Comparison between binding energy for nanoparticles (320 meV) and  $\text{MAPbBr}_3$  bulk crystals (84 meV) (c) Lead halide perovskite defect tolerance. (d) Dimension distributions of inorganic chalcogenide QDs, perovskite QDs, and perovskite nanocrystals ..... 26
- Figure 1.15. Illustration of the color tuning of the perovskite nanoplates and nanocrystals by chemical tuning as well as quantum confinement effect. (a) Colloidal  $\text{CsPbX}_3$  (X=I, Br, Cl) perovskite show composition- and size-tunable bandgap energies covering just visible region spectral with bright and narrow emission. (b) Quantum –size effects in the emission and absorption spectra of  $\text{CsPbBr}_3$ . (c) Schematic illustration of the nanoplates stacks..... 28
- Figure 1.16. (a) the formation of  $\text{CsPbX}_3$  (X=I, Br, Cl) nanoparticles mediated by amine and organic ligands. (b) Effect of reaction temperature at (i) 150°C, (ii) 130°C, (iii) 90°C. (iv) The nanostructure film templates for nanoporous silicon and alumina infused with perovskite nanoparticles with SEM. (d) Schematics illustration of core-shell of octyl ammonium lead bromide nanomaterials over  $\text{MAPbBr}_3$  nanoparticles. (e) TEM images of nanostructures, and the perovskite suspension under UV light, and UV-vis and photoluminescence spectra of perovskite ..... 30
- Figure 1.17. Applications of photovoltaic halide perovskite. (a) A model plane powered by metal halide perovskite photovoltaics. (b) Picture of a normal colored semitransparent perovskite film fabricated on glass using controlled dewetting. (c) Photonic crystal scaffolds with colorful perovskite solar cells..... 32
- Figure 1.18. Perovskite photodetectors. (a) the device structure of perovskite photodetector. (b) Bandgap energy diagram perovskite photodetector. (c) UV-vis absorption spectra of the photodetector without the Al layer and hole-blocking layer. .... 34
- Figure 1.19. Sandwiched structure and energy level schematic of perovskite LED. (a) The device structure of the  $\text{MAPbI}_{3-x}\text{Cl}_x$ . (b) Energy level schematic of different layers of materials in the infrared perovskite LED, depicting valence and conduction bandgap with respect to vacuum..... 34
- Figure 1.20. Light emission from perovskite films. (a) Photoluminescence spectra of  $\text{MAPbI}_3$  film using 1 kHz pumping pulse with increasing fluence of the pump, an illustration of

transporting from simultaneous emission to amplified simultaneous emission. (b) The FWHM of the average transition photoluminescence lifetime and emission peak with respect to pump fluence. (c) Photoluminescence intensity with respect to pump fluence. The amplified simultaneous emission threshold fluence ( $P_{th}^{ASE}$ ) and the trap state saturation threshold fluence ( $P_{th}^{trap}$ ) .....	35
Figure 1.21. Water splitting reaction on a heterogeneous photocatalyst. (a) sunlight absorption, (b) charge transfer, (c) redox reactions, (d) desorption, adsorption, and mass diffusion of species, and (e) charge recombination.....	37
Figure 1.22. Energy diagrams of photocatalytic water splitting on (a) one step excitation, (b) two-step excitation or Z-scheme, and water splitting using PEC (c) photoanode, (d) photocathode, (e) tandem device.....	38
Figure 2.1. CBD synthesis of nanostructured layers, with the system components .....	40
Figure 2.2. (a) ZnO nanostructured on FTO, (b) ZnO synthesis solution .....	42
Figure 2.3. The ZnO structure (left) and CdS layer synthesized on ZnO structure (right) ...	43
Figure 2.4. (a) the left structure of ZnO/CdS/CdSe and the right ZnO/Cd, (b) CdSe synthesis solution.....	44
Figure 2.5. The ZnO/CsPbBr <sub>3</sub> structure .....	45
Figure 2.6. The schematic of experimental PEC process. The left device is the AM1.5 light Source.....	46
Figure 2.7. The absorption spectrum of the synthesized structures .....	48
Figure 2.8. The PL spectrum of the synthesized structures .....	48
Figure 2.9. The absorption spectrum related to the CsPbBr <sub>3</sub> perovskite .....	49
Figure 2.10. The PL spectrum related to the CsPbBr <sub>3</sub> perovskite .....	49
Figure 2.11. The schematic related to a photoelectron emitting due to an incident.....	50
Figure 2.12. (a) the ZnO structure XPS survey spectrum, (b) Zn 2p, and (c) O 1s.....	52
Figure 2.13. (a) the ZnO/CdS structure XPS survey spectrum, (b) Cd 3d, and (c) O2p .....	53
Figure 2.14. (a) the ZnO/CdSe structure XPS survey spectrum, (b) Se 3d .....	54
Figure 2.15. The ZnO/CdS/CdSe structure XPS survey spectrum .....	55
Figure 2.16. The XRD patterns of structures.....	56
Figure 2.17. The SEM images of ZnO nanostructures with scale bars of (a) 100 μm, (b)20 μm, (c) 5 μm, and (d) 2 μm.....	57
Figure 2.18. The nanostructured ZnO under SEM with scale bars of (a)100 μm, (b)20 μm, (c) 5 μm .....	58
Figure 2.19. The SEM images of ZnO/CdSe nanostructures with scale bars of (a) 100 μm, (b)	

20 $\mu\text{m}$ , (c) 5 $\mu\text{m}$ , and 2 $\mu\text{m}$ .....	59
Figure 2.20. The SEM images of ZnO/CdS nanostructures with scale bars of (a) 100 $\mu\text{m}$ , (b) 20 $\mu\text{m}$ , (c) 5 $\mu\text{m}$ , and 2 $\mu\text{m}$ .....	60
Figure 2.21. The SEM images of ZnO/CdS/CdSe nanostructures with scale bars of 100 $\mu\text{m}$ .....	61
Figure 2.22. The SEM images of ZnO/CsPbBr <sub>3</sub> nanostructures with scale bars of 100 $\mu\text{m}$ ..	62
Figure 2.23. The TEM images of ZnO structures with scale bar of (a) 100 nm, (b) 50 nm, (c) 20 nm, (d) 10 nm, (e)5 nm, and (f)5 nm.....	63
Figure 2.24. The TEM images of ZnO/CdSe structures with scale bar of (a) 100 nm, (b) 50 nm, (c) 20 nm, (d) 10 nm, (e) 5 nm, and (f) 5 nm.....	63
Figure 2.25. The TEM images of ZnO/CdS structures with scale bar of (a) 50 nm, (b) 10 nm, (c) 5 nm .....	64
Figure 3.1. The J-V curves of photoanode structures.....	69
Figure 3.2. The APBE performance of untreated structures .....	70
Figure 3.3. The stability of the photoanode structures .....	71
Figure 3.4. The responsivity of the structures .....	72
Figure 3.5. The IPCE of untreated structures.....	73
Figure 3.6. The J-V curve of the treated ZnO/CdSe structure.....	73
Figure 3.7. The J-V curve of the treated ZnO/CdS/CdSe structure .....	74
Figure 3.8. The APBE performances of treated structures .....	74
Figure 3.9. The IPCE of the treated structures.....	75
Figure 3.10. The IPCE of the ZnO/CsPbBr <sub>3</sub> structure .....	75
Figure 3.11. The XRD pattern of ZnO/CdSe for treated and untreated structures.....	76

## LIST OF TABLES

	<b>Page</b>
Table 2.1. Advantages and Limitation of Spin Coating Synthesis Method .....	41
Table 2.2. The elemental EDX of ZnO .....	42
Table 2.3. Elemental EDX of ZnO/CdS.....	43
Table 2.4. Elemental EDX of ZnO/CdSe.....	44
Table 2.5. The elemental EDX of ZnO/CsPbBr <sub>3</sub> .....	45



## LIST OF ABBREVIATIONS

<b>CBD</b>	: Chemical Bath Deposition
<b>ALD</b>	: Atomic Layer Deposition
<b>CVD</b>	: Chemical Vapor Deposition
<b>ZnO</b>	: Zinc Oxide
<b>MOCVD</b>	: Metal Organic Chemical Vapor Deposition
<b>PVD</b>	: Physical Vapor Deposition
<b>LEDs</b>	: Light Emitting Diodes
<b>PVs</b>	: Photovoltaics
<b>SEM</b>	: Scanning Electron Microscopy
<b>PL</b>	: Photoluminescence
<b>IR</b>	: Infrared
<b>ITO</b>	: Indium Tin Oxide
<b>FTO</b>	: Fluorine Doped Tin Oxide
<b>FETS</b>	: Field Effect Transistors
<b>PEC</b>	: Photoelectrochemical
<b>CdS</b>	: Cadmium Sulfide
<b>CdSe</b>	: Cadmium Selenide
<b>CdTe</b>	: Cadmium Telluride
<b>QDs</b>	: Quantum Dots
<b>HRTEM</b>	: High Resolution Transmission Electron Microscopy
<b>CsPbBr<sub>3</sub></b>	: Cesium Lead Bromide
<b>PLQY</b>	: Photoluminescence Quantum Yield
<b>GaAs</b>	: Gallium Arsenide
<b>VB</b>	: Valence Band
<b>CB</b>	: Conduction Band
<b>EDX</b>	: Energy Dispersive X-ray
<b>XPS</b>	: X-Ray Photoelectron Spectroscopy
<b>XRD</b>	: X-Ray Diffraction
<b>STH</b>	: Solar-to-Hydrogen
<b>IPCE</b>	: Incident Photon-to-Current Conversion Efficiency
<b>ABPE</b>	: Applied Bias-to-Photon Efficient





## LIST OF SYMBOLS

Symbols	Explanations
$E_{\text{local}}$	Electric Field
$\beta$	Field Enhanced Factor
$\Phi$	Work Function
$C_{\text{ox}}$	Gate Capacitance
$h$	Planck Constant
$E_k$	Delocalized Energy
$E_B$	Electron Binding Energy
$E_{\text{ref}}^0$	Electrode Potential
$E_{\text{ref}}$	Working Electrode Potential
$E_{\text{RHE}}$	Working Electrode Potential Against the Electrolyte
$P_{\text{light}}$	Sun Light Energy Flux
$\lambda$	Light Wavelength
$I_{\text{ph}}$	Generated Photocurrent Density
$V_{\text{Ag/AgCl}}$	Applied Voltage
$E_{\text{Ag/AgCl}}^0$	Reference Electrode



# 1. INTRODUCTION

## 1.1. Technology of Thin Film

Generation of electricity by controlling sunlight energy has been illustrated one of the solutions to the energy problems on a global scale. However, in order to compete with conventional sources, the solar device must be cost-effective and reliable. Various solar technologies including thin film, organic, and wafer have been investigated to achieve high efficiency, cost-effectiveness, and reliability with huge success. For example, crystalline silicon has been scaled up from laboratory to commercial very successfully and becomes 90% of the global solar device market [1]. To be cost effective, energy conversion efficiency should be increased, while less material is using. Instead of wafer technology meeting high efficiency, a thin film can convince the minimum amount of material usage in solar devices as well. During the past decade, novel thin film solar device technologies such as organic and dye-sensitized, zinc oxide, most recently perovskite photovoltaics and so on have been increasing with respect to device efficiency and stability. All thin film technologies depicted efficiency rises which are similar to crystalline silicon during the last decay [2]. The crystalline silicon has not been attained any lead over the technology of thin film. By the combination of single cells into multi-junction cell devices, the damage effects of light-induced degradation on the cell can be decreased dramatically. Therefore, the p-i-n structures tolerate less from set difficulties, even if the defect densities are developed. Since, in the p-i-n structures, an electric field dominant in the i-type section layer is promoted, and the set is gradually enhanced. Multi-junction structures pose a high light-harvesting potential in the solar spectrum because the bandgap energies of the single components are adjustable. In addition, compare to traditional solar devices such as crystalline silicon solar devices, the operation mechanism of many thin film solar devices technologies is in function of complex physical principles, such as functional material interfaces, charge separation, photoinduced, and excitonic processes [3]. Thin film technology has potential applications in energy conversion, harvesting and storage, because of their high performance, effective cost, and manufacturability. Thin film electrodes can be utilized in a wide variety of fields, such as photovoltaics, supercapacitor devices, fuel cells, rechargeable metal ion batteries and so on

[4]. Thin film materials could be manufactured by different approaches including chemical bath deposition (CBD), electrochemical deposition, thermal evaporation, atomic layer deposition (ALD), chemical vapor deposition (CVD), molecular beam epitaxy (MBE), pulsed laser deposition (PLD) and so on. By harnessing thin film manufacturing techniques, thin film electrodes with favorable properties can be obtained and the electrodes employed toward enhancing the performance of devices via an understanding of the performance structure and property correlations.

## **1.2. Zinc Oxide**

Zinc oxide (ZnO) is a wide band gap semiconductor (3.3 eV). It has a higher exciton binding energy of 60 mV at room temperature with respect to other semiconductors. Its crystalline structure is wurtzite and it is a piezoelectric material and it has been studied in the form of single-crystal (bulk form) for decades [5]. Investigation in ZnO topics is still a controversial issue since there are unresolved issues concerning this material. ZnO nanostructure can be synthesized in a range of different morphologies and by a variety of methods, therefore it is of intense interest on a global scale. The wide varieties synthesis methods include CBD [6], wet chemistry [7], hydrothermal [8], electrospinning [9], flux method [10], sputtering [11], PLD [12], MBE [13], metal-organic chemical vapor deposition (MOCVD) [14], physical vapor deposition (PVD) [15], and top-down method using etching technology [16]. Among these methods, chemical methods such as CBD and wet chemistry synthesis are significant for some reasons: first of all they are capable of easy scaling up, low cost, and less hazardous. This method is compatible with flexible and organic materials; the growth occurs at a relatively low temperature; it can be combined with silicon technology, and there is no need for metal catalysts [17]. In chemical methods, the morphology and properties of ZnO nanostructures can be effectively controlled [18]. The flux and PVD techniques usually require high temperatures and impurities and catalysts can easily incorporate into the ZnO framework. Therefore, these methods are less likely to use in integrating with organic materials for flexible electronics. However, while metal-organic chemical vapor deposition and molecular beam epitaxy can produce a highly crystalline quality ZnO nanostructure, it has disadvantages including expensive, limited choice of material, low productivity yield, and poor deposition uniformity. Therefore, they are less adopted. The sputtering PVD, and PLD methods have less reproducibility and controllability with respect to other methods. Because of the highly polar surface of the wurtzite ZnO crystalline structure, it can grow in different nanostructures morphologies [19] including nanoflower [20], nanowire [21], astray [22], nanorods [23], nanobowls [24], nanospring [25], nanorings [26], nanobelts [27], nanohelics

[28]. Figure 1.1 depicts various morphologies of ZnO nanostructures. ZnO has potential applications in electronics and optoelectronics industries including light-emitting diodes (LEDs), photovoltaics (PV), photodetectors, laser, transistors, a catalyst for photoelectrochemical hydrogen production, sensors, and active elements in sunscreens, and so on.

### **1.2.1. Growth methods**

Nanostructured ZnO can be fabricated by different methods, from simple to vacuum-based, low temperature, and low-cost approaches. Due to high defect chemistry, several optical and electronic properties have been observed for different nanostructured ZnO. There are very few controversial issues on the growth of undoped nanostructured ZnO. Since, there is a relationship between native defect concentration, growth conditions and measured properties which are not often clear. There are several aspects of the fabrication, including the use of seeding layer, metal catalysts, and so on. There is an unresolved problem for the vapor-phase fabrication of nanostructured ZnO. Two of them are the lateral position control and the size of the nanostructured ZnO on the substrates. To pattern, the substrate with multiple nanorods, the lithography method can be employed. But, to control the position of single nanorods, the feature size is too large. Self-assembly also can be used to pattern the ZnO nanostructures which is a simple and fast approach. For example, ZnO nanorod has been fabricated successfully by a self-assembled layer of polystyrene spheres [30]. The second issue related to the fabrication of nanostructured ZnO is controlling the doping ZnO nanostructures. Additionally, nanostructures ZnO should be strictly banned from exposure to the ambient. To prevent artifact and erroneous results, the characterization should be implemented on freshly prepared samples because of the time-dependent properties. The ZnO is sensitive to exposure to ambient. Because the humidity of the ambient affects the crystallinity and fabrication of ZnO nanostructures. It is also sensitive to the exposure to light and dry oxygen gas because of the persistent photoconductivity.

### **1.2.2. Stability of ZnO:**

To avoid instability of the film properties, it is necessary to passivate ZnO with layers, especially for the p-type ZnO. The storage time, light exposure, and ambient humidity should be considered when characterizing ZnO nanostructures.

### **1.2.3. Post growth treatment**

The properties of ZnO can be improved by post-growth treatments including hydrothermal treatment and annealing in different environments at high temperatures. The optical properties of ZnO can significantly change with both treatments. The hydrothermal treatments which are an excellent to traditional annealing implemented at the same time for the same temperature. The promotion in nanostructure ZnO properties occurs because of the reaction between native defects and water during the treatment causing a very big improvement for the defect formation. Since ZnO is sensitive to water vapor it is necessary to carefully control the time of treatment and water vapor pressure for optimal results [31].

### **1.2.4. Properties of ZnO**

Because of the unique chemical and physical characterizations, the nanostructured ZnO has potential applications in different areas.

#### **1.2.4.1. Electronic and optical properties**

There are several debate problems related to the electronic and optical properties of nanostructured ZnO, the most important one is being p-type doping and green emission. There are some hypotheses, and different defects which can result in energy levels of the ZnO band gap for the defect emission bands in ZnO band gap. There are two significant problems related to the electronic properties of nanostructure ZnO of p-type doping and n-type conductivity. To explain n-type conductivity and a shallow donor, while oxygen vacancy utilized to be considered as a possible candidate, it has been established that they are deep donors. In the ZnO, hydrogen is the most important shallow donor and it is also a factor for defected passivation. The hydrogen action as a shallow donor has been predicted and confirmed theoretically and experimentally for the ZnO structures, respectively. Hydrogen in nanostructure ZnO can be participated as subsurface hydrogen and bulk hydrogen, which is less bond, and it forms a complex with defects. Additionally, the stability problems and the change of properties because of the ambient and light exposure are also a problem for nanostructures, which are less stable with respect to thin films because of the high surface area. The P-type ZnO layer demonstrated stable p-type for 1 year, but n-type for 24 h. These phenomena were depicted as band bending. As a result, for p-type conductivity the presence of passivation layer for ambient protection must be considered. The protection layer also promotes the substrate properties especially optical properties of nanostructured ZnO. The charge transport and electrical properties can make a benefit from passivation.

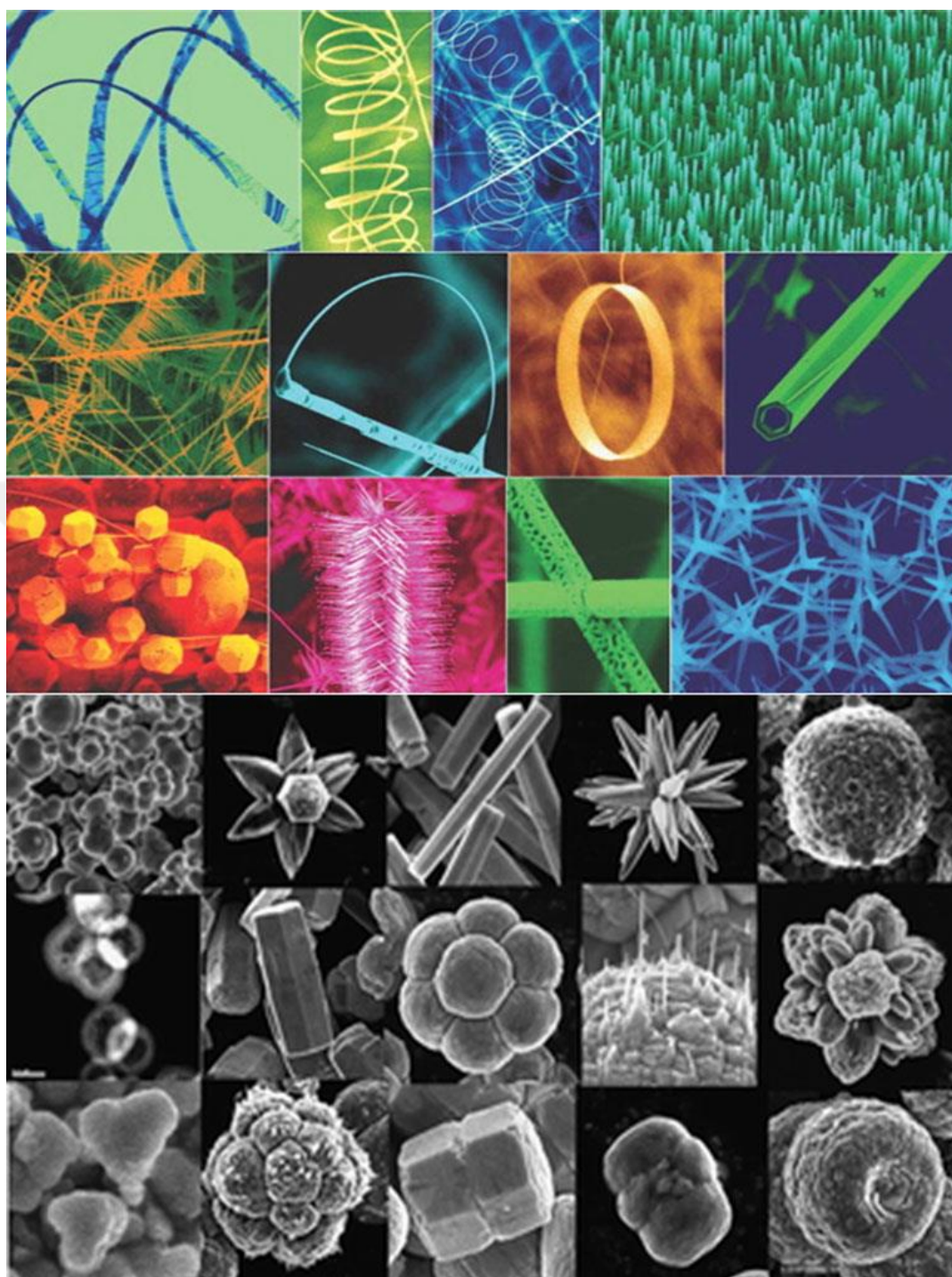


Figure 1.1 Various ZnO nanostructures under SEM [29].

#### **1.2.4.2. Catalytic properties**

Due to the low fabrication cost and large band gap of ZnO, it is received large consideration specially for the mineralization and degradation of pollutants as a photocatalyst. The ZnO generates electron and hole pairs under UV illumination which can fabricate hydrogen by splitting of water molecules, reduce graphene oxide to graphene, and synthesize H<sub>2</sub>O<sub>2</sub>. Particularly, the organic environmental pollutants can be oxidized or decomposed by generated holes, including formaldehyde, methyl blue, methyl orange, and rhodamine 6G. due to the active defect sites including the surface oxygen vacancies, ZnO can be employed as a catalyst for the production of methanol from hydrogen and carbon monoxide, and as a supporting building for different metal catalysts including copper/ferrite composites, copper oxide, cobalt, and gold, for methanol steam reforming. The nanostructured ZnO can be a perfect photocatalyst because of the huge surface to volume ratio with respect to the bulk ZnO structures. Additionally, if the length of nanostructured ZnO becomes smaller than 50 nm, the redox potential increases, the effective bandgap of ZnO increases, and therefore the photogenerated holes and electrons have a higher oxidizing/reducing power. The Large band gap energy is the main reason for recombination of the generated holes and electrons, which can promote the charge transition between the pollutants and the catalyst. To prevent the recombination for the generated hole and electron pairs and enhancing charge separation efficiency, ZnO can be combined with other nanostructures including cadmium sulfate, tin oxide, with a heterostructure array. The main drawback of nanostructured ZnO as a photocatalyst is the stability. Since it is unstable in basic and acidic media, therefore the photocatalytic activity of ZnO decreases over time due to photo corrosion under UV illumination.

#### **1.2.4.3. Hydrophobicity of the ZnO**

The surface wetting is one of the most significant factors for industry applications. There is a relationship between superhydrophobicity and superhydrophilicity of nanostructured ZnO structures by storage in dark and UV irradiation [31]. Figure 1.2 depicts a droplet on the nanostructured ZnO before and after UV illumination. By putting ZnO thin film in dark condition for seven days the superhydrophobicity can be restored. The process has been repeated for several times without any deterioration as depicted in figure 1.2b. This is related to the nano-porous surface photosensitivity of the ZnO structures. The wettability is controlled by the geometrical structure of the surface and also the material surface chemistry. A nanostructured ZnO structure subjects mostly to the non-polar low energy side



surface and is a rather porous structure, which perfectly promotes the hydrophobicity behavior. In particular, nanostructured ZnO generates hole and electron pairs under UV irradiation, and the holes can release the oxygen molecules with negatively charged absorbed on the nanostructured ZnO surface, which are full by hydroxyl group, that therefore enhances the hydrophilicity phenomenon of the nanostructure surface.

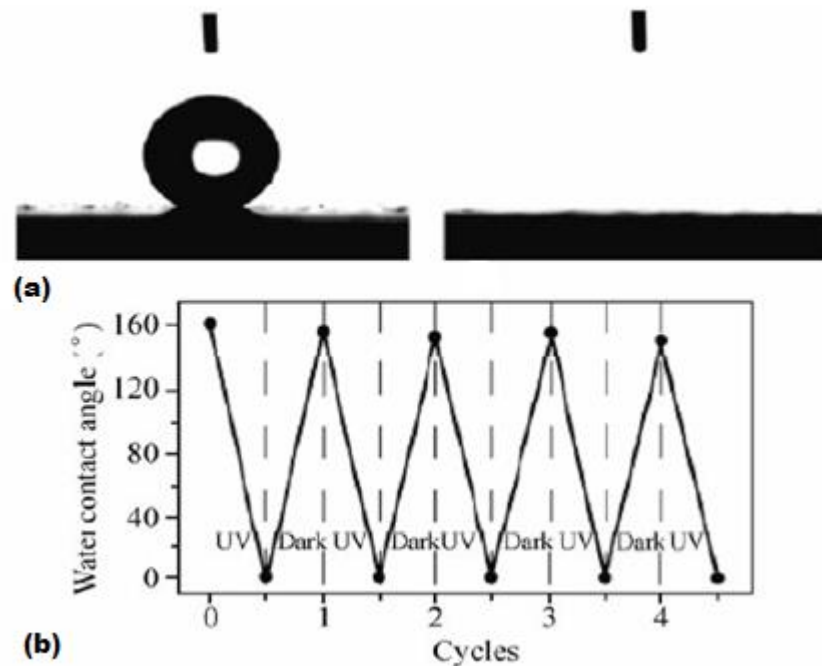


Figure 1.2 (a) a spherical water droplet on nanostructure ZnO thin film after (right) and before (left) UV irradiation. (b) Reversible superhydrophobic superhydrophilic under UV irradiation and dark storage [31].

In the dark condition, the oxygen molecules replaced gradually the hydroxyl compounds on the nanostructured ZnO surface since their absorption is more favorable thermodynamically. Therefore, the hydrophobicity phenomenon can be restored.

#### 1.2.4.4. ZnO field emission characterization

This property has applications in microwave devices, x-ray source, and photoelectric panel display. Due to high partial pressure of the oxygen during ZnO process, it has been become one of the best candidates as a field emission cathode. Having vertically aligned fine tips and relatively high density are desirable for the improved tips by local electric field. The nanotip

ZnO arrays (figure 1.3a) were fabricated via hydrothermal method on a ZnO seeding layer, with a ratio of 1:2 zinc source to HMTA [32]. Field emission investigated at room temperature in vacuum condition. The nanotip ZnO structures were positioned as a counter anode with certain size, and cold cathode, then the counter anode was placed away from the cathode at a known distance. By applying a voltage, an electric field built up between electrodes. To generate a certain current density, the threshold and the turn-on field were defined as the macroscopic required fields.

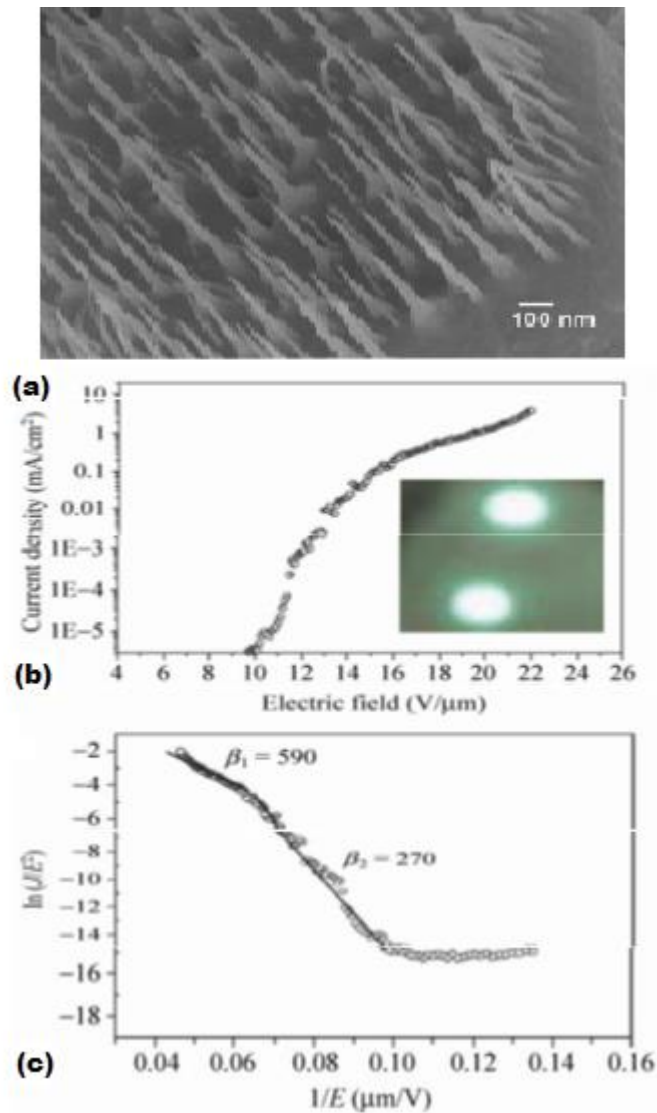


Figure 1.3. (a) synthesized ZnO nanoarrays. (b) Field emission current density versus electric field of ZnO nanotip arrays on Si substrate and (c) the corresponding plot [32].

Figure 1.3 (b) depicts a plot of field emission current density with respect to the applied field. Modification of the ZnO nanotips with metal nanoparticles reduced the turn-on field

effectively. One of the big advantages of nanostructured ZnO based field emission technology is the stability. Fowler-Nordheim (F-N) is governed the field emission behavior:

$$J=(AE_2\beta_2/\Phi)\exp(-B\Phi_{3/2}/\beta E), \quad (1.1)$$

Where  $E$  is the macroscopic applied electric field (V/cm), term  $\beta$  is field enhanced factor, explained by

$$E_{local} = \beta E = \frac{\beta V}{d} \quad (1.2)$$

Where  $E_{local}$  is electric field of the emitter  $\beta$  tips, it is influenced by emitter density, vertical alignment, crystal structure quality, and the emitter geometry. Having high  $\beta$  values is desirable. The density of emitters plays a significant role.  $\Phi$  refers to work function for ZnO it is approximately 5.4 eV.  $B$  and  $A$  are two constants with values of  $6.83 \times 10^3$  ( $V \cdot eV^{-3/2} \cdot \mu m^{-1}$ ) and  $1.56 \times 10^{10}$  ( $A \cdot V^{-2} \cdot eV$ ) respectively. And  $J$  is the current density emission in  $A/cm^2$ . Figure 1.3 (c) depicts plotting of  $\ln(J/E^2)$  with respect to  $1/E$ , the curve demonstrates more than one slope, due to absorbate induced emission saturation or the variation in the tip field.

#### 1.2.4.5. Photonic crystals

The photonic crystal is defined when photons traveling inside the aligned structure, resulting in a contrast refractive index. In particular, when the nanostructured ZnO arrays are aligned vertically gives rise for photons transportation, it is called photonic crystal ZnO. When atom arrays in crystals give the electrical potential to an ordered distribution for inside electrons transportation, the result is an electronic band gap. Therefore, the crystal poses a band gap which is called 'photonic band gap'. The defects can introduce the localized states in the photonic band gap in a photonic crystal, which is allowing the photons to diffusion at the localized states with specified frequencies. The photonic crystals properties control the diffusion and emission of photons in an optical communication system. In filtrating the empty sites between the nanostructured ZnO especially nanowires with a polymer and eliminating the nanowires with bases or acids can make reversed photonic crystals. The acceptable crystalline structure for being a photonic crystal is significant, since defects including grain, and voids can scatter the electromagnetic waves which are leading to loss by diffusion. Figure 1.4 depicts a transmission spectrum for a photonic crystal. High FWHM of the peak demonstrates a non-perfect photonic crystal.

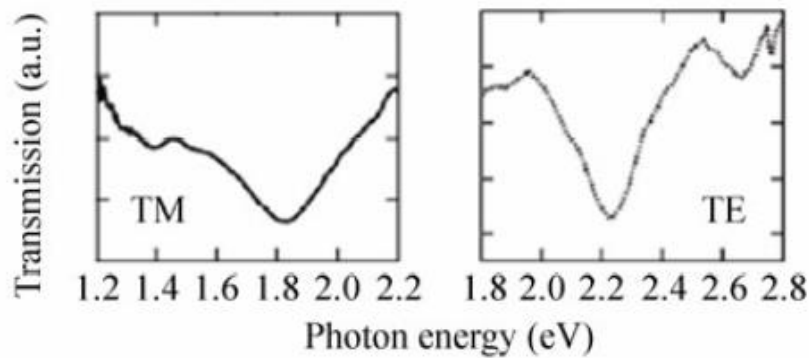


Figure 1.4 The transmission spectrum of the ZnO nanowire arrays for both TE and TM polarizations [33].

#### 1.2.4.6. Photoluminescence (PL) of ZnO

The photoluminescence of nanostructured ZnO, can be excited at room temperature by a UV light, with two emission bands. One in the visible region, comes from deep level recombination of the hole-electron caused by the surface and defects, for instance, the adhesion of the hydroxyl compounds in the crystal fabrication, zinc interstitials, and oxygen vacancies. The another is associated with the UV region peak, which arises due to emission from the band edge within exciton-exciton accident processes. Figure 1.5 (a) depicts a typical photoluminescence spectrum of nanostructured ZnO. There is a weak visible peak at around 500 nm, with dominant UV emission at near 380 nm. The emission in near infrared (IR) region at 760 nm for the nanostructured zinc oxide fabricated on the Au coated indium tin oxide (ITO) surface is associated with the second ordered characterization of UV emission [34]. The first peak blue-shift emission is because of the size of the nanostructured ZnO reduced to below 10 nm. The green emission derived from defect results in a reduction in quantum efficiency and exciton lifetime of the systems. To promote the band-edge UV emission and decrease emission from the defects, annealing in different atmospheres and different temperatures as post-plasma enhancement has been performed. The defect concentration can be reduced by annealing the structure at 200 °C. The defect and near-band-edge emissions can be effectively enhanced by coating a polymer on the nanostructure ZnO. Figure 1.5 (b) depicts a PL spectrum of nanostructured zinc oxide at 4.2 K. When the temperature reduced from 300 K to 4.2 K, the intensity of PL spectrum increased dramatically. The blue-shift from 378 nm to 368 nm is due to the shallow bound exciton. Since the band gap of semiconductors increase as the temperature reduces. Additionally, the

transversal and longitudinal optical (TO and LO) phonon replicas were also clear. As depicted in figure 1.5b, the separation of the energy between the mentioned phonon replicas is matched well phonon energies in nanostructured ZnO crystals.

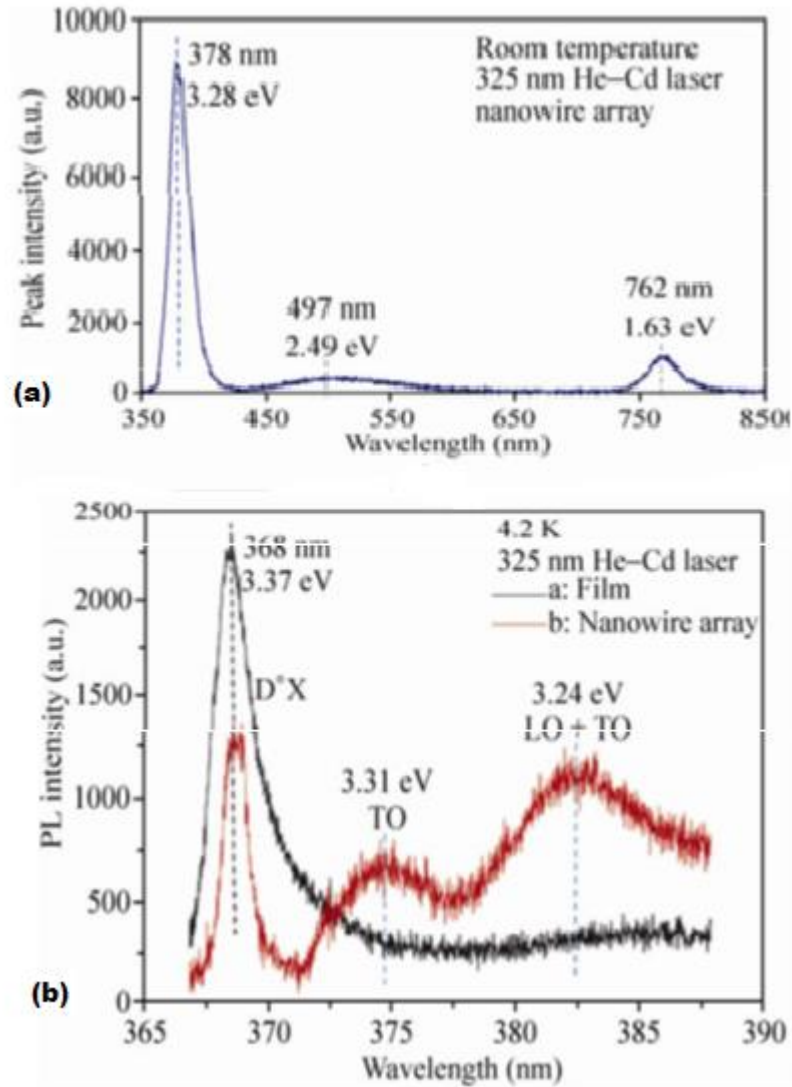


Figure 1.5 (a) PL spectrum of nanostructure ZnO fabricated on the Au-coated surface. (b) PL spectrum of thin film ZnO and nanostructure ZnO at 4.2 K [34].

## 1.2.5. Applications of nanostructured ZnO

### 1.2.5.1. Electrochromic displays

The electrochromic display systems undergo color change on extraction driven or charged injection by applied voltage. They have four strategies including low power consumption and low cost, memory effects under open-circuit states, and high coloration efficiency. In

research, an electrochromic system has been demonstrated based on nanostructure ZnO [35]. The structure of the system has been demonstrated in figure 1.6. The wet chemical approach used to synthesize ZnO arrays on a transparent conductive material. Then methyl viologen molecules which are an organic chromophore were loaded onto the nanostructure. The molecules which were absorbed physically or chemically on the surface of the nanostructured ZnO stayed there with the aim of charge transport between viologen molecule and nanoarrays. The nanostructure provided charge transport path directly because the switching speed of the system was very fast. The viologen molecules reduced under a reverse bias, and become blue within approximately 170 ms, by removing the bias the color held for about 1 hour.

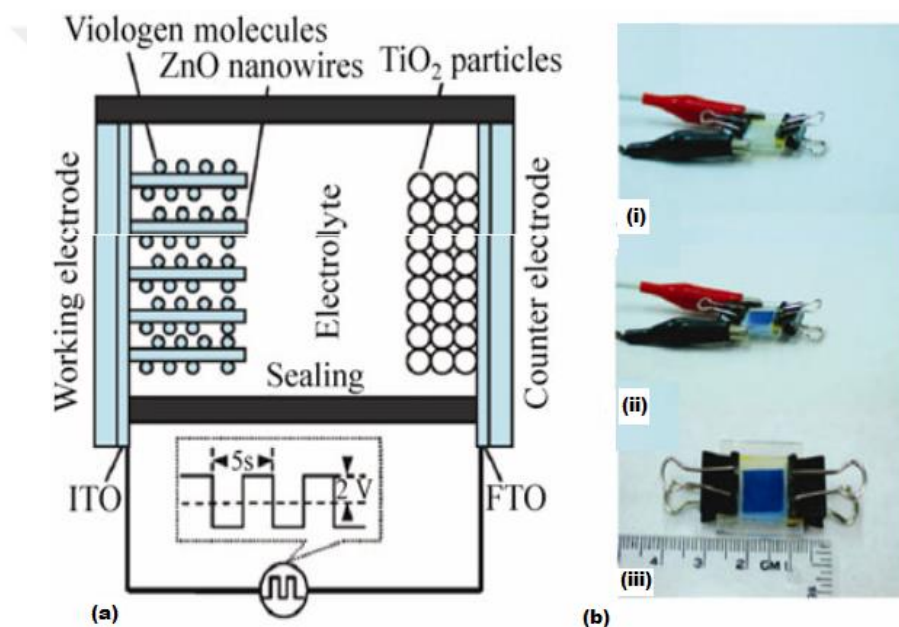


Figure 1.6 (a) The electrochromic system. (b) images of the system (i) before (ii) and after applying bias, (iii) circuit state [35].

### 1.2.5.2. ZnO structure in field-effect transistors

Field-effect transistors (FETs) based on nanostructured zinc oxide thin film has used in transparent and flexible electronics. Fabrication of ZnO in situ between drain and source electrodes is suitable with low-temperature wet chemical methods. Figure 1.7 depicts nanostructure ZnO transistor fabricated on polymer surface via an all- solution method [36]. The drain and source electrodes were manufactured Au nanoparticles followed by annealing. The ZnO nanomaterials have seeded the fabrication of nanostructure ZnO, and applied to the Au electrodes. As depicted in the figure. 1.7b, the nanostructure ZnO fabricated and connected the two electrodes through forming a nanostructure complex network, which is

depending upon the channel size between the drain and source electrodes. The contact between ZnO and Au must be ohmic. The work function mismatch between ZnO and Au are 4.5 eV and 5.1 eV respectively. The interfacial defect state is determined the transport properties. Figure 1.7c depicts the averaged transconductance  $g_m$  (maximum value about 100 nS) and output characteristics, which demonstrated a n-type channel with off/on the  $10^4$ - $10^5$  current ration.

According to:

$$\mu_e = gm2L/2IdC_{ox}W \quad (1.3)$$

the electrons mobility  $\mu_e$  in the nanostructured ZnO was measured to be  $0.2 \text{ cm}^2/\text{V}\cdot\text{s}$ . Where W and L are the channel width and length,  $C_{ox}$  is the gate capacitance. The reduction in mobility of the electron in nanostructured ZnO was induced using the nanostructure process of the surface scattering. The transistor based on the nanostructure ZnO did not demonstrate a full saturated regime as the voltage of the drain was achieved, probably due to the impurity-derived grain boundaries and the dominant phonon scattering in the bridged nanostructure ZnO. The characterizations of the FETs strongly depend upon the nanostructured ZnO alignment.

### 1.2.5.3. Sensors

Based on the multijunctional p-n diode, the barrier height change, piezoresistance or resistance change of the nanostructure, the nanostructured ZnO used as an active component in the strain sensors, biosensors, UV visible-blind sensors, visible light sensors, and gas sensors. The ZnO can be functionalized with hydroxyl ( $\text{OH}^-$ ) or protons ( $\text{H}_3\text{O}^+$ ) groups with  $\zeta$  potential by changing the pH with respect to isoelectric point ZnO, since it is an amphoteric. The PH sensors can be utilized by nanostructure ZnO as an electrochemical probe. Since nanostructured ZnO arrays offer real-time detection, and high sensitivity. In a research, a very sharp nanostructured ZnO was fabricated on electrodes. The principal mechanism represented that any change in pH of the environment leads to change in potential of the nanostructure surface, then can be detected with any change in voltage between electrodes. Figure 1.8 depicts the potential between the reference and working electrodes which was proportional to buffer pH, with a perfect sensitivity of  $52 \text{ mV/pH}$ . The

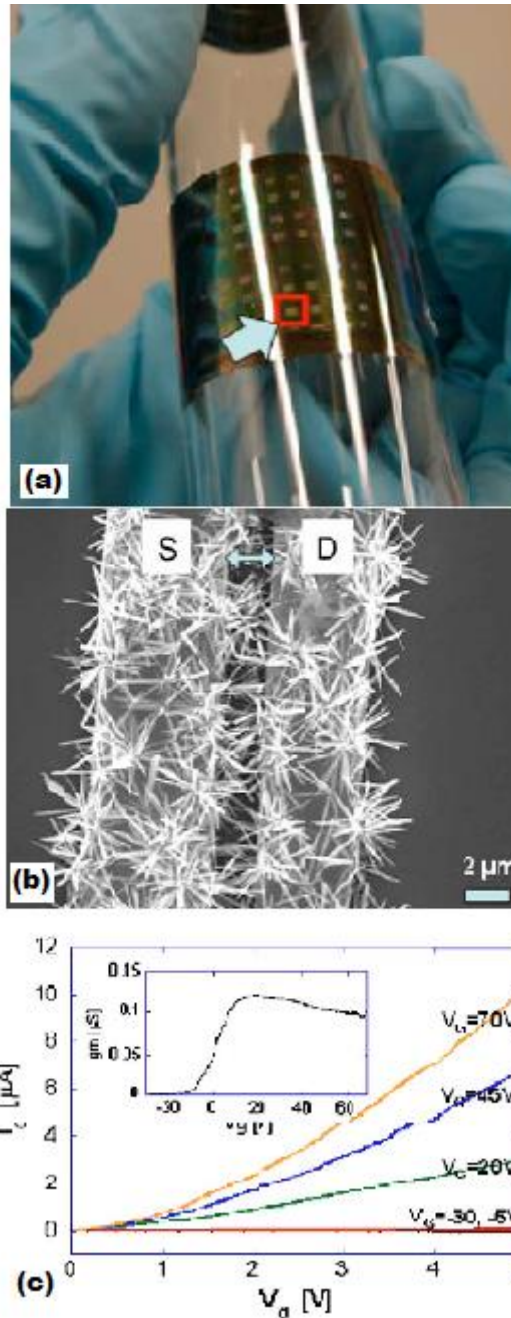
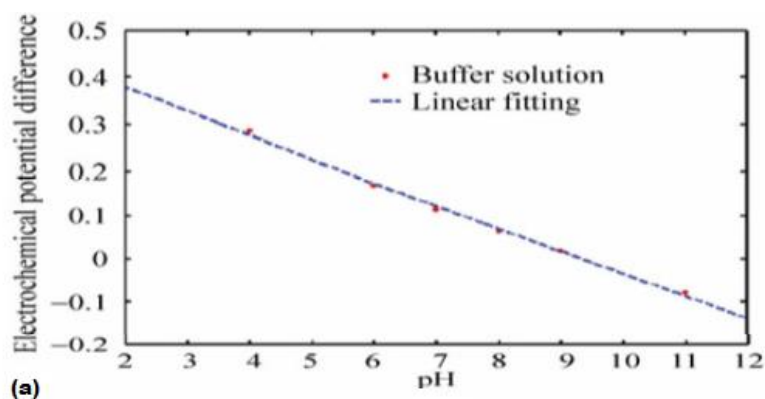


Figure 1.7 (a) nanostructured ZnO transistor structure on a flexible substrate. (b) the nanostructure ZnO under SEM fabricated between the drain and source electrodes. (c) The output properties of nanostructure ZnO transistor with 10 μm channel. The inset depicts the transconductance with respect to the gate voltage [36].

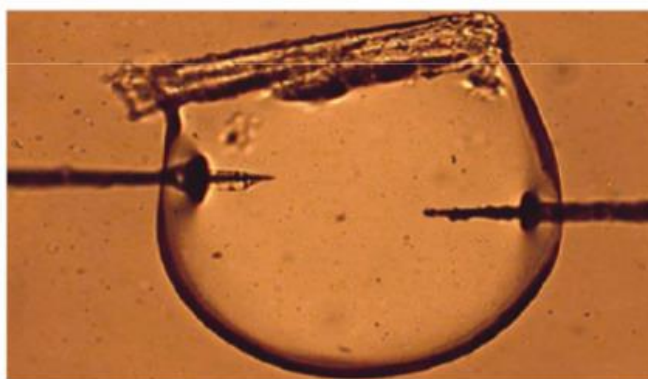
nanostructured ZnO was thermodynamically stable at room temperature over the tested pH range. Therefore, to measure the intracellular pH value, the working and reference electrodes were pushed to enter to a human fat cell membrane. As demonstrated in figure 1.8b, the electrodes were in touch with cytoplasm of the cell, and analyzed the pH of the intracellular to be 6.8 [37]. To measure the pH in single living cell, this method is one of the



perfect ways. Since ZnO is biocompatible, nontoxic, and the intracellular measurement cannot affect the cellular viability.



(a)



(b)

Figure 1.8 (a) calibration plot for working and reference electrodes in a standard buffer. (b) The pH of the intracellular measurement inside a human fat cell [37].

#### 1.2.5.4. Solar cells applications of ZnO

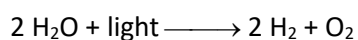
Traditional silicon solar cells have high carrier mobilities and low defect densities, and due to well-developed industrial fabrication technologies and the relatively high energy conversion efficiency, they are dominated by the solar energy industry. Different organic and inorganic compounds have been studied with the purpose of increasing efficiency by further decreasing cost of the energy per unit performance. The nanostructured ZnO is one of the best candidates for solar cell applications. Since it has fast electron transport and can be used as an electron transport layer (ETL) along the crystalline structures, high charge collection efficiency, very high area to volume ratio that can enhance the interfacial charge separation, and a very low reflectivity that can improve the absorption of light. The nanostructured ZnO have been carried out for excitonic and traditional p-n junction photovoltaics including

organic dye and inorganic nanoparticle sensitized organic and hybrid organic-inorganic solar cells.

#### 1.2.5.5. Hydrogen generation via water splitting

Hydrogen gas is one of the important energy sources with a very high energy density quantity. Hydrogen reacts with oxygen to generate water and electricity without producing any by-products as pollutants. The nanostructured ZnO as a metal oxide semiconductor has potential as high-performance photocathodes or photoanode for splitting of the water molecules into a photoelectrochemical systems (PEC). Since, it has high electron mobility efficiency, low series resistance, flat band potential and suitable direct bandgap, and high surface to volume ratio. To promote absorption efficiency in the visible region, nanostructure ZnO can be combined with different semiconductors including CdSe, CdTe and CdS quantum dots, and ZnO-CdS core shell structures. Among the cadmium chalcogenides, the CdTe is more effective than others due to favorable band energy which can be injected the electrons into ZnO structure more than others. The quantum dots (QDs) can perfectly increase the efficiency by following multiple excitons from several layers of absorbed photon. The Mott-Schottky analysis demonstrated a very suitable depletion thickness, flat band potential, and electron density. In the illumination condition, hole and electron pairs fabricate in the nanostructured ZnO then they separate in the depletion area at the nanostructured surface. Finally, the separated holes are injecting to the electrolyte and nanostructure interface to give rise to O<sub>2</sub> by oxidizing and OH<sup>-</sup> the groups, while electrons are reducing the H<sup>+</sup> groups and producing H<sub>2</sub>, by flowing to the cathode.

Water molecule Splitting reaction is:



Under +0.5 V external potential, the nitrogen doped nanostructure ZnO demonstrated a photon-to-hydrogen conversion of 0.15%. To promote the efficiency, nanostructure ZnO/multi-walled carbon nanotubes heterostructure were utilized to enhance the PEC device whole active surface area. The non-ideal and effective factors for the PEC system are including the dissolution and decomposition of the anode structure, that can be oxidized if the potential is more than the anode redox potential. The most second factor is the electrode surface energy of the states that can be non-homogeneous from the interior of the electrode. If the surface state levels are suitable, they can be used as electron transfer efficient channels. A piezoelectric potential can be carried out to drive different reactions for

water splitting [38]. Figure 1.9 depicts the working principles. The piezoelectric materials or nanostructures ZnO generate surface charge and undergo physical deformation on the compressive and tensile side under mechanical agitation by ultrasonic wave. Water molecules can be split into O<sub>2</sub> and H<sub>2</sub> in the molar ratio 1:2 when the applied piezopotential is higher than the water standard redox potential (1.23 eV). This shows that the nanostructured piezoelectric materials can get wasted mechanical energy from the environment including vibrations noise, to fabricate hydrogen gas for green energy applications.

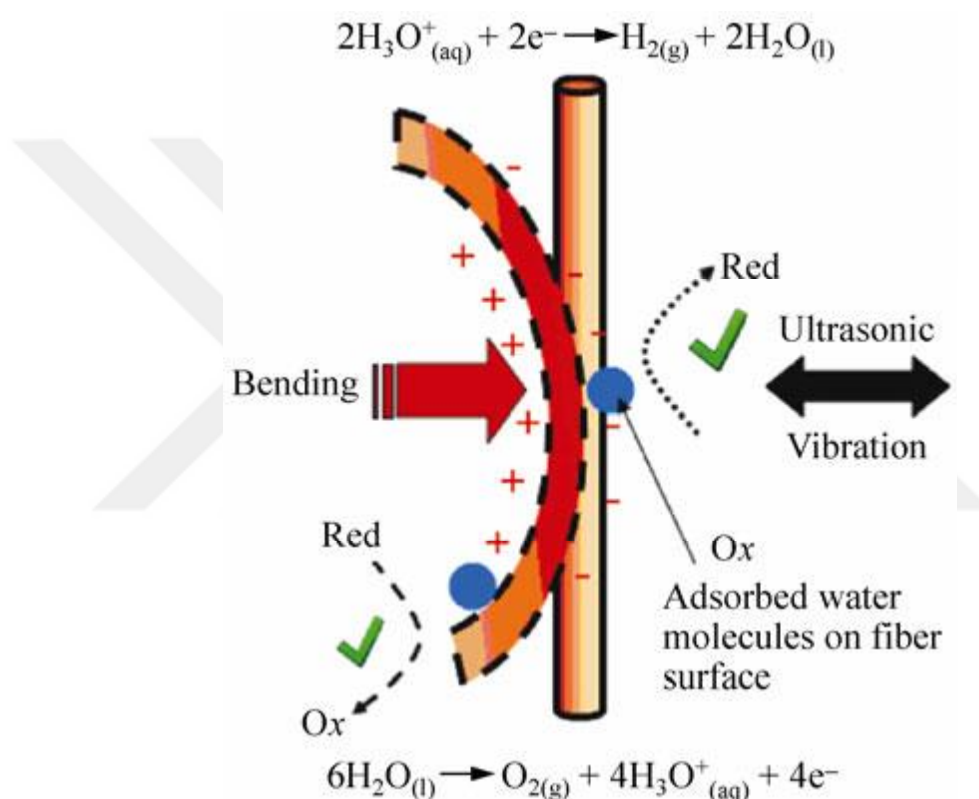


Figure 1.9 The diagram shows the charge and the ultrasonic vibration of the piezo potential created on a nanostructure ZnO [38].

### 1.3. Cadmium Chalcogenide Nanostructures

The nanostructured cadmium chalcogenides are carried out because of their significant optoelectronic and size-dependent physical and chemical properties. Recently, they have received attention. For example, nanostructured cadmium telluride (CdTe), cadmium selenide (CdSe), and cadmium sulfide (CdS) have been attained as an effective semiconductor for modern industrial applications. These nanoscale materials can be

fabricated with a variety of approaches for adjusting their properties with the aim of using in different applications including biosensor, biological fluorescence labels, light emitting diodes (LEDs), FETs, Photovoltaics (PVs), and so on. To enhance their properties, size and morphology harness of the nanostructures are main factors. Therefore, to control the size and morphology of the quantum dots (QDs), a variety of new synthesis method have been carried out.

### **1.3.1. Cadmium sulphide (CdS)**

The CdS semiconductor (direct band gap of 2.42 eV) is a substance with significant chemical and physical properties, which made it a unique photocatalyst in different photochemical processes. CdS also has potential applications including infrared and laser detectors, gas sensors, nonlinear optical materials, optoelectronic and luminescence systems. It is also demonstrated excellent visible light detecting properties. To synthesis of CdS there are varieties of methods.

### **1.3.2. Cadmium selenide (CdSe)**

The CdSe is a semiconductor with controllable size-dependent physical and chemical properties. They can be used in fabrication of LEDs, solar cells, luminescent biological labels, and so on. Interestingly, to harness the properties, the size of the nanostructures become important with respect to Exciton Bohr radius of bulk structure. By controlling the size of CdSe, the quantum confinement of photo-generated hole and electron pairs allow the tuning of optical properties of the nanostructures. In CdSe, the lowest unoccupied or conduction band has 5s orbitals of cadmium, whereas, the highest occupied or valence band has 4P orbitals of selenium.

### **1.3.3. Synthesis of chalcogenide nanostructures**

There are several synthesis methods for nanostructure chalcogenides semiconductors including spray pyrolysis, synthesis from elemental powders, ionic liquid assisted synthesis, solid state reaction, hydrothermal/solvothermal process, pulse plasma assisted route, sonochemical, synthesis into micellar medium,  $\gamma$ -irradiation route, microwave assisted route, single source molecular precursor route, template/self-assembled - assisted synthesis, colloidal precursors, chemical bath deposition, and so on. Stabilized and uniformly dispersed

nanostructures are successfully implemented by using surfactants and capping agents. Functionalized nanostructures with biomolecules and polymers have been fabricated for biological functionalities and optoelectronic. By investigating the effect of process parameters including the use of cosurfactants, the role of surfactants and solvents, temperature, molar ratios, and concentration of ion source precursor, the reaction conditions have been enhanced in different fabrication methods. The formation mechanism of nanostructures has been clarified for several approaches. Different researches focused on the physical and chemical properties related to specific applications including photocatalysts, luminescence for lasing and optoelectronics, so on. Cadmium chalcogenide nanostructures have a potential application such as gas sensing, pollutant reducers, photocatalysts, LEDs, solar cells, and so on. Advances in the fabrication methods have been attained in synthesis nanomaterials or/and nanostructures with varying morphologies. To get the desired shape and size, the basic idea has been processed with a harnessed reaction to start arrested and nucleation growth. However, each route has its limitations and advantages. Therefore, the synthesis of controlled and functionalized nanostructures still poses a great challenge.

#### **1.3.3.1. Colloidal synthesis method**

One common method for the fabrication of nanostructure semiconductors is harnessing the precipitation by a suspension of colloidal nanoparticles. The method idea arises from the slowly injection of the metal ions solution into the non-polar or polar solution of chalcogenide ion source precursor. By adjusting the size of nanostructure after the nucleation step, the fabrication is stopped immediately by harnessing the equilibrium between the solvated ions and the nanocrystals of desired chalcogenides. Most investigations have been carried out for controlling and identifying the effective factors that influence such equilibrium. The factors are including the concentration and molar ratio of the precursors, the role of the solvents, and the temperature which have been found very significant. To achieve very stable and monodispersed nanostructure quantum dots, surfactants, polymers, and other molecules can be used as coated agents. For example, it has been reported that the chalcogenide capped with thiol are very stable. Figure 1.10 depicts the schematic diagram for the fabrication of CdTe nanostructure quantum dots functionalized with thiol ligand [39]. Thioacetamide, thiourea,  $H_2S$ , and  $Na_2S$  can be used as the sulfur source. The drawbacks of the methods are including invariably related surface defects and large size distribution, and poor crystallinity of nanostructures.

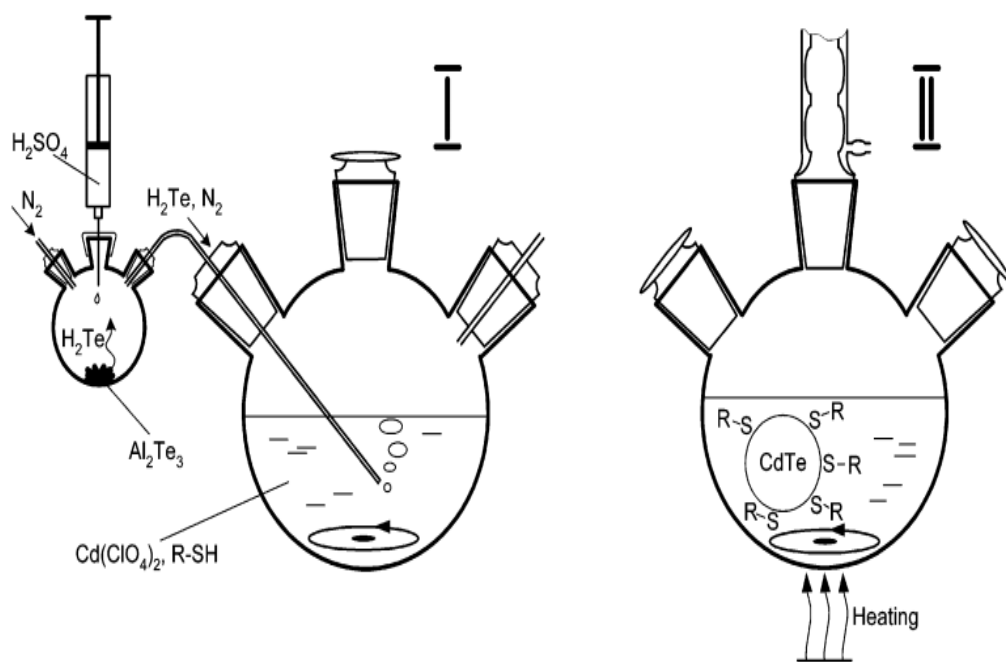


Figure 1.10. Schematic depicts the fabrication of thiol capped CdTe quantum dots. Left depicts the formation of CdTe precursor by  $H_2Te$  gas. Right depicts growth of CdTe QDs by reflux [39].

### 1.3.3.2. High temperature injection

For the fabrication of cadmium chalcogenide nanostructures, single molecule decomposition of the precursors prepares effective and convenient routes. In this synthesis route, molecular complex including the chalcogen and cadmium metal are thermally decomposed in a non-polar coordinating solvent. The fabrication of core-shell-shell CdS/CdSe/CdTe nanostructure QDs reported using the precursor of materials dispersed in an organometallic reagent such as tri-octylphosphine (TOP) is followed by the organometallic pyrolysis on injection into a coordinating solvent, tri-northophosphine oxide (TOPO) [40] at a very high temperature as depicted in the diagram figure 1.11. The formation of the nanostructures QDs initiated by the precursors decomposition whereas the fabrication of nanostructures is prevented when the precursor supply is unloaded. The size control synthesis of nanostructure QDs carries out in three steps: 1) The injection of precursors, 2) the nucleation, 3) the Ostwald ripening growth control of the nuclei. The resulted QDs can be agglomerated as TOPO passivated. The QDs nanocrystals provided by this approach have more crystalline quality than those fabricated by colloidal methods.

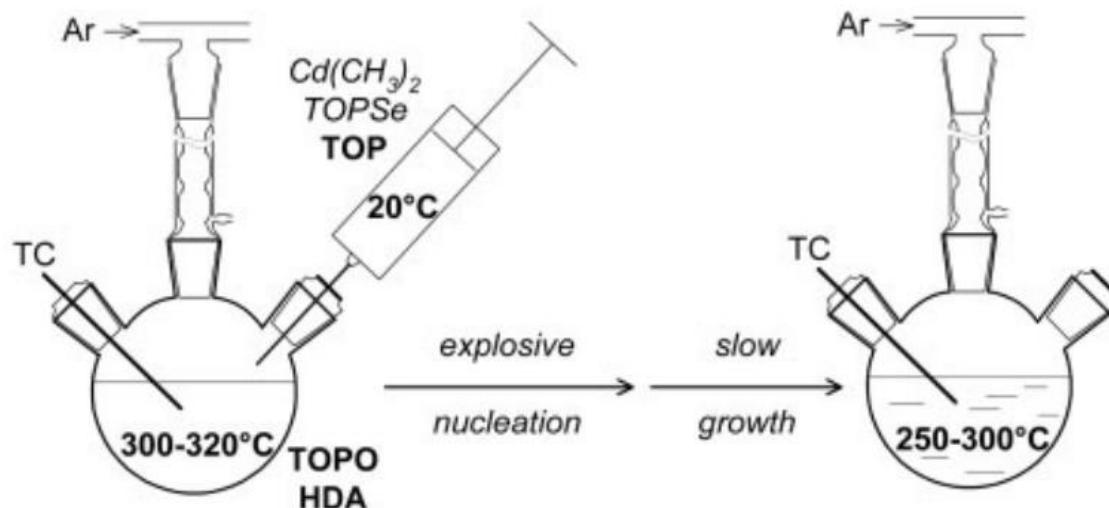


Figure 1.11. Representation of hot injection approach in organo-metallic fabrication of QDs nanostructures [40].

To provide a single-source precursor from available chemicals, many scientists used simple cadmium salts instead of selenocarbamates and dithiocarbamates of metal compounds of dithiobiurea as a single-source precursor for the synthesis of high-quality and mono dispersed QDs with adjustable color tuning. The limitations prohibited using such approaches including the toxic materials such as CE<sub>2</sub> (E=Se or S) for the fabrication of the materials precursor. Cadmium thiolate, metal chalcogenolates and selenolate derivatives were used as precursors for fabrication of nanostructured cadmium selenide and sulfide. Monodispersed cadmium chalcogenide nanostructures (CdE; E=Te, Se, S) can be fabricated by organometallic materials including formaldehyde. Cadmium chalcogenide nanostructures were also synthesized by using tributylphosphine (TBP) at high temperatures. In an environment-friendly approach cadmium oxide, carbonate, and acetate were used as a greener cadmium source instead of dimethyl cadmium. The nanostructured Zn, Cu, Pb, Mn, Hg, and Cd sulfide can be fabricated by thermal decomposition. However, because of the fact that, using pyrophoric and highly toxic materials as metal sources, and alkyl amines, TOPO as a solvent which have high boiling point, requires special inert gas and high temperature environment that makes the approach complex for scaling up and more expensive.

### 1.3.3.3. Hydrothermal/Solvothermal process

The hydrothermal process carried out under temperature and pressure reaction between the different precursors; the approach is called the hydrothermal process. This approach utilizes high boiling point solvent through autogenously high temperature and high pressure in an autoclave. Therefore, it is very suitable for fabricating highly crystalline nanostructures

by using cheap low boiling solvents. The water can be used as an environmental solvent. Recently, wide variety numbers of precursors have been used to fabricate metal chalcogenide nanostructures via hydrothermal method. The effective factors for morphology and the size of nanostructures are 1) temperature, 2) the time of hydrothermal decomposition, 3) the type of surfactants used, and iv) the nature of the solvent used. The hydrothermal method has benefits including purity of nanophase, the nanostructures size distribution, but morphology difference still remains and needs to overcome.

#### **1.3.3.4. Microwave-Assisted synthesis**

In this approach, microwave radiation induces a chemical reaction to produce desired products. The electromagnetic field with high-frequency radiations force on the charged particle solution and generating molecular rotation or charge migration. This process may generate further polarization in polar molecules. Micron size structures with different morphologies can be fabricated by using visible light and simple aqueous method under microwave and employing different Sulphur ion source. The nanostructured CdS can also fabricate using thiourea and cadmium acetate in certain solvent via microwave irradiation. The molar ratio of precursors has been found also critical. This method has advantages including purity of materials, small particle size, short reaction time.

#### **1.3.3.5. Sonochemical process**

In this method, the energy is transferred to the solution by an ultrasonic radiation. The ultrasonic radiation interacts with the molecules and solution and the energy improves the reaction activating. The synthesis with the sonication method is a significant approach for the fabrication of nanostructures. The ultralysis is based on cavitational heating by collapsing bubbles and surface damage and emulsification. The ultrasonic wave forms bubbles in solution that collapse each other; this process is defined as cavitation process. During bubble formation, heat transfer to the solution and an extreme situation is generated, this phenomenon induces the chemical reaction. The nanostructured CdSe, CdS, and other chalcogenides can be synthesized using the sonochemical method. The nanostructures with different morphologies including nanowires or nanotubes, nanorods can be fabricated using sonochemistry by using direct growth helping agents. Sonochemically synthesis has potential advantages including small particle size, better thermal stability, and uniform size distribution.



#### **1.3.3.6. Capping-Assisted synthesis**

To develop diversified QDs semiconductors, capping synthesis is very promising since the morphology of the crystals is strongly dependent upon the type of capping ligand attracted on their surface. The surfactants play a significant role in the fabrication of nanostructures especially in controlling morphology, shape, and size of the fabricated nanostructures as well as stabilization to specific assemblies. These assembly methods are including bilayer liquid membranes, Langmuir Blodgett film, micro-emulsion, monolayers, micelle, reverse micelle, and so on. Nanostructured cadmium, zinc, and lead chalcogenides have been fabricated using surfactant assemblies. Thiol coated nanostructures QDs are water-soluble since thiol capping agents are hydrophilic molecules that are strongly coordinated to the QDs and a polar group such as amine, carboxyl, and hydroxide ensuring hydrophobicity. They can be also coated with a polymer and biologically active macromolecules. The macromolecules including polymer, RNA, DNA, proteins, and amino acids can control the growth and nucleation of QDs. Some advantages have been brought by biological macromolecules conjugation including biocompatibility and bioactivity, and biological functionality which can provide on the surface of QDs. This has brought many applications including bio-labeling, drug delivery by luminescence probing, and so on.

#### **1.3.4. Applications of metal chalcogenide nanostructures**

Quantum dots or chalcogenide nanoparticles have potential applications in medical technology to material science. They demonstrated continuous absorption spectra, long term photostability, tunable quantum efficiency, and narrow emission, therefore they are invariable materials for different photovoltaic and biomedical applications. Their applications include Optoelectronic materials for LEDs, photo-catalyst, degradation of pollutants, photo-reduction of dyes and pigments, photochemical applications, photocatalysis, solar cells (both QDs organic-inorganic and sensitized hybrid), and so on. Among the biomedical applications, cancer therapy, drug delivery, DNA labeling and observation of diagnosis have attracted more attention. Recently, the QDs have been used in long term in vivo and in vitro cell trafficking, and high-resolution cellular imaging, tumor targeting, drug delivery and diagnostics [41]. Figure 1.12 depicts the classification of potential biomedical applications of QDs in bio-imaging and bio-sensing.

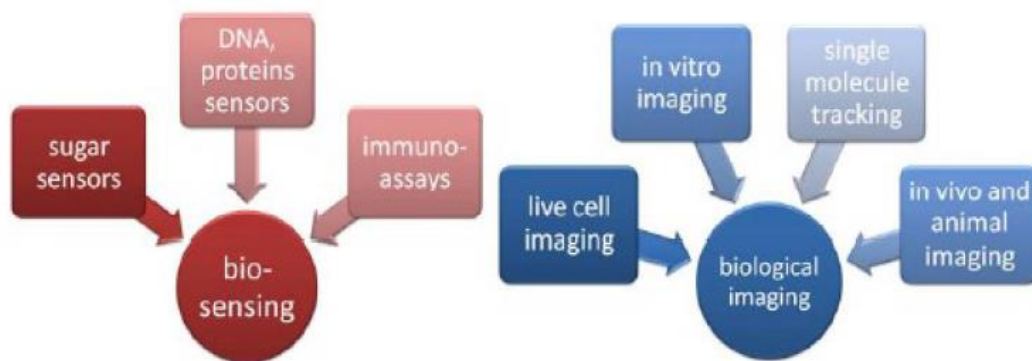


Figure 1.12. The classification of biomedical applications of QDs [41].

The possibility of utilizing QDs semiconductors as fluorescence labeling reagents for biological imaging experiments has been depicted by a core-shell structure such as CdSe/ZnS and CdSe/CdS attached to proteins and DNA molecules. Because of the unique emission properties of QDs, a lot of color probes can be distinguished in a single exposure and excited by a single narrowband excitation source. This can make QDs superior to use organic chromophores. The QDs have been demonstrated as the best systems for intracellular investigations including tracking single molecules in the cell, investigation of the dynamic cellular processes, and visualizing the cellular structure. However, metal chalcogenide bare QDs possess toxicity and have a hydrophobic surface, therefore, they cannot be used in vivo without surface modification and functionalization. By suitable surface modification, it has been possible to reduce toxicity and increase hydrophilicity.

#### 1.4. Halide Perovskites

The nanostructured perovskites have been attracted high attention in optoelectronic industries due to their unique electronic and optical properties such as cost-effective and easy solution processability, bandgap tunability over the visible region, sharp absorption edge with small Urbach tails, and long charge carrier propagation. Their electronic and optical properties can be varied in different visible ranges by the composition differences of metal ion ( $\text{Ge}^{2+}$ ,  $\text{Pb}^{2+}$ ,  $\text{Sn}^{2+}$ ), cation formamidinium or methylammonium as well as an anion ( $\text{Br}^-$ ,  $\text{I}^-$ ,  $\text{Cl}^-$ ), which form a 3D structure of the  $\text{AMX}_3$  type as demonstrated in figure 1.13 a. Additionally, the shape, size, morphology and dimension of nanostructured perovskites can be adjusted with a variation ratio between perovskite precursor and the amine chain ligands (figure 1.13). Due to strong anisotropy and quantum confinement, they show size- shape-dependent electronic and optical properties distinct from their bulk structure peers. QDs based on Perovskite suppose a dimension in size smaller than the exciton Bohr radius. In

general, nanostructure perovskites depict higher photoluminescence quantum yield, especially in suspension, that can be related to the lower defect concentration and the charge confinement.

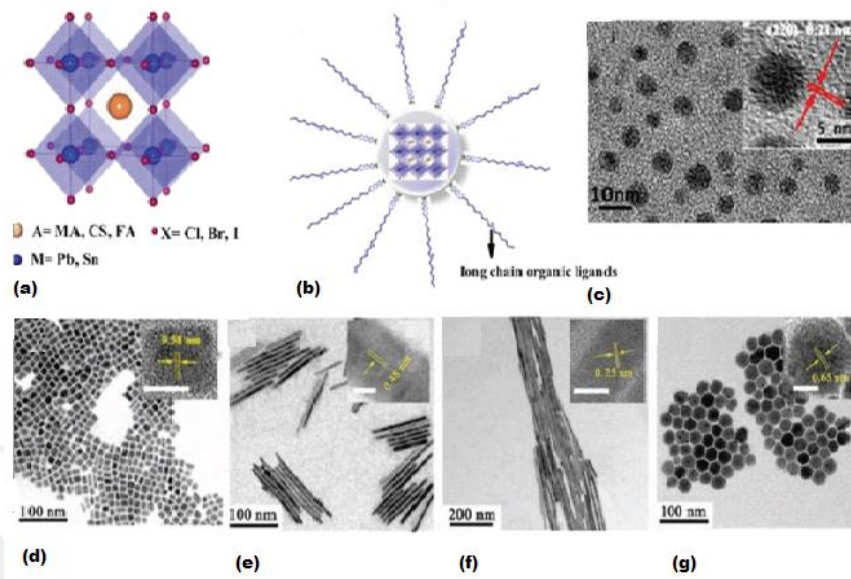


Figure 1.13 (a) perovskite unit cell and ions. (b) schematic of a perovskite quantum dot and oleate ligands on the surface. (c) typical high-resolution (HRTEM) image of MaPbBr<sub>3</sub> QDs perovskite. (d-g) TEM images of the CsPbX<sub>3</sub> perovskite QDs with different structures, (d) nanocubes, (e) nanorods, (f) nanowires, (g) hexagonal nanoplates [42].

On the other hand, their transport properties positioned below of 3D and bulk structures. Figure 1.14 summarized the properties of QD perovskites as with respect to their bulk structures. When the nanoparticles such as nanowells, are functionalized by an organic ligand, therefore the separation of the hole-electron pairs interaction becomes inactive. The nanowell exciton of perovskites can be increased by a magnitude with respect to the bulk phase. The higher binding energy importantly decreases the exciton separation probability prior to radiative decay, therefore it represents excellent PLQY. For instance, the calculated exciton binding energies for nanoparticles and MAPbBr<sub>3</sub> are 320 and 84 meV, respectively as represented in figure 1.14 b-i,ii. As depicted in figure 1.14 c, the perovskite nanoparticles have specific electronic band structure, where defect states do not act as trap states and appear inside the bands. Therefore, perovskite nanoparticles have higher photoluminescence properties over the traditional semiconductor nanoparticles, which for achieving high photoluminescence needs an electronic passivation layer of wide bandgap semiconductors. The nanoparticles represent color tuning properties as function of the size

the same as inorganic chalcogenide nanoparticles, while perovskite QDs represent very high color purity and the size-independent emission wavelength, because of crystal-dependent electronic band as represented in figure 1.14 D. The unit cell of the perovskite is sensitive to the size of cation “A” position, and increasing the cation size can cause reconstruction for the perovskite framework. For example, larger cation “A” can produce the 2D perovskite of  $A_2MX_4$  types, by comparing the monomolecular layer of  $[MX_6]$  octahedral by “A” cation block layers,  $A_4MX_6$  type 0D structure or 1D  $A_3MX_5$  type chain-like structure.

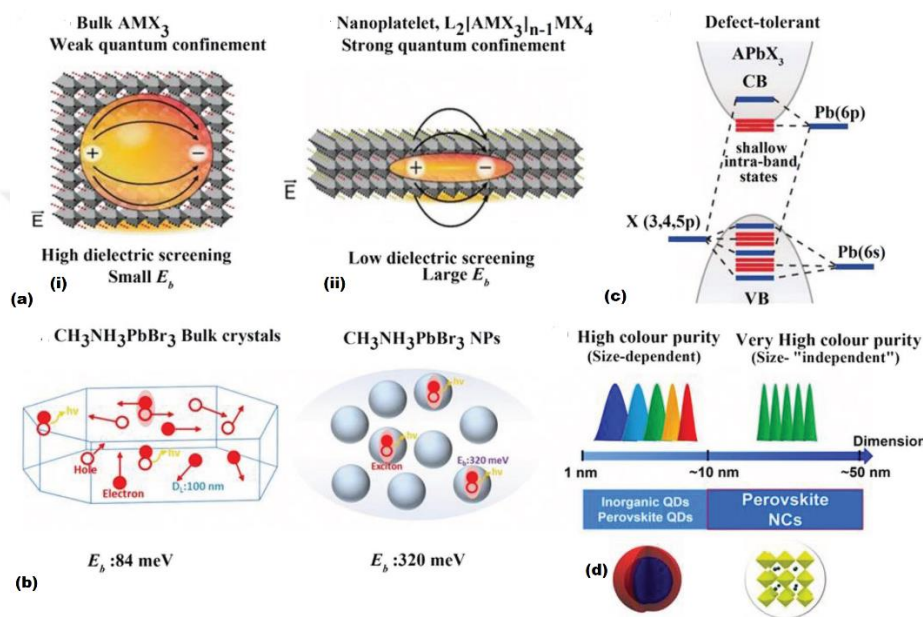


Figure 1.14. (a) Representation of dielectric effects on electronic states in (i) cubic bulk perovskite and (ii) nanoplatelets. (b) Comparison between binding energy for nanoparticles (320 meV) and  $MAPbBr_3$  bulk crystals (84 meV). (c) Lead halide perovskite defect tolerance. (d) Dimension distributions of inorganic chalcogenide QDs, perovskite QDs, and perovskite nanocrystals [42].

While quasi-free charge carriers have been distinguished in 3D perovskite, excitons are confined in the 2D inorganic structures because of higher binding energy. The nanowell perovskites can form a  $A_2(AMX_3)_{n-1}MX_4$  structure, which is known as Ruddesden-Popper perovskites. These 2D structures are a mixture of the  $A_2MX_4$  (2D)- and  $AMX_3$ -types where the organic layers adopt the role of the barrier, whereas the inorganic layers act as quantum well. Inorganic wells can be effectively confined and form the photo-induced charge carriers excitons, and by decreasing well width the confinement effect increases, for example, the number of inorganic layers. Therefore, by reducing the inorganic layer numbers, the excitonic characterization of the 2D structures can be fitted to 3D. This 2D perovskite

introduces additional degrees of freedom which can be used as a perfect way to develop radiative recombination efficiency. This can be brought a problem to inject (or extract) charge perpendicularly to plane layers, and it can be solved by strategies including nanostructure platelets.

#### 1.4.1. Properties of perovskites

To control the electrical and optical properties, perovskite nanoparticles offer an additional degree of freedom over bulk films. Generally, halide perovskites show perfect band gap color emission over the region of 1050-390 nm wavelength with a very high PLQY, color purity and narrow FWHM. By controlling the chemical composition of halide materials (X) in  $AMX_3$  type perovskites, it is possible to adjust the band gap of the perovskites over the visible region. These modifications also have strong effects upon the effective exciton mass and the electronic energies. The  $\pi$  antibonding orbitals (I 5p, Pb 6p) are the main participation for conduction band minimum and  $\sigma$  orbitals of halide ion (I 5P) and "B" cation (Pb 6s) are for valence band maximum. On the other hand, due to improved effect of hydrogen bonding between the inorganic octahedral and cation network, any change in the "A" cation (with FA to MA) also changes the band gap. In addition to 3D perovskites, a very tunable light emission has been depicted for 2D layered nanoparticles by controlling the shape and size as represented in figure 1.15. These systems do not only represent the potential to overcome the problems related to phase segregation but also offer perfect stability and PLQY. The quantum confinement affects the wave function when at least one of the dimensions reach the material exciton Bohr radius. The energy of quantum confinement in semiconductor nanoparticles calculated using effective mass approximation:

$$\Delta E = \hbar^2 \pi^2 / 2m^* r^2, \quad (1.4)$$

where  $r$  is the particle radius and  $m^*$  is the reduced mass of excitons. According to the equation, a blueshift in the resultant emission (a rise in confinement energy ( $\Delta E$ )) could be received upon the decrease in exciton mass of the nanoparticles ( $m^*$ ) and size ( $r$ ). For example, the combination of quantum size effects as well as halide compositional synthesis have been depicted to fabricate the  $CsPbX_3$  nanoparticles to reach an emission over the whole visible spectral of 700-410 nm, the standard color National Television System Committee has been covered up to 140% with wide color gamut as depicted in figure 1.15.

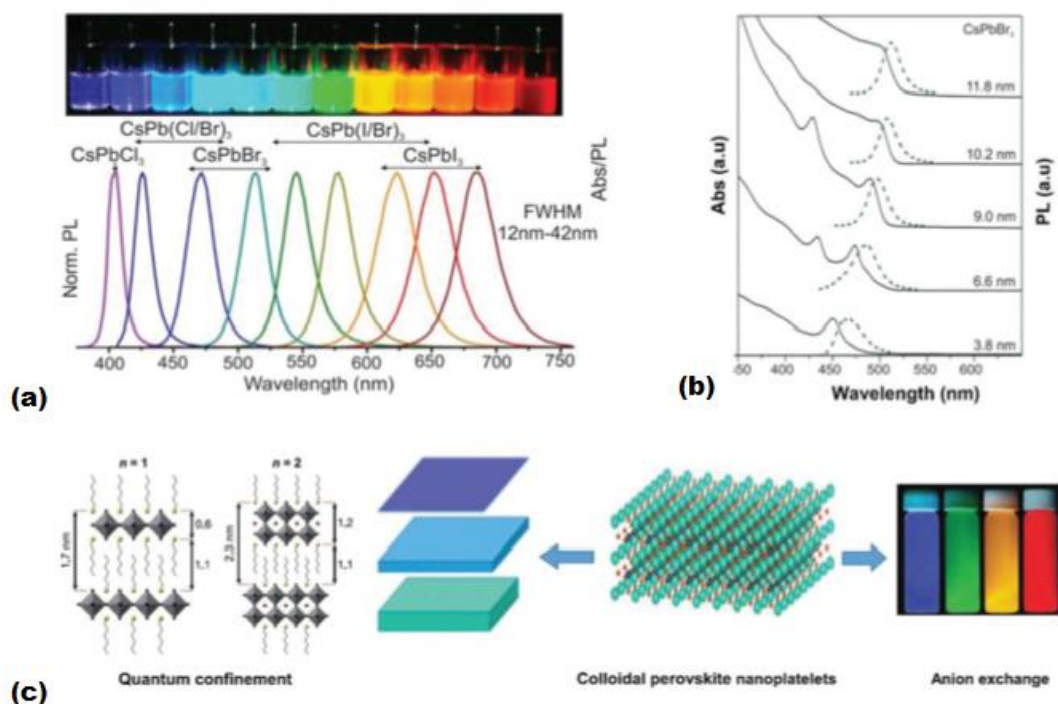


Figure 1.15 Illustration of the color tuning of the perovskite nanoplates and nanocrystals by chemical tuning as well as quantum confinement effect. (a) Colloidal  $\text{CsPbX}_3$  ( $X=\text{I, Br, Cl}$ ) perovskite show composition- and size-tunable bandgap energies covering just visible region spectral with bright and narrow emission. (b) Quantum size effects in the emission and absorption spectra of  $\text{CsPbBr}_3$ . (c) Schematic illustration of the nanoplates stacks [42].

Additionally, a considerably PLQY of 90% and the narrow emission (11-40) have been represented by  $\text{CsPbX}_3$  nanoparticles. With size decrease from 11.7 to 3.9 nm it has been depicted a blueshift from 510 to 455 nm in the  $\text{CsPbBr}_3$  nanoparticles as depicted in figure 1.15b. The harness of the particle size has been successfully utilized to fit the emission of  $\text{MAPbBr}_3$  nanoparticles from 650 to 780 nm by controlling the size from 3 to 8 nm. To modify the bandgap of 3D perovskite the same method can be applied to their lower-dimensional structures. Doping of  $\text{CsPbBr}_3$  nanoparticles with  $\text{Mn}^{2+}$  causes to a blueshift, because of the size variation of the cation, it affected by lattice contraction. The blue emission 456 nm can be achieved by doping with about 0.25% Al in  $\text{CsPbBr}_3$  nanoparticles. Doping with Al supposes a new band gap energy level, which hybridizes as depicted in the theoretical calculation. 2D perovskite with chemical formula  $\text{L}_2[\text{APbX}_3]_{n-1}\text{PbX}_4$  have been good structure to attain the color fitting with stacking of them in a tiny thicknesses. For instance, 2D QWs  $\text{L}_2[\text{FAPbX}_3]_{n-1}\text{PbX}_4$  for  $n = 1$  with substitution of  $X=\text{Br, X=I}$  have depicted violet and green

emissions, however. Interestingly, for  $n=2$ , QWs depict the yellow and blue emissions for iodine and bromide substitutions, which is related to confinement effect as depicted in figure 1.15c. Similarly, by changing Pb with Sn, there would be a redshift. Therefore, by the selection of halide (X) and metal (B), it can be tuned the emission and absorption of the  $n=1$  and  $n=2$  QWs to cover total visible region of the spectrum. The PL emission of the  $\text{MAPbBr}_3$  QWs can be changed by managing the layer width of the wells. The 2D  $\text{MAPbBr}_3$  QWs depict the blueshift and can be further developed with carrier density increasing, attributed to dielectric and quantum confinements. For vacuum deposition layers, further insignificant devices hysteresis has been depicted for  $n-i-p$  and  $p-i-n$  perovskite solar cells, with a grain size average  $<50\text{nm}$ .

#### **1.4.2. Perovskite nanostructure synthesis**

The highly luminescent perovskite nanoparticles have been developed with the aim of improving perovskite light emission systems. They depict potential applications in various fields of optoelectronics including lasing, transistors, photodetectors, light-emitting diodes and so on. The perovskite nanoparticles have been illustrated by a large number of factors including chemical composition, dimensionality, and size of the particles, which can fit their electronic and optical properties. To improve the electronic, optical properties and morphology of the perovskite nanoparticles, they can be easily customized by managing the experimental conditions precisely including precursor concentration, reaction time and temperature. There are a variety of approaches to synthesize the perovskite nanoparticles namely colloidal, emulsion process, and so on.

#### **1.4.3. Applications of nanostructure perovskite**

The perovskite material processing and compositions approaches, with the favorable electrical and optical properties, opens potential applications for metal halide perovskites. These potential applications are including photovoltaic and photovoltaic beyond.

##### **1.4.3.1. Photovoltaics applications of perovskites**

The perovskites materials were demonstrated as a perfect replacement with dye molecules in dye-sensitized photovoltaics, because of their broad absorption spectrum and high absorption coefficient. However, it is realized that the perovskites are excellent semiconductor materials, different from organic absorber and dye molecules, and more

dependent on the inorganic semiconductors for photovoltaic applications including GaAs or Si.

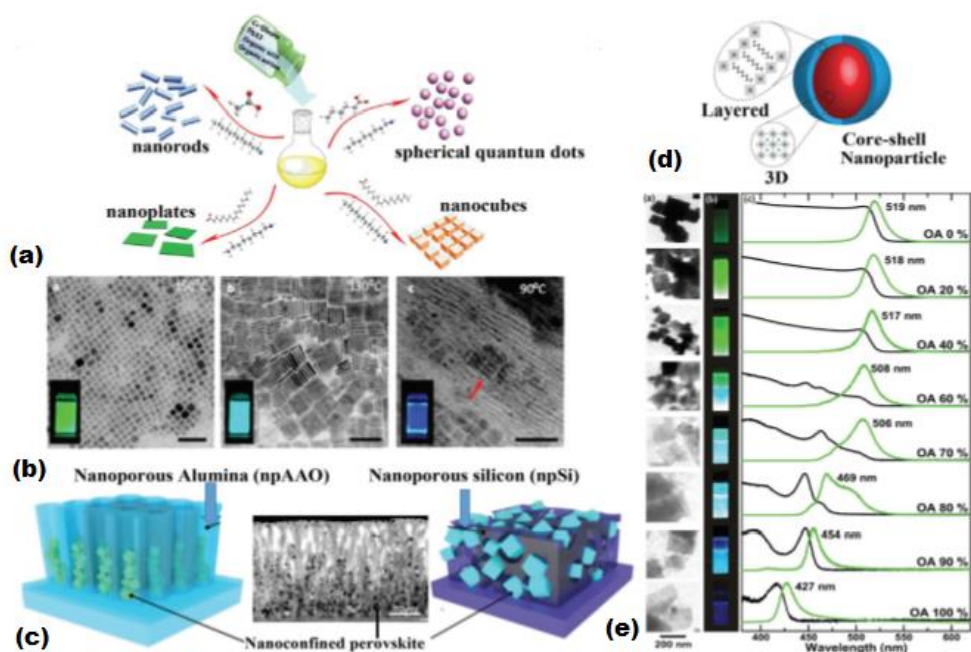


Figure 1.16 (a) the formation of  $\text{CsPbX}_3$  ( $X=\text{I, Br, Cl}$ ) nanoparticles mediated by amine and organic ligands. (b) Effect of reaction temperature at (i)  $150^\circ\text{C}$ , (ii)  $130^\circ\text{C}$ , (iii)  $90^\circ\text{C}$ . (c) The nanostructure film templates for nanoporous silicon and alumina infused with perovskite nanoparticles with SEM. (d) Schematics illustration of core-shell of octyl ammonium lead bromide nanomaterials over  $\text{MAPbBr}_3$  nanoparticles. (e) TEM images of nanostructures, and the perovskite suspension under UV light, and UV-vis and photoluminescence spectra of perovskite [42].

Perovskite materials have considerable performance and long carrier diffusion length in layer heterojunction structures, where an i-type perovskite layer film is sandwiched between a p-type hole transport layer and n-type electron transport layer. This structure has been led to the current density voltage curve (J-V) measured power conversion efficiency. The n-i-p architecture has a J-V curve demonstrated a large hysteresis. The hysteresis originates from an accident of mobile ionic and electronic species, and is not because of ferroelectricity. To decrease hysteresis, a mesoporous  $\text{TiO}_2$  can be deposited in the devices with highest efficiency [43]. It has been illustrated that the active mesoporous layer offers a high surface area for enabling electron collection and to make more favorable charge extraction in perovskites within this area, which act as filler for the electronic trap sites at this interface collection of negatively charge. To decrease the hysteresis, a solution is replacing a n-type



organic collection layer with n-type TiO<sub>2</sub> layer and promotion by an inverted p-i-n perovskite structure. It has been demonstrated that structures with an n-type organic fullerene charge collection layer demonstrates an insignificant hysteresis in J-V curves. It has been indicated that a big density of surface defect can be created at the interface between perovskites and the TiO<sub>2</sub> layers, whereas the organic layers appear no to suppose such a high density of defects. Additionally, such structures inherit the benefits of organic solar cells: easy processing of tuning the alignment of the energy level, and interfaces low temperature. It has been depicted that the TiO<sub>2</sub> structure efficiency can be enhanced by organic contacted structure. The tandem solar cells based on CIGS, silicon, and perovskites are a suitable method to deliver cost-effective solar technology that would compete with current technologies. To compare with silicon-based solar cells, the main properties of wafer-based solar cells are the need for lack of aesthetic versatility and a heavy rigid format, especially when a semitransparent application is considering. On the other hand, perovskite solar cell can process on different materials via either vapor phase or solution processing, and already have used with a high efficient flexible substrate. As illustrated in figure 1.17a silicon solar cells with space-related at 1 Wg<sup>-1</sup> which have been used to power a model airplane, compared with very light-weight perovskite photovoltaics with a power to weight ratio of 23 Wg<sup>-1</sup>. Particularly, this can be a demonstration of the future technologies that can be enabled by very light-weight and high-performance perovskite solar cells; this also would be very suitable for air vehicle transportations industries and space applications. For building-integrated photovoltaics applications, perovskite photovoltaics can also be manufactured to be colorful or semitransparent, or even fabricated into photovoltachromic self-tinting systems, as illustrated in figure 1.17 b and c respectively.

#### **1.4.3.2. Applications beyond photovoltaic**

The potential applications beyond photovoltaics referred to different types of semiconductor systems including photodetectors, light-emitting diodes (LEDs), and thin-film transistors (TFTs).

##### **1.4.3.2.1. Photodetectors**

A high quality photovoltaic is able to function as a photodetector. Photodetector based transistors have been demonstrated by employing the perovskites photoconductivity. A

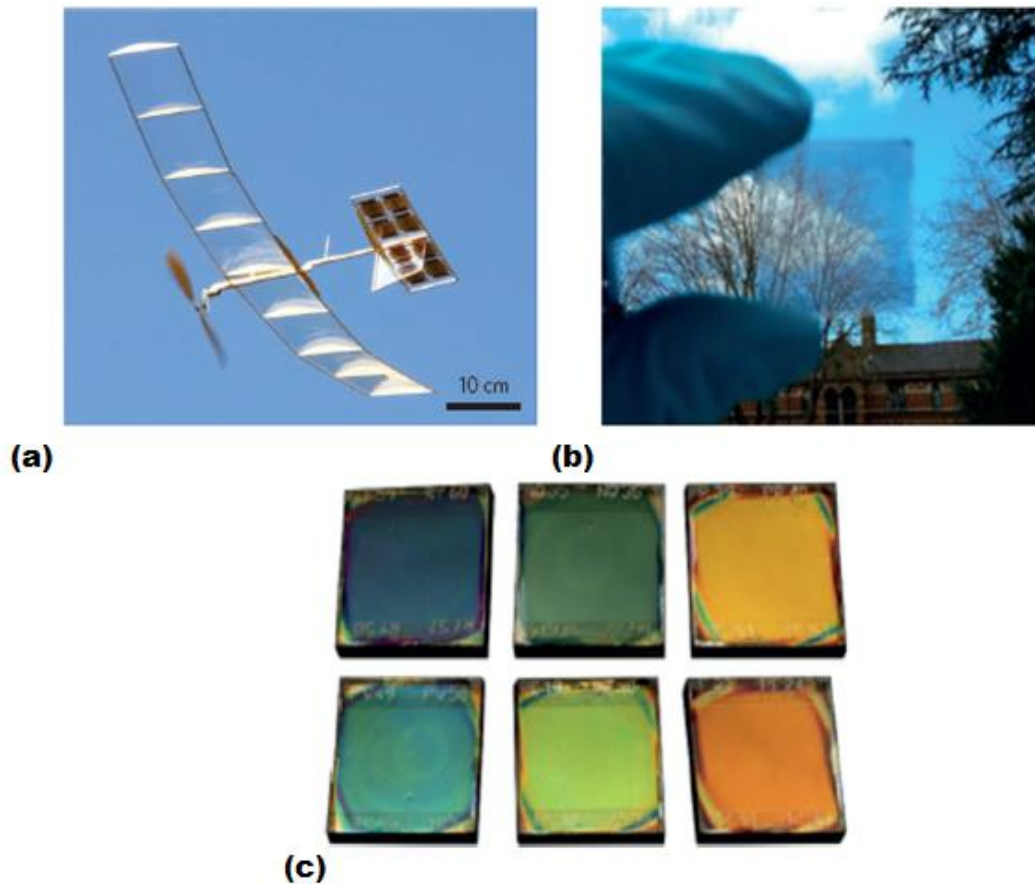


Figure 1.17 Applications of photovoltaic halide perovskite. (a) A model plane powered by metal halide perovskite photovoltaics. (b) Picture of a normal colored semitransparent perovskite film fabricated on glass using controlled dewetting. (c) Photonic crystal scaffolds with colorful perovskite solar cells [43].

high-performance photodetector has been reported from hybrid perovskite photovoltaic cells [44] (figure 1.18a) which has a conversion efficiency of 12% under normal 1 sun condition. Figure 1.18b also illustrates a high detectivity near to 1114 Jones, that is better than of the conventional silicon photodetectors with the same working wavelength. A perfect photodetector must show an exceedingly fast interaction to the incident photon beam. In solar cell photodetectors, the film thickness is about several hundreds of nanometers, and because the charge diffusion length in perovskite crystals films has the same order, both fast responses and high efficiency can be observed. The second most important effect of system structure on photodetector efficiency is related to the hysteresis behavior of perovskite photovoltaics. Therefore, to clarify the real behavior of the hysteresis

at this point, any delay for the light photo-response excitation must be minimized dramatically. For a p—i—n system architecture using a perovskite as the intrinsic layer, a fullerene as an n-type layer, and a polyelectrolyte as the p-type layer, photo-response times are about 300 ns. Consequently, it has been depicted that hysteresis strongly depends upon perovskite interfacial contact with control charge carrier layers. When a perovskite intrinsic layer is sandwiched in an n—i—p architecture, for which the p-type layer is doped Spiro-MeOTAD and a n-type layer is a material oxide (ZnO or TiO<sub>2</sub>), the response time delay of 0.1-30 S have been obtained. At a wavelength of 365 nm, a very high photoresponsivity has been reported [45]. From the cathode side, such photo-response shows a strong light supposed charge injection related to the slow response of trap filling processes happening at the interface. Importantly, it is noting that the mentioned photodetectors show higher photoresponsivity as the large channel width is able to position high photocurrent. However, the photoresponse speed is strongly influenced by the charge transport distance, the channel size should finally be the barrier factor. To reduce the response time, decreasing the channel size to micrometer would be a useful solution. For improving photodetectors efficiencies, the perovskites hybrid materials would be a promising method.

#### **1.4.3.2.2. Light emitting diodes (LEDs) and laser**

The Shockly-Queisser limit describes that an ideal solar cell compound shows radiative recombination rate. Hybrid perovskites have been depicted a very high near 70% PLQY at room temperature and at 195 K reaching to 100%. This not only suggests a strong application for light-emitting diodes but explains the high photovoltaic efficiency. A bright electroluminescence perovskite has been reported [45]. By adjusting the perovskite layer composition, the emission color can be changed. For example, the MAPbI<sub>3</sub> can emit a light near 780 nm wavelength. By replacing the iodine with bromide, the emission also change from red color to green color. To confine the recombination through the structure, a sandwich and QW structures were offered with a perfect electroluminescence quantum efficiency of about 0.8% as depicted in figure 1.19. The perovskite film is sandwiched between a polymer as a HTL and a TiO<sub>2</sub> as a ETL that can efficiently charge injection [46]. Due to high film quality, the hybrid perovskite materials have high PLQY. Additionally, the photoluminescence lifetime is only a few nanoseconds for direct band gap semiconductors including GaAs, shorter than perovskite semiconductor which is about a few hundred seconds. A laser system can be manufactured by low-cost processes, made them highly

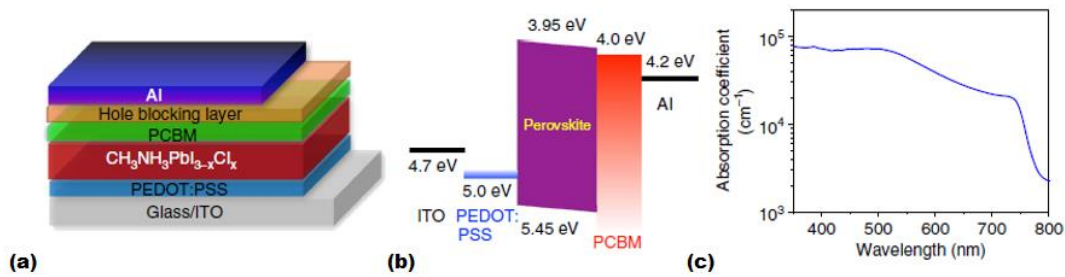


Figure 1.18. Perovskite photodetectors. (a) the device structure of perovskite photodetector. (b) Bandgap energy diagram perovskite photodetector. (c) UV-vis absorption spectra of the photodetector without the Al layer and hole-blocking layer [44].

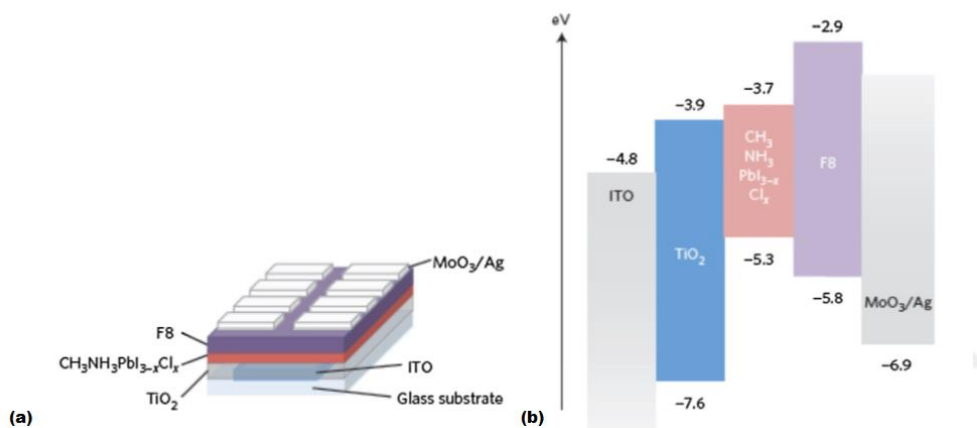


Figure 1.19. Sandwiched structure and energy level schematic of perovskite LED. (a) The device structure of the MAPbI<sub>3-x</sub>Cl<sub>x</sub>. (b) Energy level schematic of different layers of materials in the infrared perovskite LED, depicting valence and conduction bandgap with respect to vacuum [46].

attractive as electrically pumped. The Lasing and even amplified emission phenomenon have been depicted from non-cavity and cavity modes. Figure 1.20 shows a very low threshold amplified simultaneous emission from MAPbI<sub>3</sub> films clearly. Consequently, radiative recombination with amplified simultaneous emission successfully overcomes both interfacial defects and Auger recombination. Surprisingly, it stays unclear why the amplified simultaneous emission happens on such a fast time scale (<10 ps). The quantum yields of photoluminescence emission ranging from 70% to 20%, showing that film properties are

strongly dependent to the measurement condition and processing parameters as observed for photovoltaic applications.

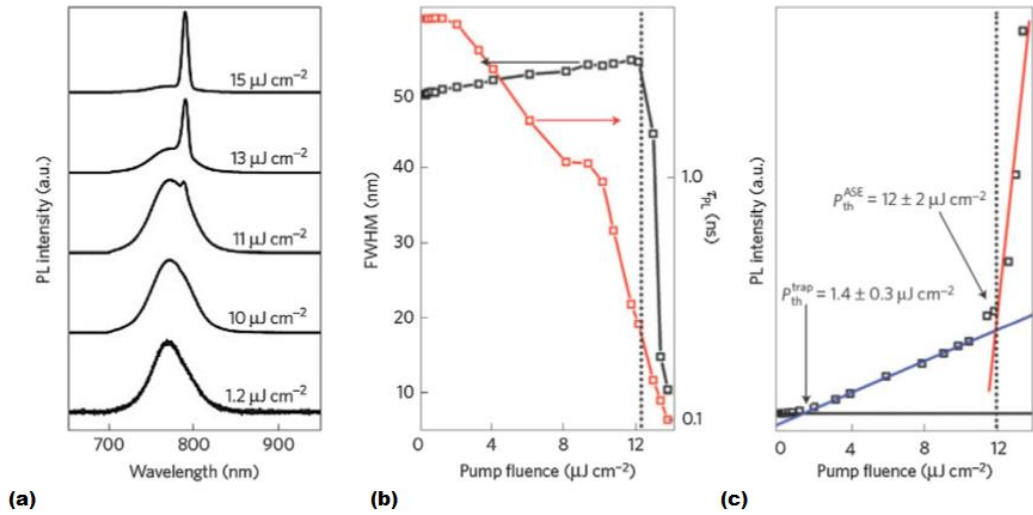


Figure 1.20. Light emission from perovskite films. (a) Photoluminescence spectra of MAPbI3 film using 1 kHz pumping pulse with increasing fluence of the pump, an illustration of transporting from simultaneous emission to amplified simultaneous emission. (b) The FWHM of the average transition photoluminescence lifetime and emission peak with respect to pump fluence. (c) Photoluminescence intensity with respect to pump fluence. The amplified simultaneous emission threshold fluence ( $P_{th}^{ASE}$ ) and the trap state saturation threshold fluence ( $P_{th}^{trap}$ ) [45].

### 1.5. Principles of Photoelectrochemical (PEC) Cells

Photoelectrochemical (PEC) water splitting has developed from simple forms, which illustrate the function of basic concepts, to develop systems, which create solar fuel production efficiencies. In general, there are four steps in a completed solar water splitting process. The first two steps are associated with photon light photoexcitation and absorption, whereas the last two steps are related to photogenerated charges including surface reaction and charge separation. Regardless of the complexed structures of the cells, at least one of the electrodes which form the photo absorber is a semiconductor. It can absorb photons and convert them into hole-electron pairs to feed power to all systems. Afterward, junctions participate in gradient electrical or/and chemical potentials, vertically separate holes and electrons. Nevertheless, efficient use of solar energy could decrease many environmental and energy issues, because it is irradiating the surface of the Earth ( $1.3 \cdot 10^5$  TW) increases

the current global human energy consumption. Therefore, to fabricate renewable hydrogen in large scale, splitting water molecules under sunlight has received much attention. Because it was discovered in the early 1970s [47], that illustrated as a photoassisted water oxidation method using a photoanode single crystal  $\text{TiO}_2$  by band gap excitation, PEC and photocatalytic on semiconductor materials. The hydrogen production by sunlight will play a significant role in the future of sustainable energy. Since it is transportable, storable and using a fuel cell it can be convert into electricity. In addition, the hydrogen can recycle the  $\text{CO}_2$  gas using some chemical processes including methanol synthesis and the Fischer-Tropsch. The PEC reaction for splitting water molecules is a difficult process in which the reaction Gibbs free energy can increase by 237 KJ/mol. To derive PEC and Photocatalytic splitting of water, the requirement energy is provided by natural sunlight. Figure 1.21 depicts the reaction processes of photocatalytic system. Inside the semiconductors photo-catalyst, the holes and electrons are created by band gap excitation. The photo-excited charges are transferred to the photo-catalyst surface active sites with the aim of consuming by redox reactions of the surface. The mass diffusion of products and reactants must proceed simultaneously. Therefore, for successfully splitting of water molecules the redox reaction on their surface and the charge separation in photo-catalyst particles should proceed within the lifetime of photo-excited carriers. In most cases, the photo-excited carriers undergo recombination process. In order to simplify the surface reaction and charge separation, photo-electrodes and photo-catalysts are modified with suitable buffer and co-catalysts layers.

### **1.5.1. The Thermodynamics of photoelectrochemical and photocatalytic water splitting**

When a semiconductor is irradiated to light, it can absorb higher than band gap energies photons, the valence band (VB) electrons are excited to the conduction band (CB). Consequently, exciting holes and electrons are created in the VB and CB, respectively. If the injected charges into the reactants are thermodynamically desired, these photogenerated carriers can control oxidation and reduction reactions. To attain photocatalytic splitting of water using a photocatalyst, the band gap of the photocatalyst should mount the oxidation (+1.23 V) and reduction (+0 V) potential of water, as depicted in figure 1.22a which is the one-step splitting of water process. As depicted in figure 1.22b, the semiconductors linked with reverse redox shuttle in series. In this plot, the oxidation of reduced redox mediators

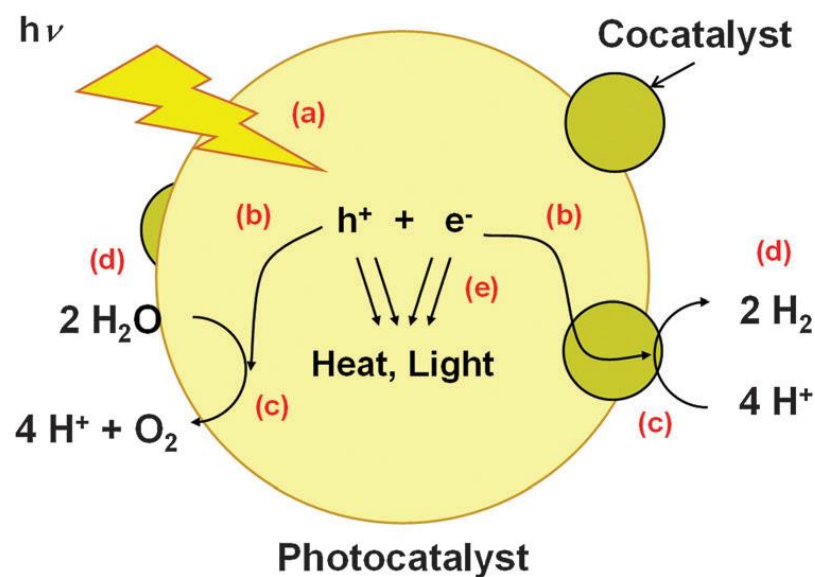


Figure 1.21. Water splitting reaction on a heterogeneous photocatalyst. (a) sunlight absorption, (b) charge transfer, (c) redox reactions, (d) desorption, adsorption, and mass diffusion of species, and (e) charge recombination [48].

and reduction of water to hydrogen happen on one photocatalyst at the same time with the oxidation of water to oxygen and reduction of oxidized redox mediators occur on the other photocatalyst. The mentioned photocatalytic device is defined as “Z-scheme” due to the similarity in the transfer and excitation photoexcited processes of electrons to photosynthesis in plants. In some cases, the splitting of water can be carried out even in the lack of reversible redox shuttles due to the interparticle transfer of electron during the physical contact between the oxygen and hydrogen evolution. Inside an electrolyte, the electrodes start to transfer the electron between the electrolyte solution and the semiconductors until equilibration of the Fermi level with the redox potential of the electrolyte. Therefore, an electrolyte solution donates electrons to a photocatalyst when the Fermi level of the photocatalyst is more positive than the reduction potential of the electrolyte solution and vice versa. Because the band positions at the interface can be supposed to be pinned and the electrons density in a semiconductor is finite, the band bending caused by the electron moving. The band bending can also take place in semiconductor dispersed in an aqueous solution, however it can affect nanomaterials in the case that the thickness of the space charge could be more than the structure sizes. Therefore, it plays a significant role in the separation of the charges. As depicted in figure 1.23c, in photoanodes (n-type semiconductor electrode), the photoexcited holes collect on the photoanode surface and are participating in reactions oxidation, while electrons transfer via

an external circuit to a counter electrode and the back contact, then consumed in reactions reduction. To generate oxygen at photoanode, the top of the VB must be more positive than the potential of the oxygen evolution. Nevertheless, the photocathode (p-type semiconductor) uses for hydrogen evolution when the CB edge is more negative than the potential of the hydrogen evolution (figure 1.23d). In both cases, the photoexcited minority carriers drive PEC reaction on photoelectrodes. Therefore, under photoexcitation, the electrons on counter electrode has the potential as the same as the photoelectrode Fermi level. To compensate the potential shortage, between a photoelectrode and a counter an external voltage can be applied. In that case, when the energy conversion efficiency is considered, the input power should be reduced from the energy output. Alternatively, a photocathode and a photoanode can be linked in a tandem device as in Z-scheme splitting of water (figure 1.22e) instead of utilizing a counter electrode and a single photoelectrode. In that tandem devices, the working potential of the photoelectrodes and the maximum photocurrent can be theoretically calculated.

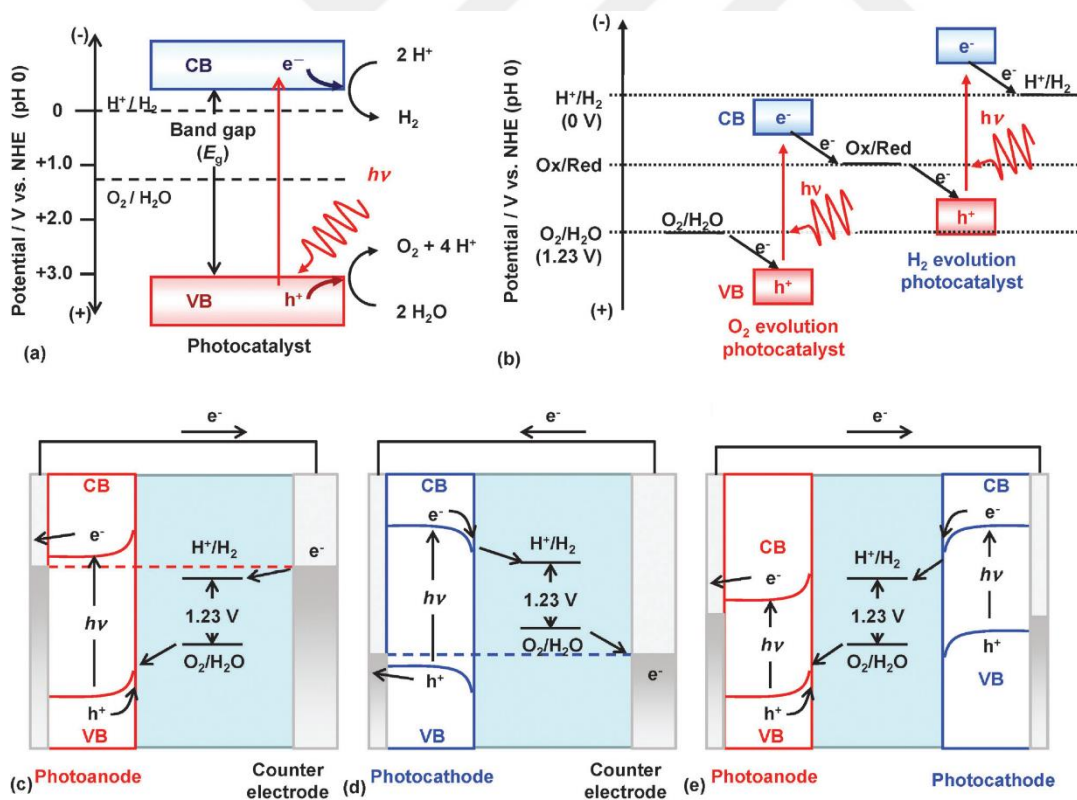


Figure 1.22. Energy diagrams of photocatalytic water splitting on (a) one step excitation, (b) two-step excitation or Z-scheme, and water splitting using PEC (c) photoanode, (d) photocathode, (e) tandem device [48].



## **2. SYNTHESIS AND CHARACTERIZATION OF FABRICATED SEMICONDUCTOR**

### **2.1. Chemical Synthesis of Nanostructured Thin Film**

Synthesis of nanostructured materials via chemical methods has been found to be most versatile, not only in the majority of materials that can be formed, but also in the difference of morphologies in which they can be obtained without using lithographic methods, and in the variety of methods through which fabrication can be implemented. The main chemically synthesis of nanostructured thin films are including chemical bath deposition (CBD), sol-gel, hydrothermally, spin coating, and so on.

### **2.2. Chemical Bath Deposition (CBD) Synthesis Method**

Chemical bath deposition synthesis of nanostructured thin film has attracted the attention of scientists and researchers today because of its commercial production and large area scaling, replicability, simplicity, and convenience. CBD technique has been used for the synthesis of ternary, oxides, selenides and sulfides compound. The selection of this method arises from its simplicity of instruments for deposition, the possibility of application on a large surface, ease of handling, and its low cost. Hence it is most appropriate instead of other fabrication methods including CVD, MBE, PLD, and so on which are very expensive instruments. CBD technique also offers a means of fabrication large area sample, which can be a technology readily adaptable for industrial fabrication. The properties of fabricated materials can be controlled and varied by proper optimization of the chemical baths and deposition conditions. To deposit a thin film on substrates via CBD, a certain volume of the bath solution is provided. The resulting solution is well stirred and the material layer, which was previously degreased, is clamped vertically into the solution inside a beaker as depicted in figure 2.1. Then by controlling the time and the temperature of the bath, the structure becomes ready for the next works. In the CBD synthesis of oxides, the chalcogenide source is water, therefore tighter control must be exerted over just temperature and PH parameters to reach a similar point of control over the rate of hydrolysis and by implication, control over the properties and thin film microstructure [49].

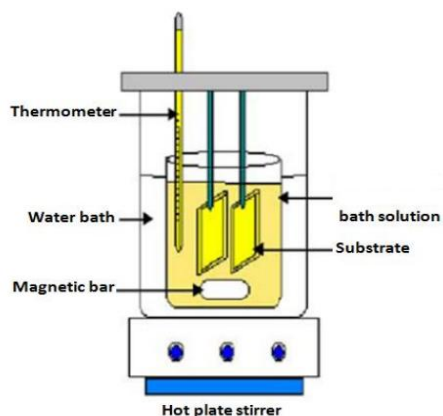


Figure 2.1 CBD synthesis of nanostructured layers, with the system components [50].

### 2.3. Synthesis of the Nanostructured Thin Film via Spin Coating

This approach is used to deposit uniform coatings of organic materials on different types of a flat surface using a spin coater device. It has been designed by Emslie and Meyerhofer in 1958. Nowadays, the spin coating approach could be used as one of the best deposition techniques since, it is a simple, fast and cheap approach for fabrication homogeneous samples. Furthermore, this approach also has great benefit to develop extremely uniform layers of samples on different layers of substrates. The width of thin film is mainly controlled by several factors including viscosity and spin speed. A certain thickness can be achieved using a liquid precursor through a spin coating approach. Spinner (or spin coater) is the device that is used for the spin coating process. There are plenty of key stages including fluid dispense, stable fluid outflow, spin up, and evaporation in order to provide thin film by using a spin coating approach. In the spin coating process, first of all, the target substrate rotates while distributing the fluid onto the sample. Secondly, a certain quantity of a solution is dropping on the targeted substrate, then the targeted substrate is rotating in order to spread the solution on the targeted substrate. The quantity of solution and speed of a rotor play an pivotal role on the properties of the thin films. The limitation and advantages of this technique are listed in table 2.1 [51].

Table 2.1 Advantages and Limitation of Spin Coating Synthesis Method.

Limitation	Advantages
The size and costs of targeted substrates affected the working of spin coaters.	It can be used in antireflection, flat screen and conductive oxide display coatings.
Less material efficiency	Film thickness can be controlled and varied through changing spin speed.
It is considered a slow-developing method since only a single targeted substrate can be used at a time.	This method can be also used for etching and cleaning.
In nanotechnologies, it is working performances become low because of fast-drying processes	Most substrates used can be wafers, small pieces, and micro-scope slides.
	Spin coating processes can be mostly used in the semiconductor industry, where thin films with a thickness of less than 11 nm can be fabricated for many applications.
	It is a fast and low-cost technique as compared to other techniques.
	It is an easy and simple approach.

## 2.4. Experimentally Semiconductor Synthesis

### 2.4.1. Nanostructured ZnO

The nanostructured ZnO film photoelectrodes have been fabricated on the hydrophilic chemically treated fluorine doped tin oxide (FTO) coated glass substrate using CBD. First of all, the FTO coated glass structure were cleaned by sonication inalconox solution, acetone, and water for 10 min each, respectively. To chemically treatment, the FTO coated glass samples were placed in an ultrasonic device bath of a mixture of 40 ml of 1.0 M of an aqueous solution of potassium hydroxide (KOH) and 60 ml of isopropanol for 3 minutes, followed by immersing them in deionized water (D.I.W) with sonication for 10 minutes. CBD synthesis of the ZnO nanostructured film has been carried out in the chemical bath solutions containing zinc acetate dihydrate ( $\text{Zn}(\text{CH}_3\text{COO})_2 \cdot 2\text{H}_2\text{O}$ ) as the zinc source. First of all, 0.05 M of  $\text{Zn}(\text{CH}_3\text{COO})_2 \cdot 2\text{H}_2\text{O}$  and 1.0 M of urea ( $(\text{NH}_2)_2\text{CO}$ ) in D.I.W have been provided. After that, by

using an acetic acid solution, the PH of the solution bath was adjusted to 4.8. Then, in order to form  $Zn_4CO_3(OH)_6$  complex, the glass samples were immersed into the prepared solution vertically and kept in an oven for 3 hours at 80°C. Finally, the samples were calcinated at 300 °C for 30 minutes to convert the chemical structures of  $Zn_4CO_3(OH)_6$  complex to ZnO nanostructures. Figure 2.2 represents the ZnO solution and the ZnO layer deposited on FTO glass. Table 2.2 depicts the composition of ZnO structures under EDX. The EDX elemental distribution depicted higher atomic value for Zn than O element. The presence of carbon also depicted due to the presence of urea in the synthesis procedure of the ZnO nanostructures.

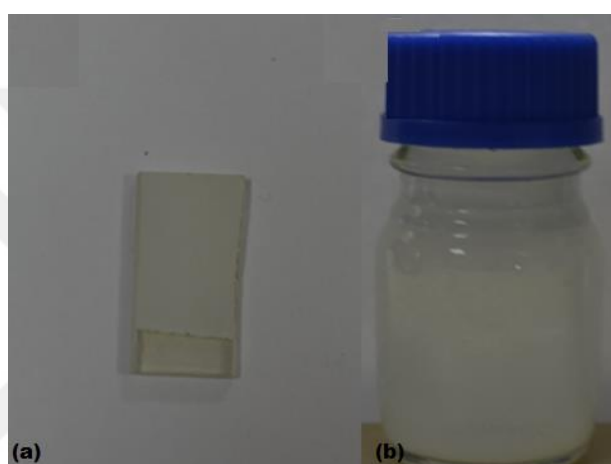


Figure 2.2 (a) The ZnO nanostructured on FTO, (b) ZnO synthesis solution.

Table 2.2 The Elemental EDX of ZnO.

Element	Weight%	Atomic%
Zn	94.33	79.88
O	5.23	18.11
C	0.44	2.01
Total	100	100

#### 2.4.2. ZnO/CdS structure fabrication

The CdS heterostructure layer was also synthesized by the CBD approach. The as-prepared ZnO nanostructure substrate was immersed into the aqueous solution consisting of 0.01 mM of cadmium nitrate tetrahydrate ( $Cd(NO_3)_2 \cdot 4H_2O$ ) and 0.01 mM of thioacetamide

(CH<sub>3</sub>CSNH<sub>2</sub>). Then, the solution bath temperature was increased to 60 °C for 30 minutes. Figure 2.3 represents ZnO/CdS structure, and table 2.3 also depicts the EDX composition of the synthesized ZnO/CdS structure. Table 2.3 represents the elemental composition of the ZnO/CdS structure. The EDX atomic composition depicted approximately evenly atomic compositions for Cd and S elements in the structure surface.

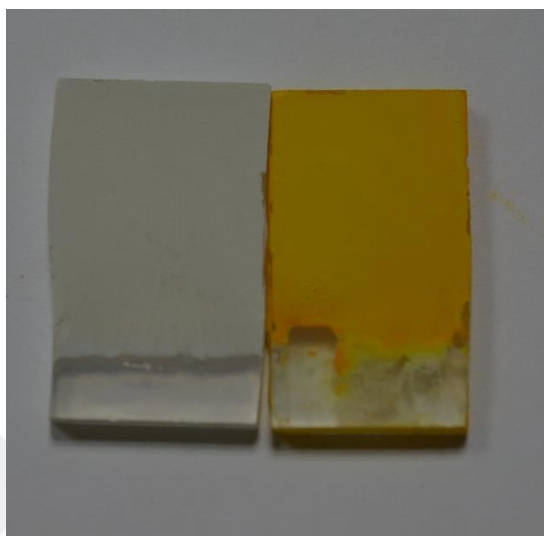


Figure 2.3 The ZnO structure (left) and CdS layer synthesized on ZnO structure (right).

Table 2.3 The Elemental EDX of ZnO/CdS.

Element	Weight%	Atomic %
Zn	44.61	41.09
Cd	40.68	21.79
S	10.07	18.9
O	4.02	15.14
C	0.62	3.08
Total	100	100

#### 2.4.3. ZnO/CdSe and ZnO/CdS/CdSe structures synthesis

The CdSe heterostructure layers were also synthesized on ZnO and ZnO/CdS layers by the CBD approach. The as-prepared ZnO and ZnO/CdS nanostructure substrates were immersed separately into the aqueous solution consisting of 0.0016 mM of cadmium nitrate tetrahydrate (Cd(NO<sub>3</sub>)<sub>2</sub> · 4 H<sub>2</sub>O), 1 ml of diethylene glycol as a stabilizer, and 8 ml of as

prepared selenium precursor  $\text{NaSeSO}_3$ . Next, the solution bath temperature was raised to  $80^\circ\text{C}$  for 1 hour. The deposition process was repeated three times. Figure 2.4 represents the deposited CdSe layer on the ZnO and ZnO/CdS structures. And the table 2.4 depicts the elemental compositions of the fabricated structures under EDX. For Cd and Se elements there is approximately evenly distribution on the surface of the structures.

The selenium precursor was prepared by dissolving 5 mmol selenium powder and 14.1 mmol of sodium sulfate ( $\text{Na}_2\text{SO}_3$ ) in 100 ml of D.I.W at  $80^\circ\text{C}$  under reflux for 24 hours to get a clear solution.



Figure 2.4 (a) the structure of ZnO/CdS/CdSe (left) and ZnO/CdSe (right), (b) CdSe synthesis solution.

Table 2.4 The Elemental EDX of ZnO/CdSe.

Element	Weight %	Atomic %
Zn	64.83	50.22
Cd	11.62	5.24
Se	11.89	7.62
O	11.66	36.92
Total	100	100

#### 2.4.4. ZnO/CsPbBr<sub>3</sub> structure synthesis

CspbBr<sub>3</sub> precursor solutions were provided by adding  $\text{PbBr}_2$  (0.3 mmol) and  $\text{CsBr}$  (0.3 mmol) in 1 ml of dimethyl sulfoxide (DMSO) and dimethylformamide (DMF) solvents, respectively. The solutions were provided in an Ar glovebox, then dissolved at  $70^\circ\text{C}$  for 30 min and stirred

for 24 hours at room temperature. Then, solutions were transferred into the glovebox and spin-coated with 60  $\mu\text{L}$  each solution (1200 rpm for 30 s) by a one-step method. Finally, the spin-coated  $\text{CsPbBr}_3$  film was annealed at 250  $^\circ\text{C}$  for 30 min. Figure 2.5 represents the schematic of the  $\text{ZnO}/\text{CsPbBr}_3$  structure after annealing. And table 2.5 depicts the EDX composition of the synthesized  $\text{ZnO}/\text{CsPbBr}_3$  structure. Table 2.5 represents the elemental EDX of the structure. It has been depicted acceptable atomic composition for the substrates. The near amounts for Cs and Pb and near three times for Br which is accurate composition for  $\text{CsPbBr}_3$  perovskite.

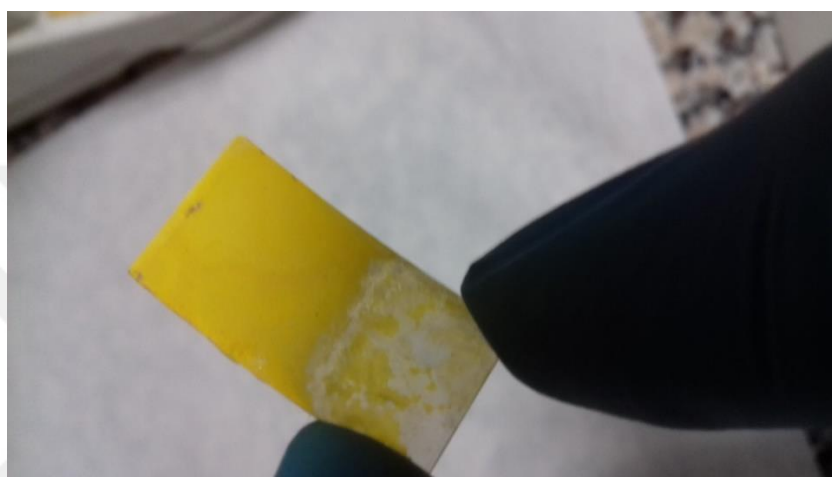


Figure 2.5 The  $\text{ZnO}/\text{CsPbBr}_3$  structure.

Table 2.5 The elemental EDX of  $\text{ZnO}/\text{CsPbBr}_3$ .

Element	Weight %	Atomic %
Zn	37.82	39.82
Br	21.69	18.68
Cs	17.33	08.98
Pb	16.90	05.61
O	06.26	26.91
Total	100	100

## 2.5. Thermally post treatment of the $\text{ZnO}/\text{CdS}/\text{CdSe}$ and $\text{ZnO}/\text{CdS}$ structures

After synthesis completion, the  $\text{ZnO}/\text{CdS}/\text{CdSe}$  and  $\text{ZnO}/\text{CdS}$  structures were thermally annealed at 200  $^\circ\text{C}$  for 3 hours in an oven. All analyses have been repeated also on the treated structures and the results would be discussed in the results and discussion section.

## 2.6. Photoelectrochemical (PEC) System and Electrolyte

The PEC performance of the photoanode structures with an area of approximately 1.0 cm<sup>2</sup> has been experimentally analyzed with a mixture of aqueous 0.35 M of Na<sub>2</sub>SO<sub>3</sub> and 0.25 M of Na<sub>2</sub>S electrolyte solutions with PH of 12.5 and using a conventional three-electrode quartz cell system. The silver paste was used for contacting copper wires on FTO for electrode connection. By using an epoxy resin, the back and silver contacts of the photoanode structures were isolated. Gamry 750 Potentiostat system was used for analyzing the current density of the photoanode structures with respect to applied potential in the range of +1.0 to -1.0 V. Finally, Ag/AgCl electrode and platinum sheet have been used as reference and counter electrodes. As depicted in figure 2.6, the AM 1.5 standard light system used in PEC analysis.

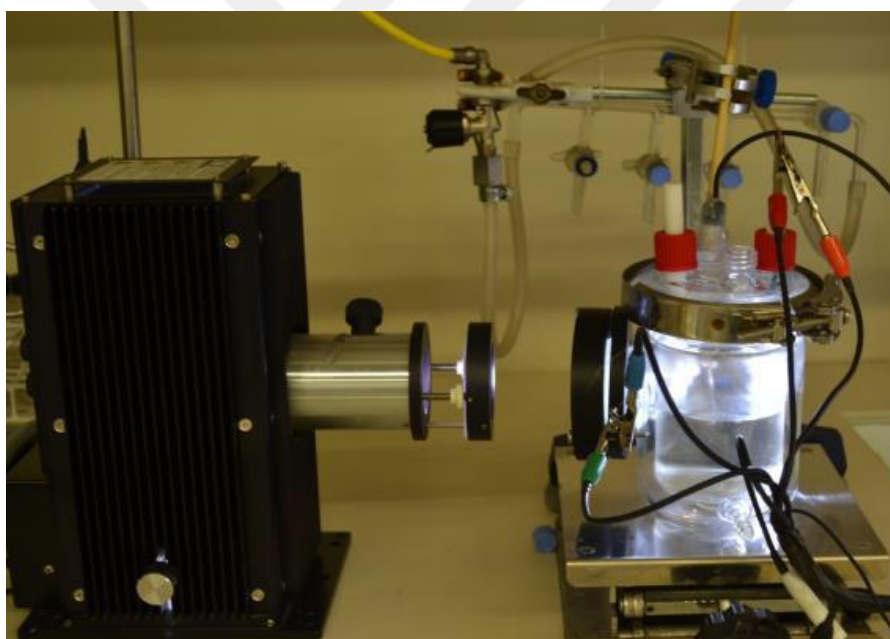


Figure 2.6. The schematic of experimental PEC process. The left device is the AM1.5 light source.

## 2.7. Photoluminescence (PL) and Absorbance Spectroscopy of The Structures

For investigating the optical properties of photoanode structures, PL and UV-VIS absorption spectroscopies were measured. As depicted in figure 2.7, the ZnO structure represents almost no absorption in the visible wavelength light region because of its wide bandgap of 3.2 eV. In comparison to ZnO, the absorption intensity of other structures increased apparently in the visible wavelength light region with a redshift. After the deposition of a



single CdSe and CdS shell, absorption peaks of about 660 and 480 nm were observed. Because of the lower bandgap of CdSe with respect to the CdS layer, the redshift of the CdSe deposited layer is more than the CdS deposited layer. For the ZnO/CdS/CdSe structure, it is important noting that its absorption range and intensity was increased with respect to single deposited layers. This promotion arises from the thickness and the presence of two visible wavelengths light-responsive CdSe and CdS layers, which act as a co-sensitization system. For the perovskite system, the absorption peak started from 550 nm to the Uv region with high intensity, as depicted in figure 2.9. For the PL spectroscopy of the structures (figure 2.8), absolutely there is a redshift with respect to their absorption peaks, and it is clear that by increasing the thickness of the layers the intensity of ZnO peak decreases. PL spectroscopy represents the charge separation of the film structures. The intense peak at about 380 nm for the ZnO structure represents that the ZnO structure poses a strong recombination rate with respect to other structures. However, for CdSe structures, the emission peaks were gradually decreased until 650 nm, representing that the CdSe deposition can efficiently increase the separation of photoinduced charge of the ZnO nanostructure. There are also two peaks, first at about 550 nm for all structures and more than 650 nm, which related to the charge recombination of them in the related wavelengths. The weakest intensity is related to ZnO/CdS, which is representing the efficient photoinduced charge carrier separation of the multi-heterojunction structures. For the CsPbBr<sub>3</sub> structure, sharp PL represents high quality and color emission purity. There is about 25 nm redshift with respect to the absorption spectrum, and very strong recombination at about 575 nm.

## 2.8. X-ray Photoelectron Spectroscopy (XPS)

X-ray photoelectron spectroscopy refers to the techniques based on photoelectric effect applications and defined as a development of the light quantum nature. It has been explained that when a sample is irradiated to an incident light, a photon can be absorbed by an electron and the electron leaves the material surface with a maximum kinetic energy:

$$E_k = h\nu - E_B - e\Phi \quad (2.1)$$

where  $\Phi$  is work function,  $E_B$  electron binding energy,  $\nu$  is the photon frequency, and  $E_k$  is the minimum energy required to pick up a delocalized electron from the surface of the metal. The work function acts as a surface potential barrier that prohibits the electrons of valence band from escaping.

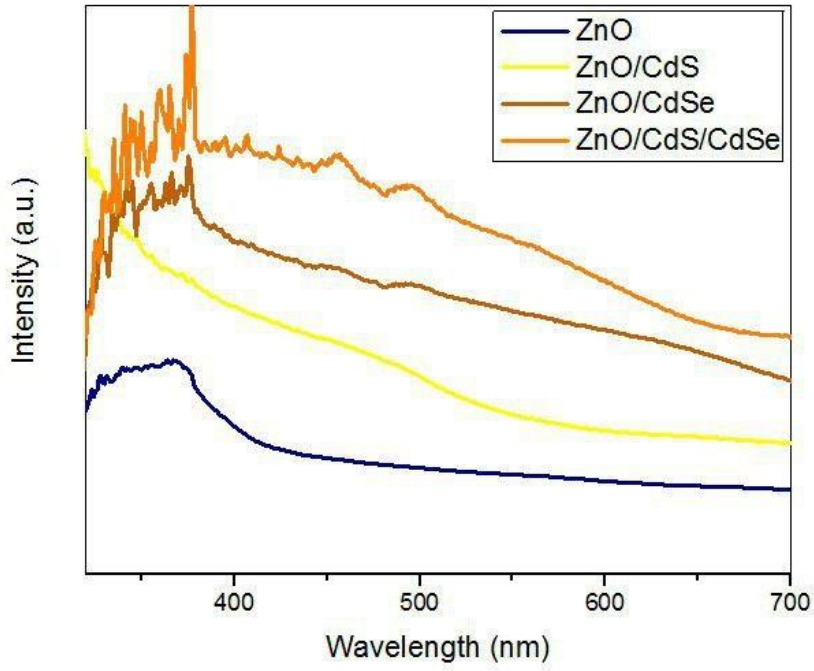


Figure 2.7 The absorption spectrum of the synthesized structures.

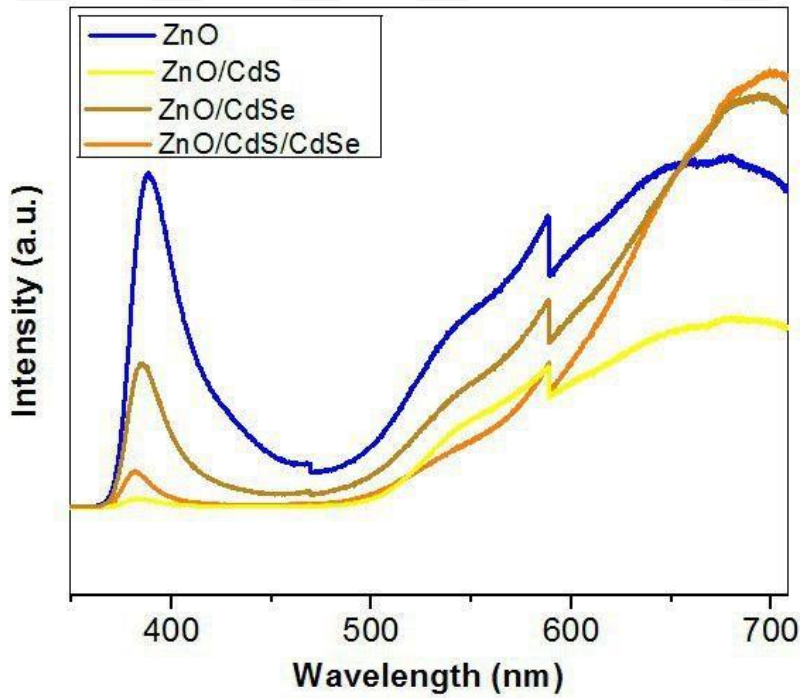


Figure 2.8 The PL spectrum of the synthesized structures.

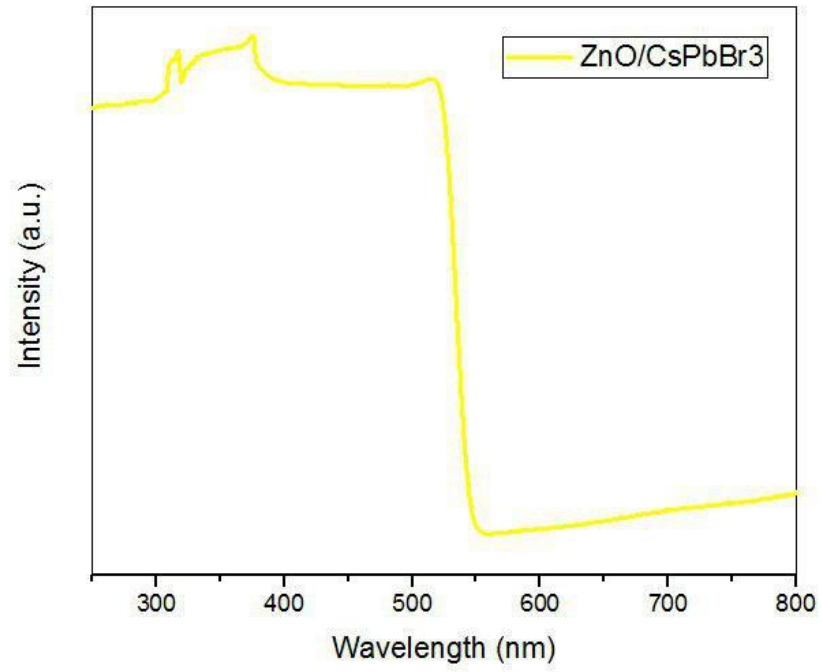


Figure 2.9 The absorption spectrum related to the CsPbBr<sub>3</sub> perovskite.

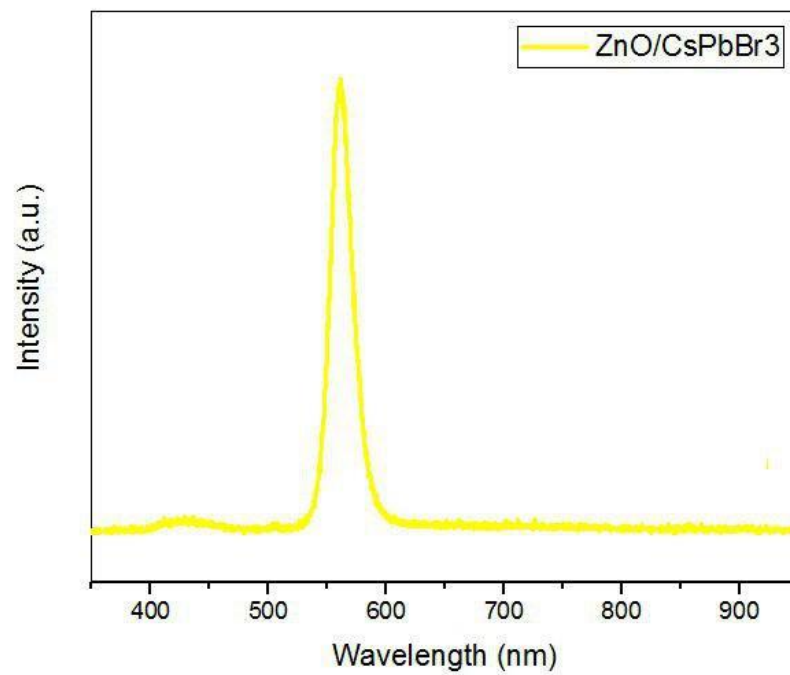


Figure 2.10 The PL spectrum related to the CsPbBr<sub>3</sub> perovskite.

The XPS can be used to explore quantum states and chemical composition of the material surface. Since the surface of a solid has different physical properties and chemical composition from the interior of the solid. An intense beam of X-ray or ultraviolet light ionizes the atoms or molecules. The light used should have enough energy to ionize electrons at least from the highest valence shell of atoms. If  $h\nu$  is higher, electrons can be diffused also to deeper levels. When photons have lower energy wavelengths such as X-ray, it can incident on the crystal surface and then core electrons can leave the atoms (Figure 2.11). Then the spectrum can be obtained by calculating the properties of electrons that leave from the surface. And this electron spectroscopy approach is called X-ray photoelectron spectroscopy (XPS).

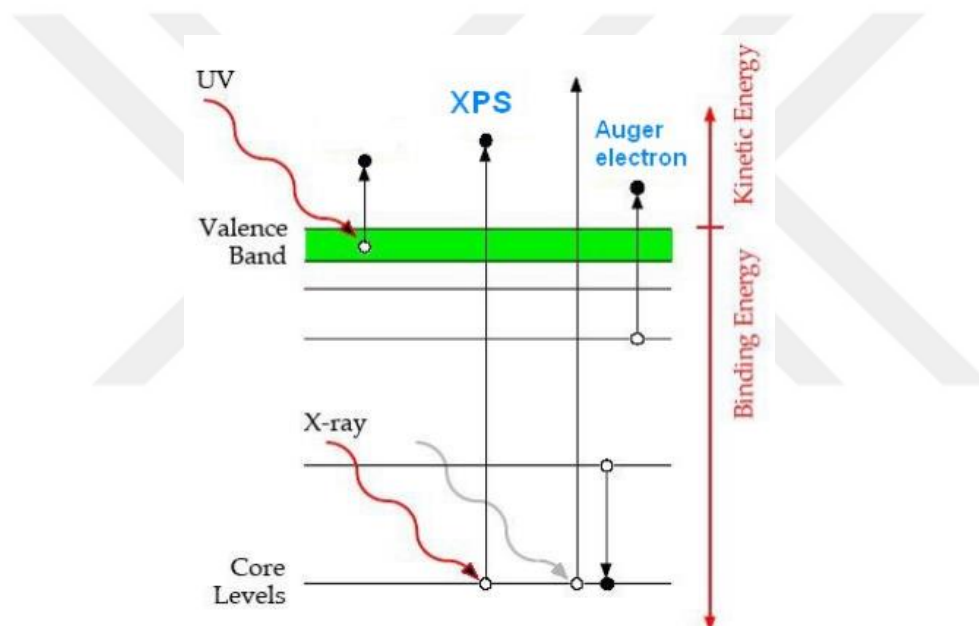


Figure 2.11 The schematic related to a photoelectron emitting due to an incident [52].

The XPS of ZnO/CdS/CdSe, ZnO/CdS, ZnO/CdSe, and ZnO structures were measured and depicted in the figures 2.12-2.14. For the ZnO structure, the surface composition and electronic states were analyzed and results depicted in figure 2.12. The XPS survey spectra is represented in figure 2.12a. The presence of only zinc and oxygen elements depicted the products high purity. The symmetric peaks with binding energies of 1044.6 eV and 1021.5 in the spectrum are related to Zn 2p<sub>1/2</sub> and Zn 2p<sub>3/2</sub> (Figure 2.12b). As depicted in figure 2.12b, the oxygen O1s peak can be divided into two peaks at about 531.8 eV and 530.9 eV, corresponding to the adsorbed O<sub>2</sub> or surface hydroxyl species and the Zn-O bonds of ZnO

which is more intense for ZnO structure. Figure 2.13 depicts the XPS of ZnO/CdS structure. By deposition of CdS layer the intensity of zinc and oxygen have been decreased and instead high intense cadmium peaks were appeared and sulfur peaks also grown as can be seen in survey figure 2.12a. The composition of zinc and oxygen in ZnO/CdS structure were the same. Figure 2.14a depicts the survey XPS for ZnO/CdSe structure. Meanwhile, the two peaks at 54.3 eV and 53.6 eV in figure 2.14 are related to Se 3d<sub>3/2</sub> and Se 3d<sub>5/2</sub>, respectively, illustrating the value state for Se<sup>2-</sup> in ZnO/CdSe photoanode structure. Figure 2.15 represents the typical survey spectrum of the ZnO/CdS/CdSe photoanode structure, which shows the coexistence of CdS, and CdSe structure, but due to high thickness of them, there is no ZnO composition in the survey.

## 2.9. X-ray Diffraction (XRD)

X-ray powder diffraction is an analytical method mainly used for identifying of the crystalline structure of materials and also it gives information on dimensions of the unit cell. To analyze the crystallinity of structure, it should be homogenized and finely ground. It has been found that for X-ray wavelength, the crystalline structures act as 3D diffraction, which is analogous to the location of different planes in crystals lattice. It is a novel method used for atomic spacing and identification of crystal structures of materials. It is also based on the interference building of a crystalline specimen and a monochromatic X-ray. Generally, these X-rays are generating by a tube of cathode ray, then filtering for the fabrication of single radiation, and directing toward the specimen. The specimen and the incident rays interaction generates a diffracted ray and interference building in which the Bragg's Law condition should be satisfied.

$$n\lambda = 2d \sin \theta \quad (2.2)$$

Where  $\lambda$  is the wavelength of the incident monochromatic X-rays (nm),  $n$  is the order of reflection,  $d$  is the interplanar location of the crystal, and  $\theta$  is the angle of incidence. This law connects the wavelength of monochromatic electromagnetic radiation to the lattice spacing and crystals diffraction angle in a structure. The diffracted monochromatic X-rays from the sample, are then detected, counted and processed. Because of the random direction of the powdered sample material, all possible diffraction orientations of the lattice must be achieved by scanning the powder sample through a  $2\theta$  angles range.

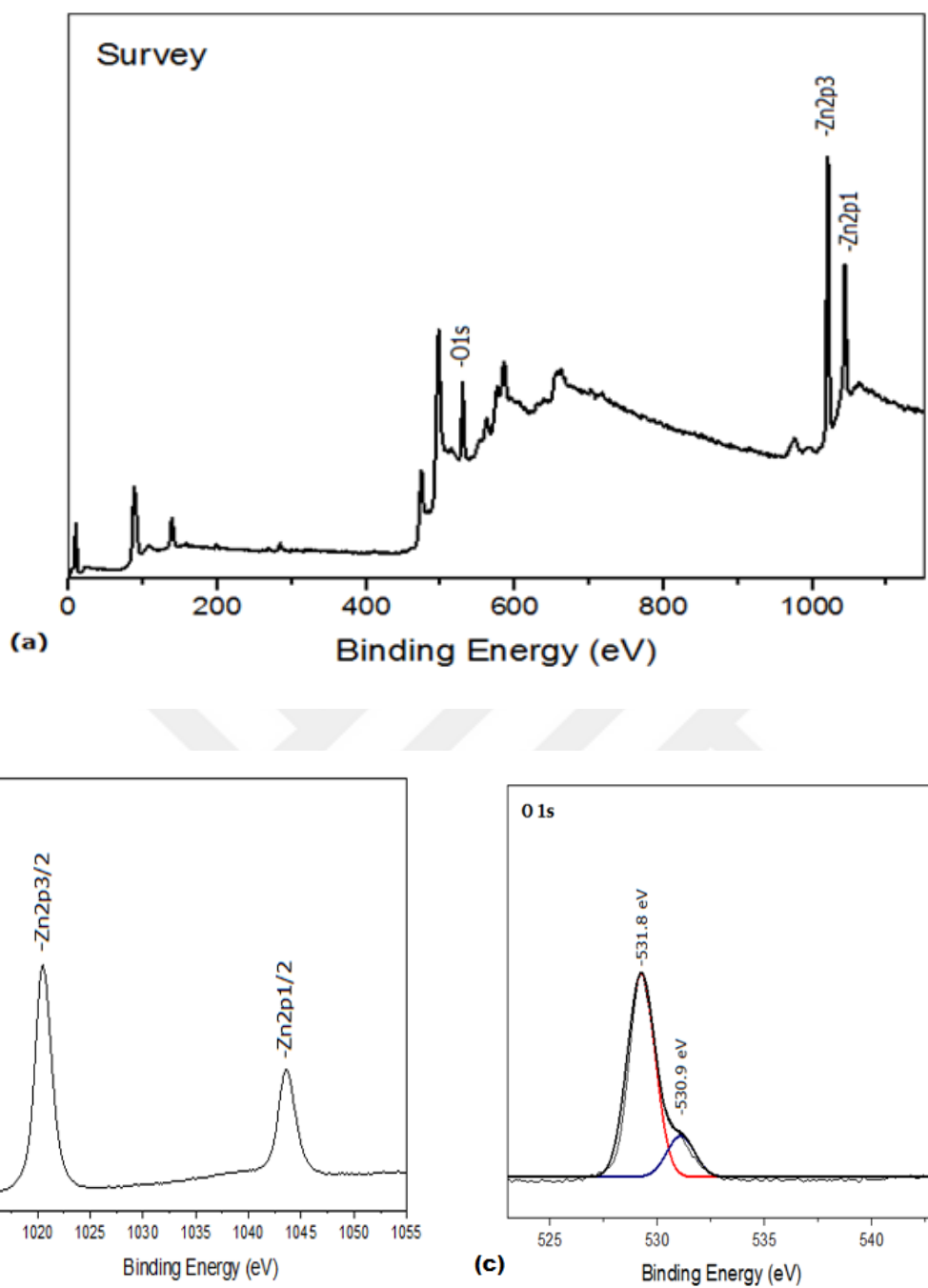


Figure 2.12 (a) the ZnO structure XPS survey spectrum, (b) Zn 2p, and (c) O 1s.

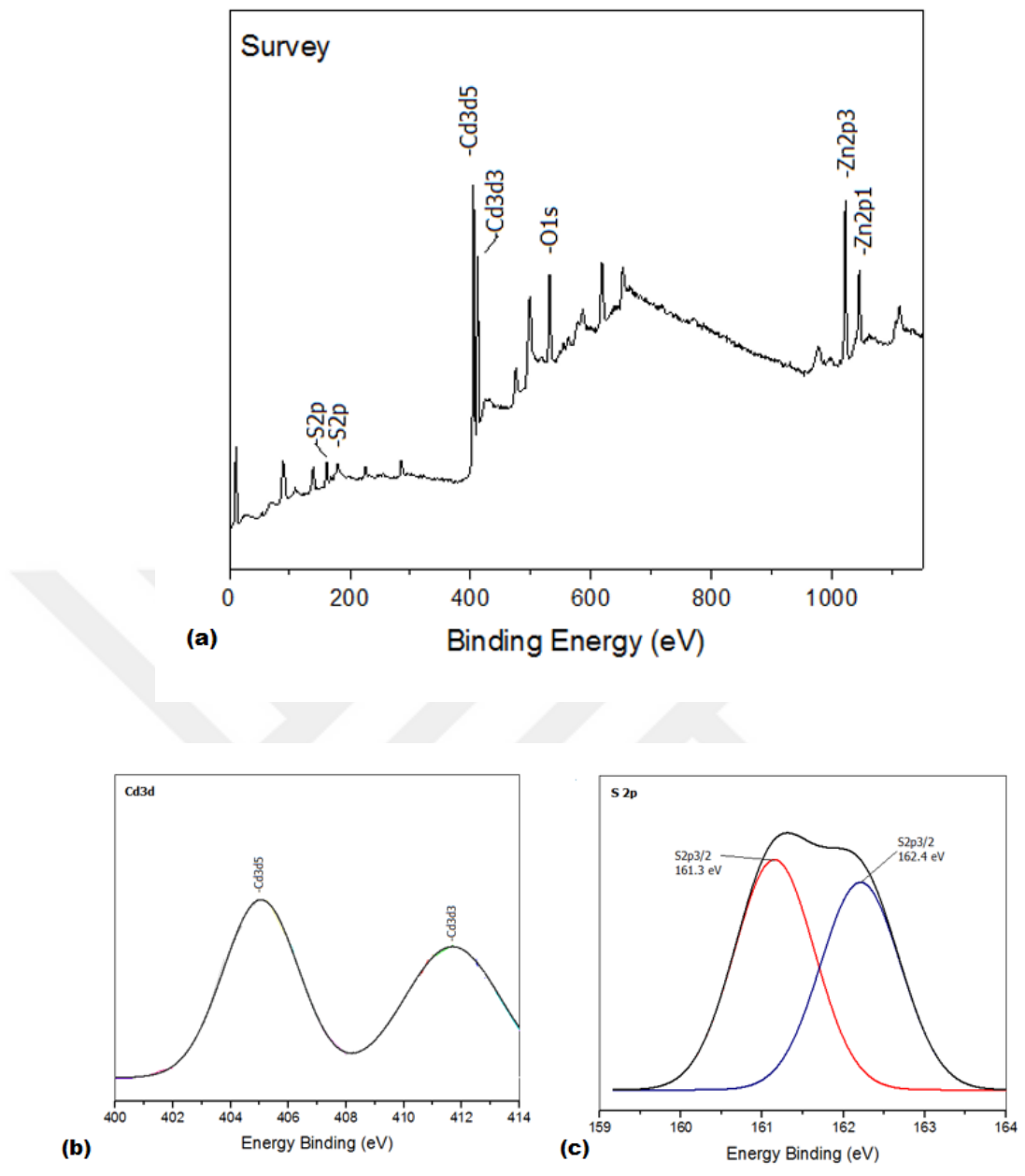


Figure 2.13 (a) the ZnO/CdS structure XPS survey spectrum, (b) Cd 3d, and (c) O 2p.

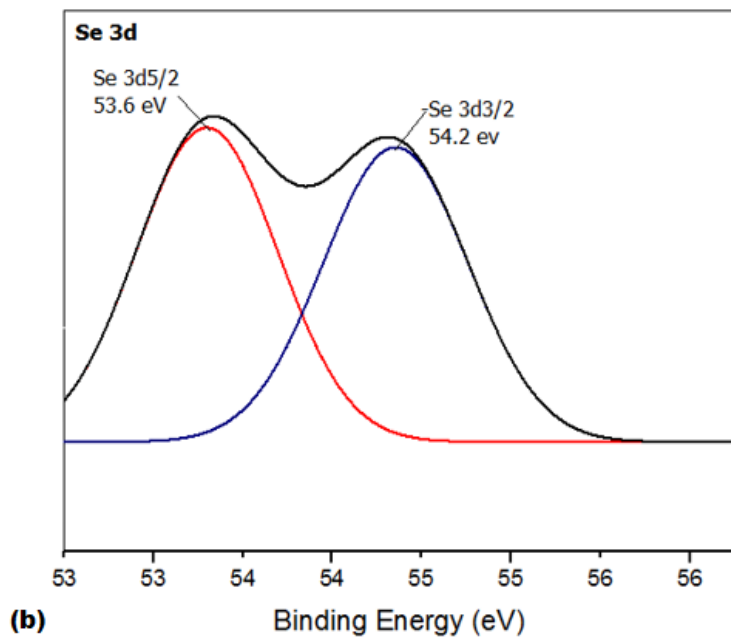
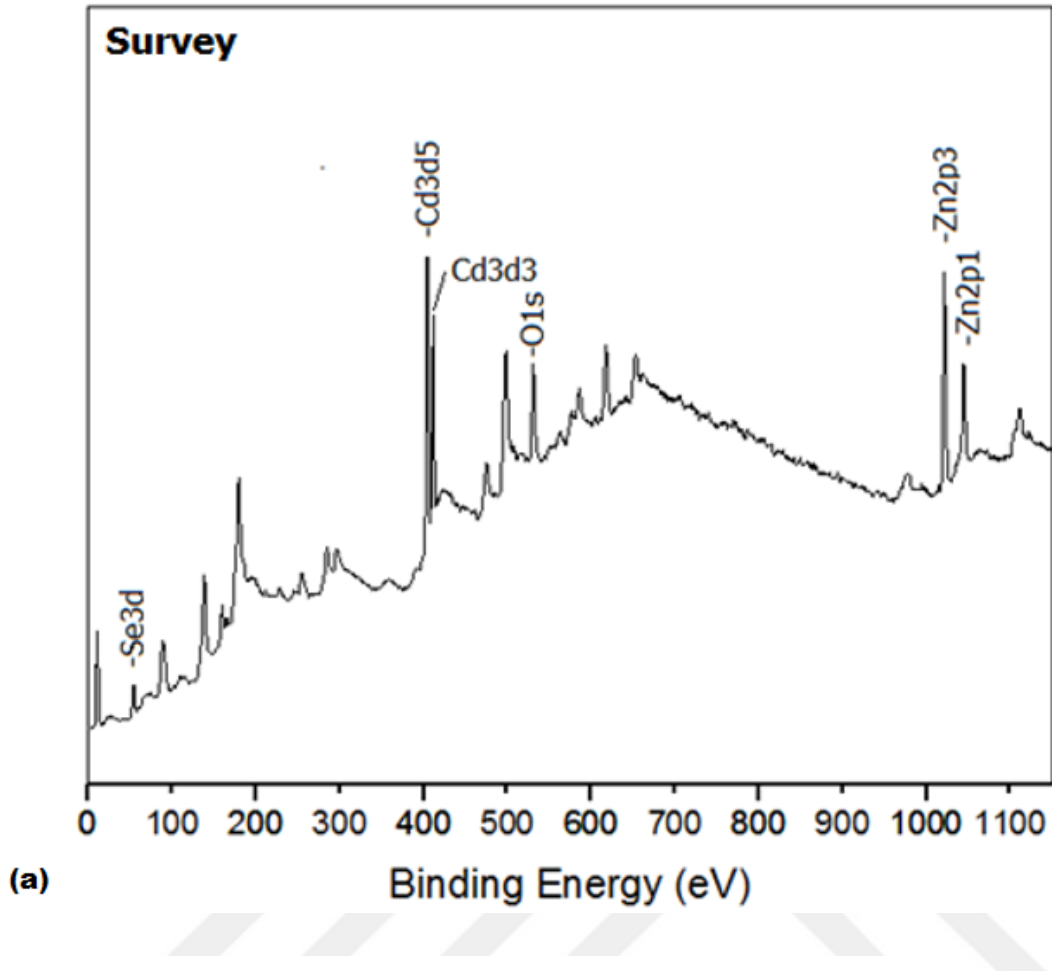


Figure 2.14 (a) the ZnO/CdSe structure XPS survey spectrum, (b) Se 3d.



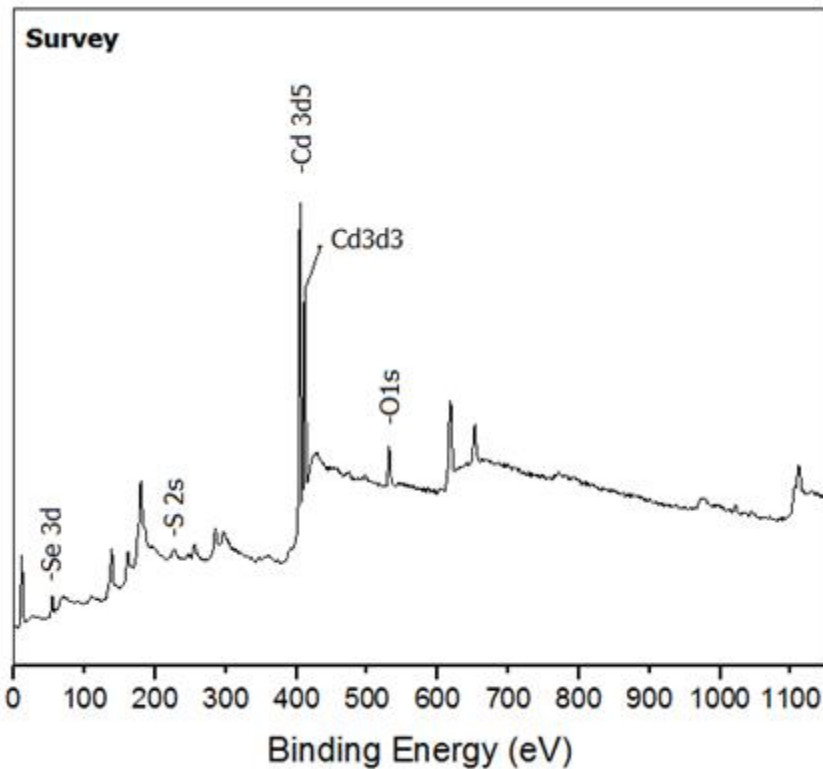


Figure 2.15 The ZnO/CdS/CdSe structure XPS survey spectrum.

Since each material has a set of especial d-spacing, they can be identified via conversion of the diffraction peaks to d-spacings. This can be attained by comparing the d-spacings with respect to standard reference patterns. Figure 2.16 depicts the XRD patterns of all untreated fabricated structures. The diffraction peaks at  $62.8^\circ$ ,  $47.5^\circ$ ,  $36.2^\circ$ , and  $34.4^\circ$  are related to (103), (102), (101) and (002) planes in the ZnO with hexagonal wurtzite crystalline structure, respectively (JCPDS: 36-1451). By fabrication of CdS layer, new diffraction peaks have been appeared at  $52.2^\circ$ ,  $43.7^\circ$ ,  $28.2^\circ$ ,  $26.5^\circ$ , and  $24.8^\circ$ , which are corresponded to well-indexed (112), (110), (101), (002) hexagonal crystal planes of CdS structure, respectively (JCPDS: 41-1049). For CdSe, hexagonal phase (JCPDS: 65-3436,  $a = b = 4.30 \text{ \AA}$ ,  $c = 7.01 \text{ \AA}$ ) was finely detected, with  $25.2^\circ$ ,  $26.5^\circ$ , and  $42.5^\circ$  which are corresponded to well-indexed (100), (002), and (110) crystal planes, respectively. Furthermore, there are no other impurity pattern peaks, consequently, it is confirming that the structures were obtained with high purity.

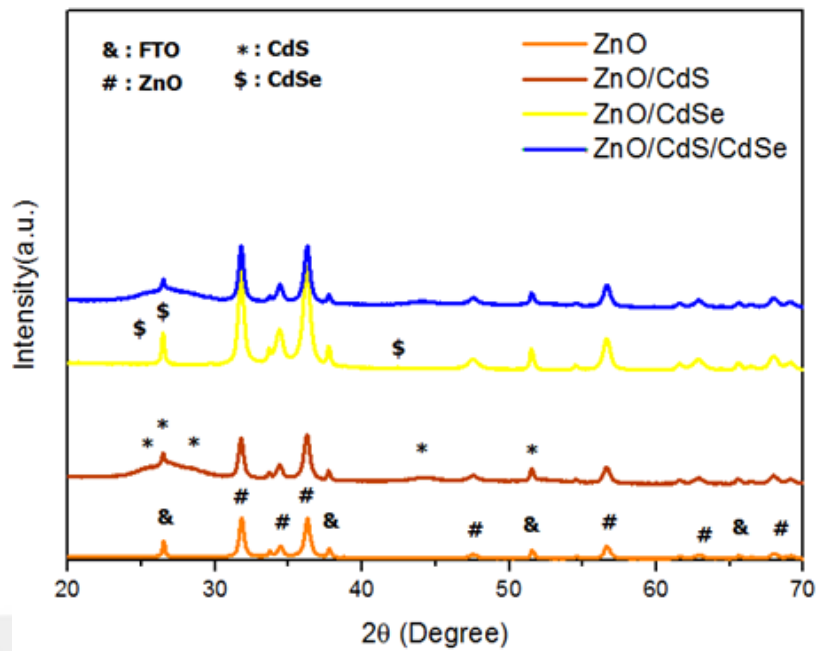


Figure 2.16 The XRD patterns of structures.

## 2.10. Scanning Electron Microscopy (SEM) and Transmission Electron Microscopy (TEM)

The transmission electron microscopy (TEM) and scanning electron microscopy (SEM) images represent the microstructure and morphology of the fabricated structures. Figure 2.17 and 2.18 represent ZnO structures fabricated in this research with urchins and flower-like morphology with diameters of about 30  $\mu\text{m}$  and 40  $\mu\text{m}$ , respectively. These morphologies of ZnO structures could provide a more efficient light absorption surface area instead of ZnO bulk materials. Figure 2.19-21 displays the magnified images after the deposition of CdSe, CdS, and CdS/CdSe layers, respectively. The Figure 2.22 represents the ZnO/CsPbBr<sub>3</sub>, the same as other SEM images CsPbBr<sub>3</sub> thin layer is deposited on ZnO structures. Figures 2.23-25 are the corresponding TEM images of the structures which further confirm the nanocrystalline construction of the synthesized substrates. As depicted in Figure 2.23 the ZnO nanostructures have size of about 30 nm. The Figure 2.24 exhibits the ZnO/CdSe crystal structures which are deposited on ZnO structure. Figures 2.24 c and d clearly depict the CdSe layer on ZnO. Finally, the CdSe nanostructures depicted in Figures 2.24 e and f which have been attached to ZnO nanostructure with size of about 10 nm. The interface is continuous, which can favor the transfer of charge carriers. The TEM of ZnO/CdS depicted in figure 2.25 clearly. The deposition of about 5 nm layer of CdS has been represented clearly.

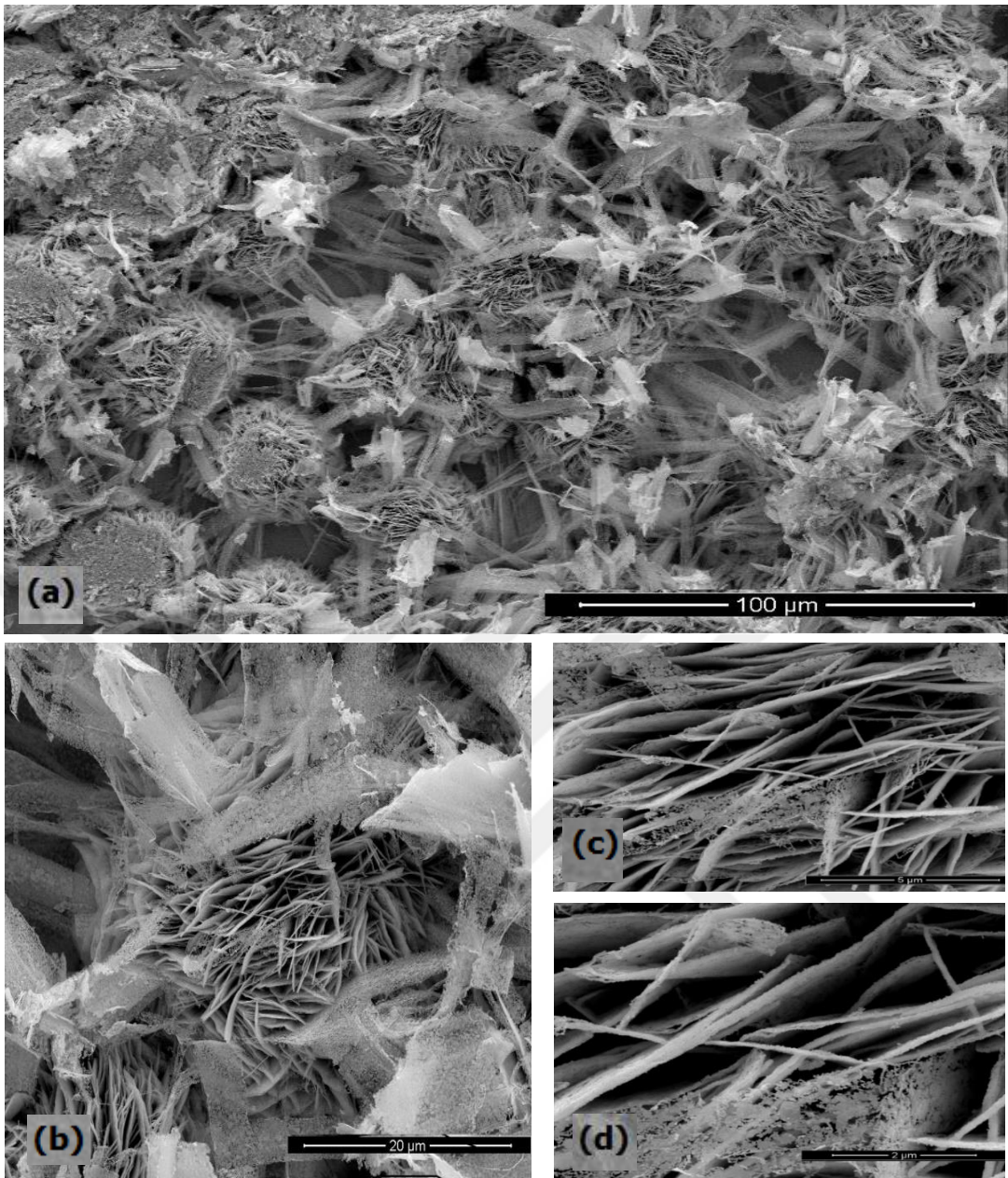


Figure 2.17 The SEM images of ZnO nanostructures with scale bars of (a) 100 μm, (b) 20 μm, (c) 5 μm, and (d) 2 μm.

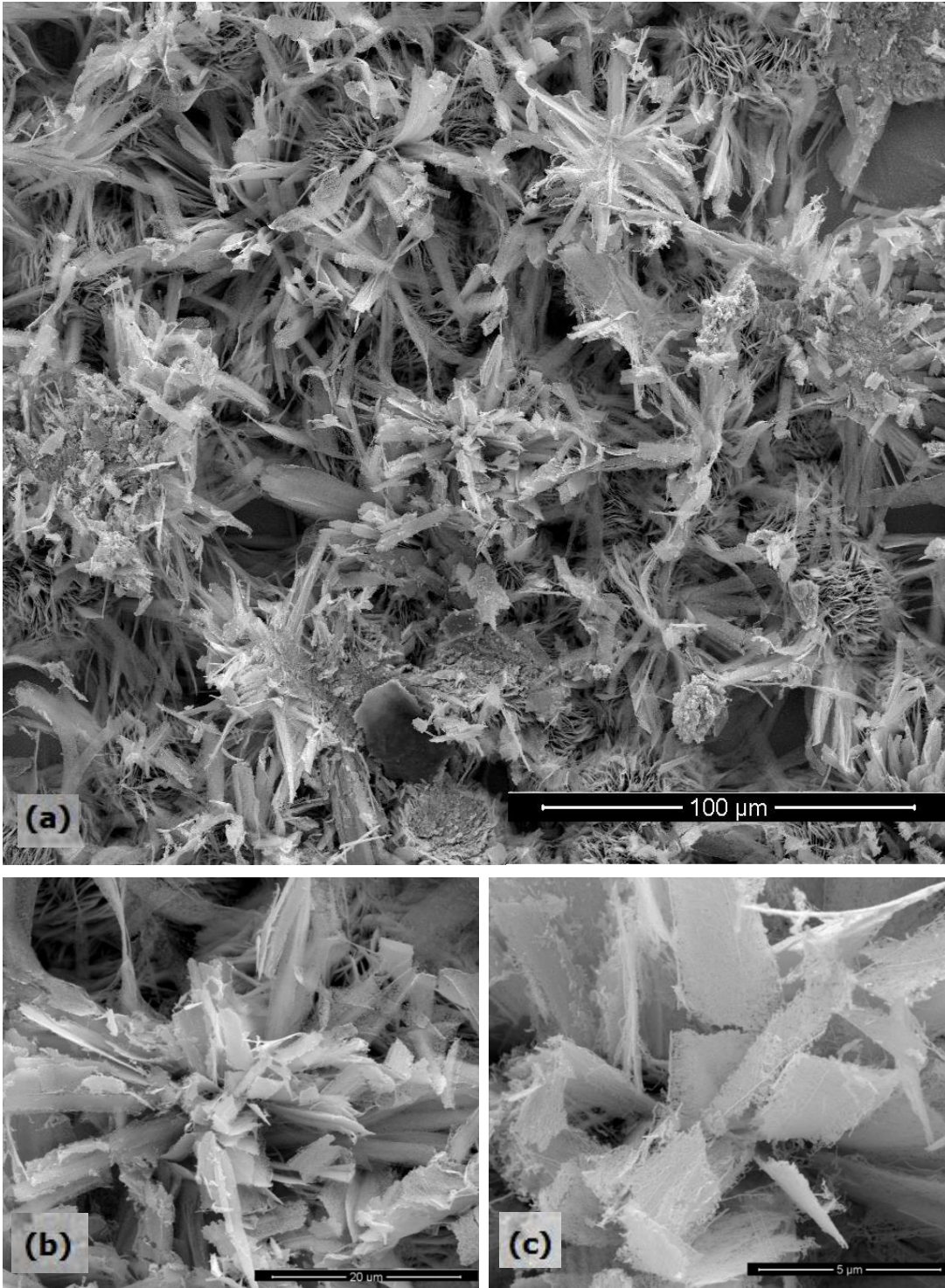


Figure 2.18 The nanostructured ZnO under SEM with scale bars of (a) 100 μm, (b) 20 μm, (c) 5 μm.

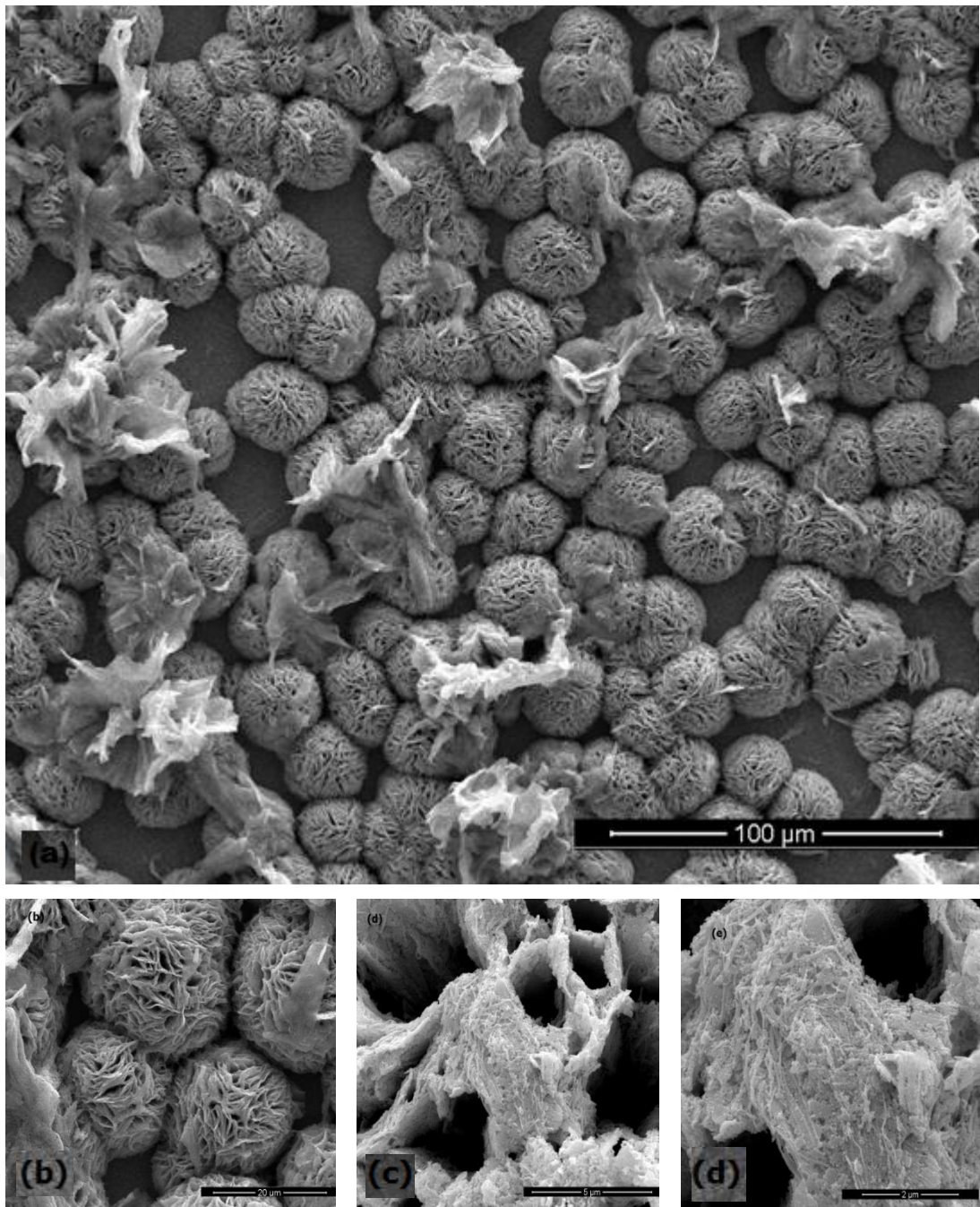


Figure 2.19 The SEM images of ZnO/CdSe nanostructures with scale bars of (a)100 μm, (b)20 μm, (c)5 μm, and (d) 2 μm.

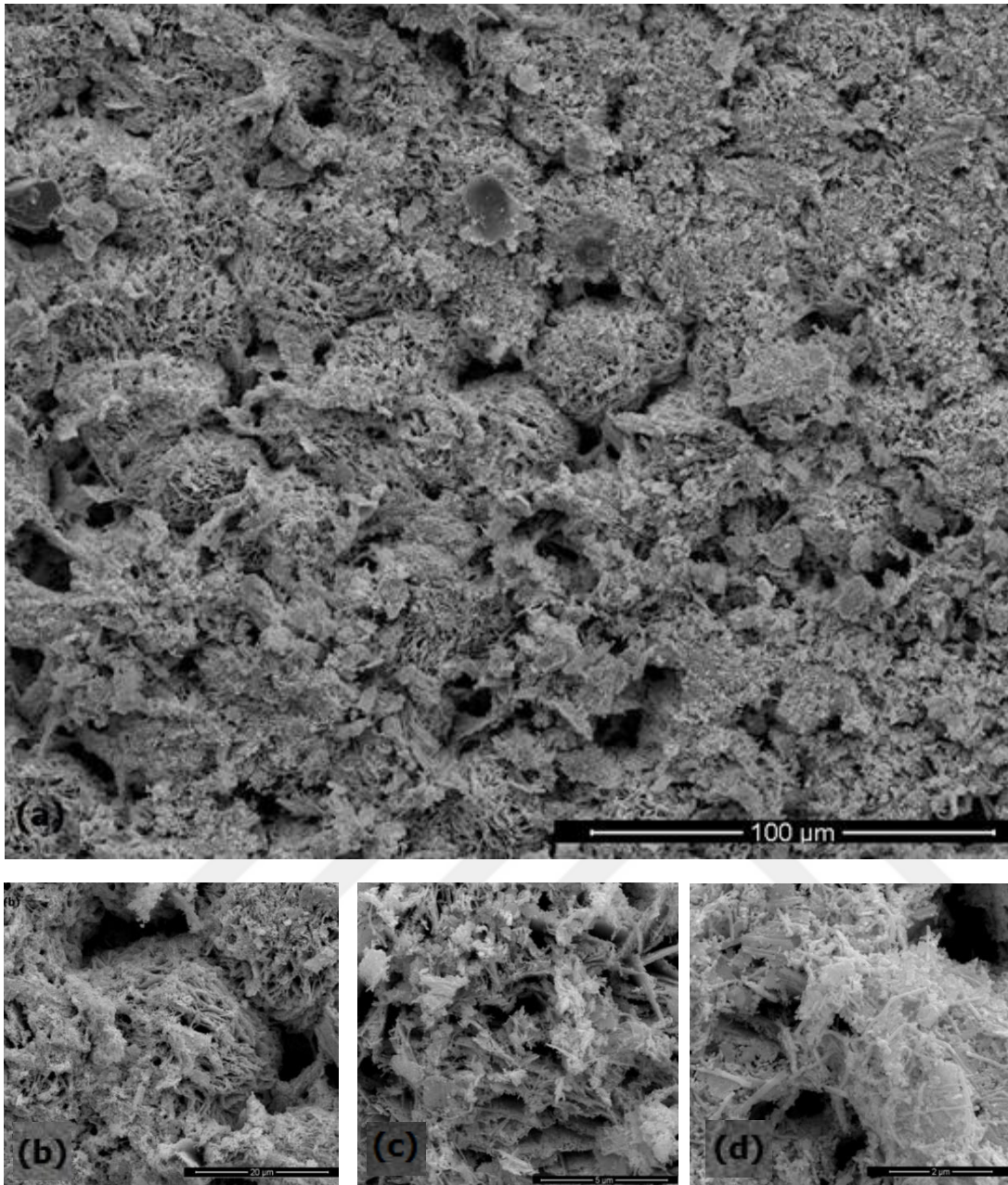


Figure 2.20 The SEM images of ZnO/CdS nanostructures with scale bars of (a)100 μm, (b)20 μm, (c)5 μm, and (d) 2 μm.

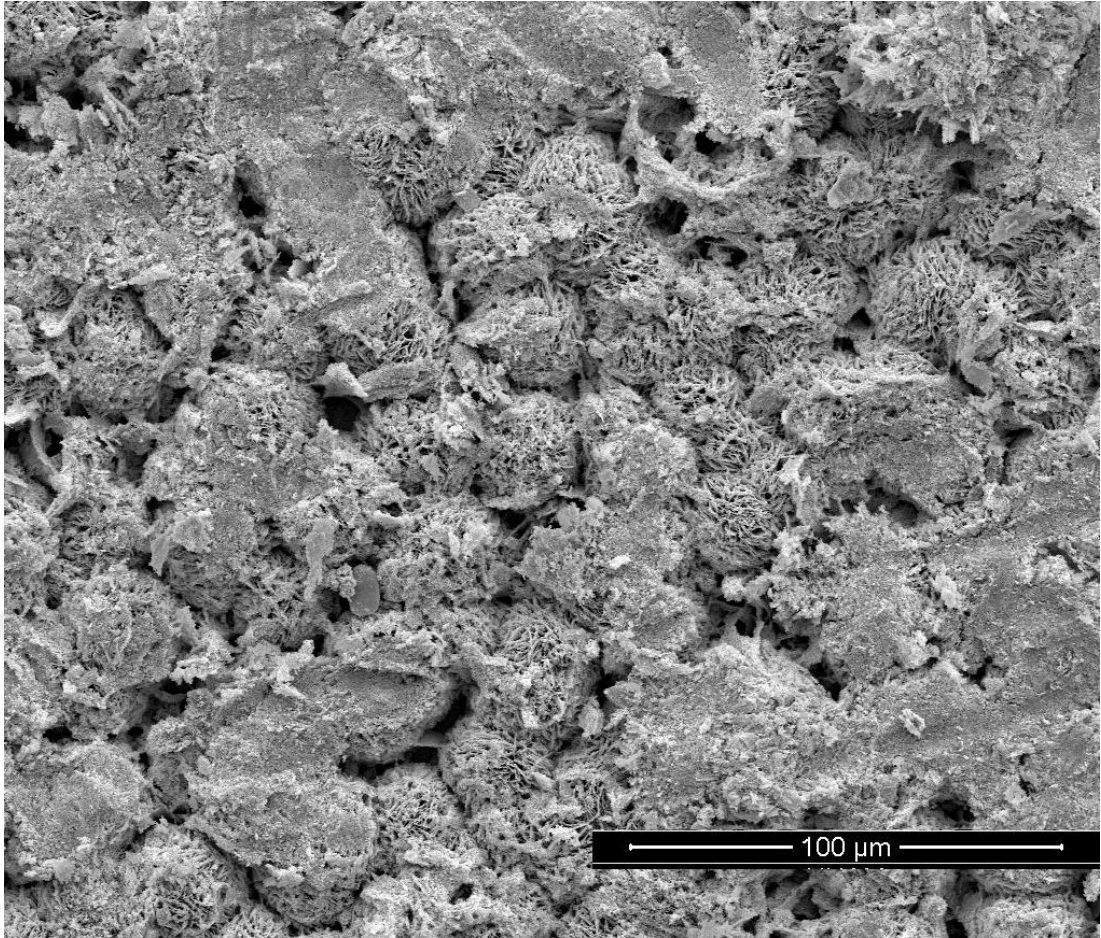


Figure 2.21 The SEM images of ZnO/CdS/CdSe nanostructures with scale bars of 100 μm.

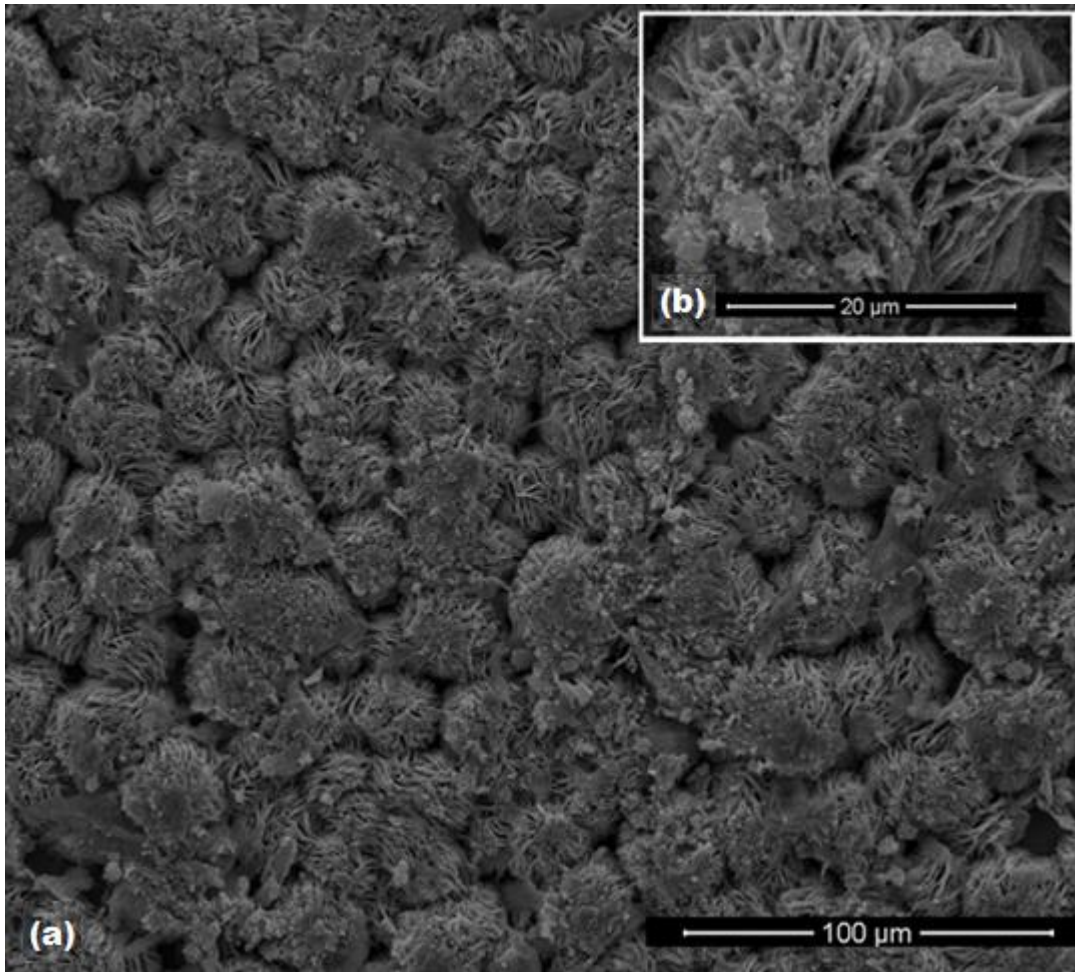


Figure 2.22 The SEM images of ZnO/CsPbBr<sub>3</sub> nanostructures with scale bars of (a) 100 μm, and (b) 20 μm.



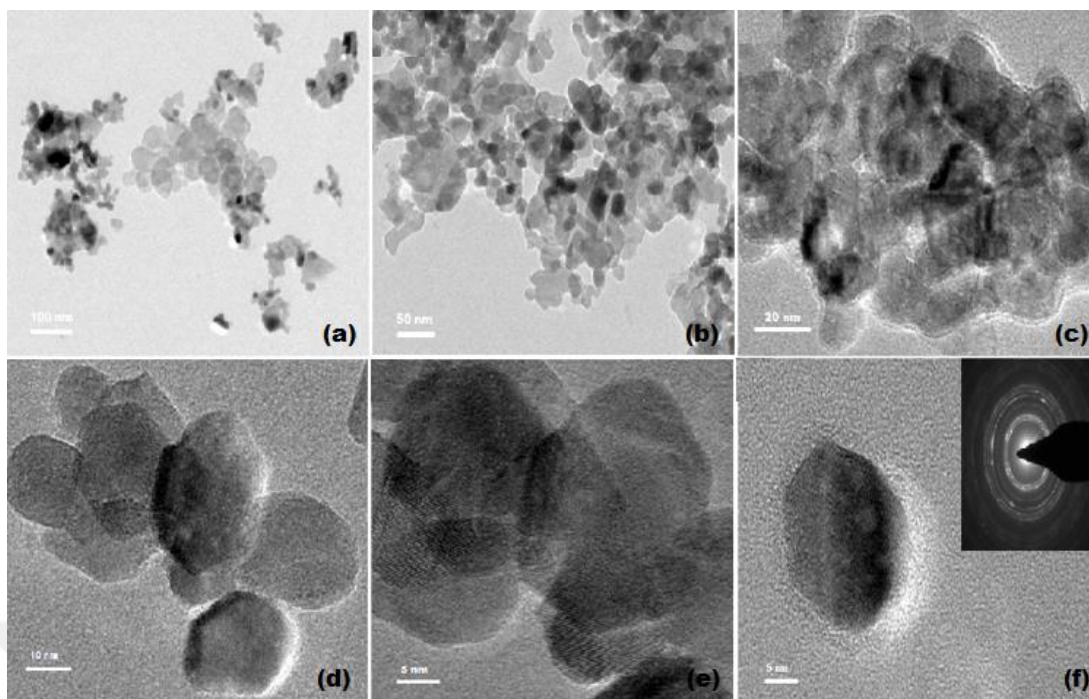


Figure 2.23 The TEM images of ZnO structures with scale bar of (a) 100 nm, (b) 50 nm, (c) 20 nm, (d) 10 nm, (e) 5 nm, and (f) 5 nm.

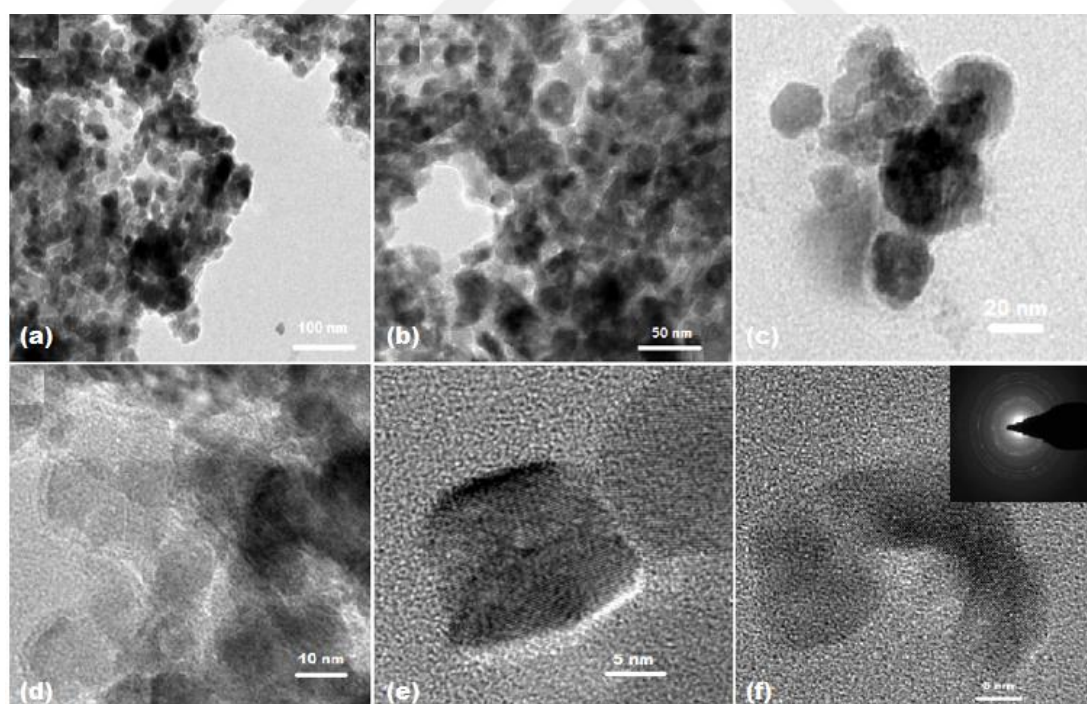


Figure 2.24 The TEM images of ZnO/CdSe structures with scale bar of (a) 100 nm, (b) 50 nm, (c) 20 nm, (d) 10 nm, (e) 5 nm, and (f) 5 nm.

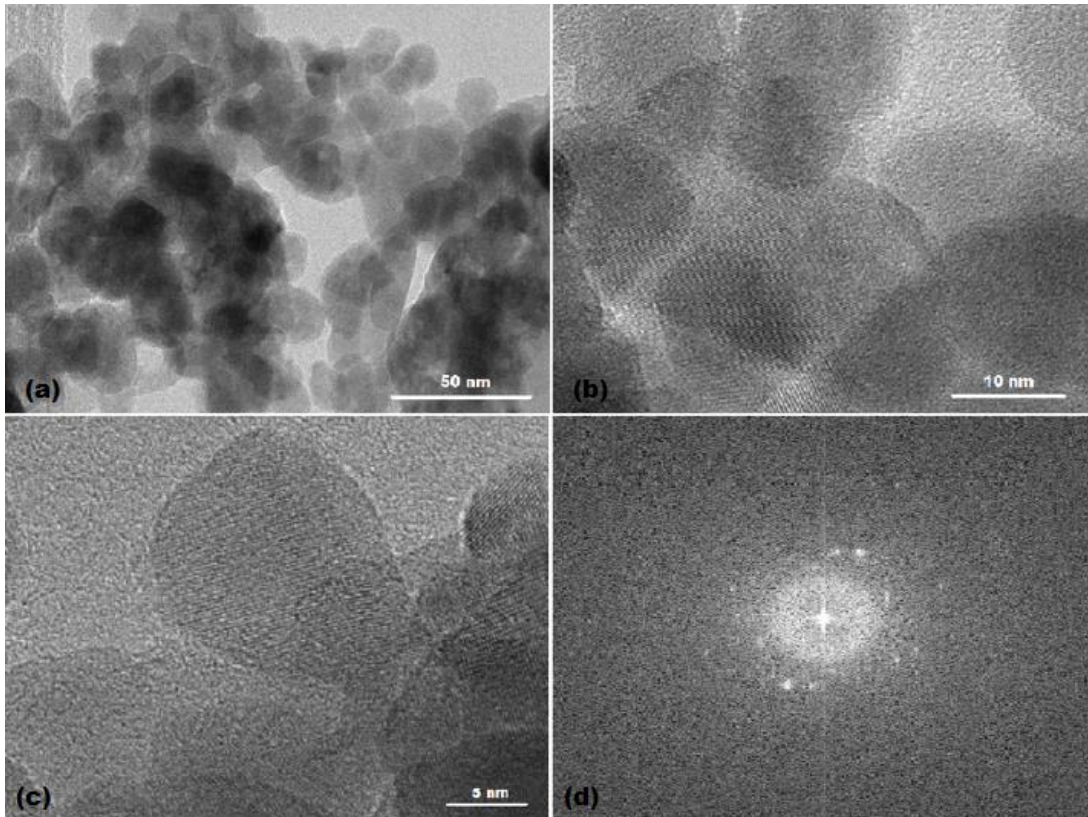


Figure 2.25 The TEM images of ZnO/CdS structures with scale bar of (a)50 nm, (b)10 nm, (c)5 nm.

### 3. RESULTS AND DISCUSSIONS

#### 3.1. Photoelectrochemical Device

The photoelectrochemical (PEC) water splitting device can be performed by using a double- or single cell equipped with a small optical window. It is including several parts of electrodes. Three- or two-electrode compartment device are used to analyze the performance of the working electrode as a half cell and the performance of a whole cell. In a two-electrode device, the dark- and photo-current are recorded with respect to voltage against a counter electrode. The potential of counter electrode has the same as quantity as potential of the redox reaction happening on the counter electrode. However, the potential of the redox reaction is not at equilibrium with the counter electrode due to the reaction over-potential, which strongly depends upon the current density.

Therefore, the current-voltage curve depends on the characterization of the counter electrode. As a result, the working electrode potential cannot be analyzed in the two-electrode system. The aim of the two-electrode system is to distinguish the performance of the PEC cell by considering the over-potential loss in counter and working electrodes. But, in the three-electrode device, a potential-static as a function of the reference electrode can control the potential of the working electrode. The dark- and photo-current are recorded with respect to the potential as a function of the electrolyte solution. The aim of the three-electrode device is to explain working electrode potential with respect to the electrolyte solution, which is not depend upon the characterization of the counter electrode. The mercury/mercury oxide, the silver/silver chloride, and the saturated calomel electrodes are the most commonly used reference electrodes in the PEC water splitting process. They can depict the certain potential as a function of the electrolyte solutions with distinguished redox temperature, concentration, and species. The working electrode potential can be measured as a function of a reference electrode. And it can be converted to the potential vs. the reversible hydrogen electrode (RHE) on the following equation:

$$E_{RHE} = E_{ref} + E^0_{ref} + \frac{RT \ln 10}{F} PH \quad (3.1)$$

where  $E_{ref}^0$ ,  $E_{ref}$ , and  $E_{RHE}$ , defined as the reference electrode potential as a function of the normal hydrogen electrode (NHE), the working electrode potential can be measured as a function of a reference electrode (if the potential is independent of PH), and the working electrode potential against the electrolyte solution with respect to the RHE, respectively. The F, R, and T stand for Faraday constant, gas constant, and temperature, respectively. The potentials at +1.23 and 0 vs. RHE shows the potential where oxygen and hydrogen are in equilibrium with the electrolyte solution. There are different types of light sources using for illumination, such as light-emitting diodes, halogen lamps, Xe lamps, and Hg lamps. Halogen and Xe lamps mostly fabricate continuous spectra, while light-emitting diodes and Hg lamps excel in fabricating emission line spectra. Solar simulator can be formed by a suitable filter using Xe lamps. The power spectra should be considered as an intense at a different wavelength of visible light source at different distance, and position since the energy and photon fluxes are significant in the assessment of the energy conversion and the quantum efficiencies. Since the splitting rate of the water strongly depends upon the reaction temperature, the solution should be avoided from heating under illumination. In addition, oscillations in vapor pressure can produce gas phase which affect the reaction and reactor condition.

### 3.2. PEC Efficiency

The solar-to-hydrogen efficiency (STH) can be measured from the product of the gain in Gibbs energy ( $\Delta G$ ) and the rate of hydrogen production ( $r_{H2}$ ).

$$STH = \frac{\text{Output Energy as H}_2}{\text{Energy of incident solar light}} = \frac{r_{H2} * \Delta G}{P_{sun} * S} \quad (3.2)$$

Where S is the area of the reactor and P<sub>sun</sub> is the sunlight energy flux. The irradiation solar energy flux is 1000 W.m<sup>-2</sup> which is AM1.5 global tilt, with well-defined power spectrum. When an external voltage is applied to PEC devices, the electrical energy should be subtracted from the energy gain. For the two-electrode calculations, the applied bias photon-to-current-efficiency (ABPE) is used and is defined as:

$$ABPE = \frac{|J| * (V_{th} - V_{bias})}{P_{sun}} \quad (3.3)$$

Where  $V_{bias}$ ,  $V_{th}$ , and  $J$  are applied voltage, the water-electrode voltage (1.23 V), the photocurrent density, respectively. A problem related to ABPE is that the faradaic performance is not explicit. Therefore, the photocurrent is not necessarily related to splitting of water unless the generation of oxygen and hydrogen are confirmed at the faradaic performance. The faradaic performance of the water splitting is defined as the ratio of the present current in water splitting into oxygen and hydrogen to get the current. In reality, four electrons are corresponded to one oxygen molecule and two hydrogen molecules. If the faradaic performance is below unity, a part of the current must be contributed other than water splitting to redox processes. By considering the naming and ambiguous definition of ABPE either as quantum efficiency or energy conversion efficiency, it has been suggested that applied-bias can be compensated the solar-to-hydrogen efficiency (AB-STH) as a general expression of STH via PEC water splitting under sunlight irradiance:

$$AB - STH = \frac{|j| * \eta_F * (V_{th} - V_{bias})}{P_{sun}} \quad (3.4)$$

In equation 3.4,  $V_{bias}$  and  $\eta_F$  are zero and unity respectively, which STH is corresponded to a special case of AB-STH.

It should be noted that due to the discharging/charging of co-catalysts, the surface of photoelectrodes, and trap states, the current-voltage curves often have an important hysteresis in cyclic voltammetry. To get a precise estimate of AB-STH, the photocurrent at a static applied voltage should be measured and a two-electrode device also should be used. Obviously, to quantify the amounts of oxygen and hydrogen gases since  $\eta_F$  should be known. When side reactions are hydrogen and oxygen gases, the PEC cell should be purged with inert gas such as Ar.

The quantum efficiency with respect to wavelength is a special suitable parameter to identify the limiting performance factors in PEC system photoelectrodes.

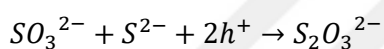
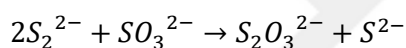
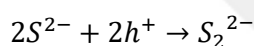
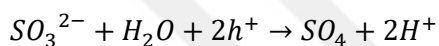
The definition of the external quantum efficiency or incident photon-to-current conversion efficiency (IPCE) is the fraction of the incident photons that are converted to electrons, which is given by equation

$$IPCE = \frac{1240 * I_{ph}}{\lambda * P_{light}} \quad (3.5)$$

1240 is the unit correction factor,  $P_{light}$  is the photon flux ( $W/m^2$ ),  $\lambda$  is the incident light wavelength (nm), and  $I_{ph}$  is the generated photocurrent density ( $A/m^2$ ).

### 3.3. Findings

Current densities of the produced photoelectrodes under applied voltage are examined. Nanostructured ZnO and cadmium chalcogenides photoelectrodes give different results to the applied light intensity. Figure 3.1 depicts the obtained results related to ZnO, ZnO/CdS, ZnO/CdSe, ZnO/CdS/CdSe, and ZnO/CsPbBr<sub>3</sub>. Different Heterojunction structures depicted different current density values. An important condition observed during measurements is current density-voltage measurements under the current conditions and the dark conditions. In this case, dark current may be caused by external voltage in the electrolyte solution and some side reactions. The following side reactions in sulfate and sulfur are likely to occur:



As seen in figure 3.1, the intensity of the current under the light and dark are different. It was observed that the voltage varies according to the applied value. High values belong to ZnO/CdS, ZnO/CdS/CdSe, ZnO/CdSe, and ZnO/CsPbBr<sub>3</sub>, respectively. In addition, as depicted in fig 3.1 (e), the dark condition value of the ZnO/CsPbBr<sub>3</sub> structure also is high due to side reaction effects in solution. It can be interpreted that due to a more disintegration reaction of water, the electron-hole pair generation is also increasing under illumination for mentioned structures respectively.

$$ABPE (\%) = \frac{(J_{Ill} - J_{Dark}) * (1.23 - |E_{RHE}|)}{P_{in}} * 100 \quad (3.6)$$

In this formula, the term  $(J_{Ill} - J_{Dark})$  represents the current intensity difference between darkness illumination conditions,  $E_{RHE}$  represents the voltage applied during measurement according to the standard hydrogen electrode (SHE), and  $P_{in}$  represents the power of light. Ag / AgCl reference electrode was used for measurements. For this reason, the voltage applied to the reference electrode (Ag / AgCl) is converted to the SHE.

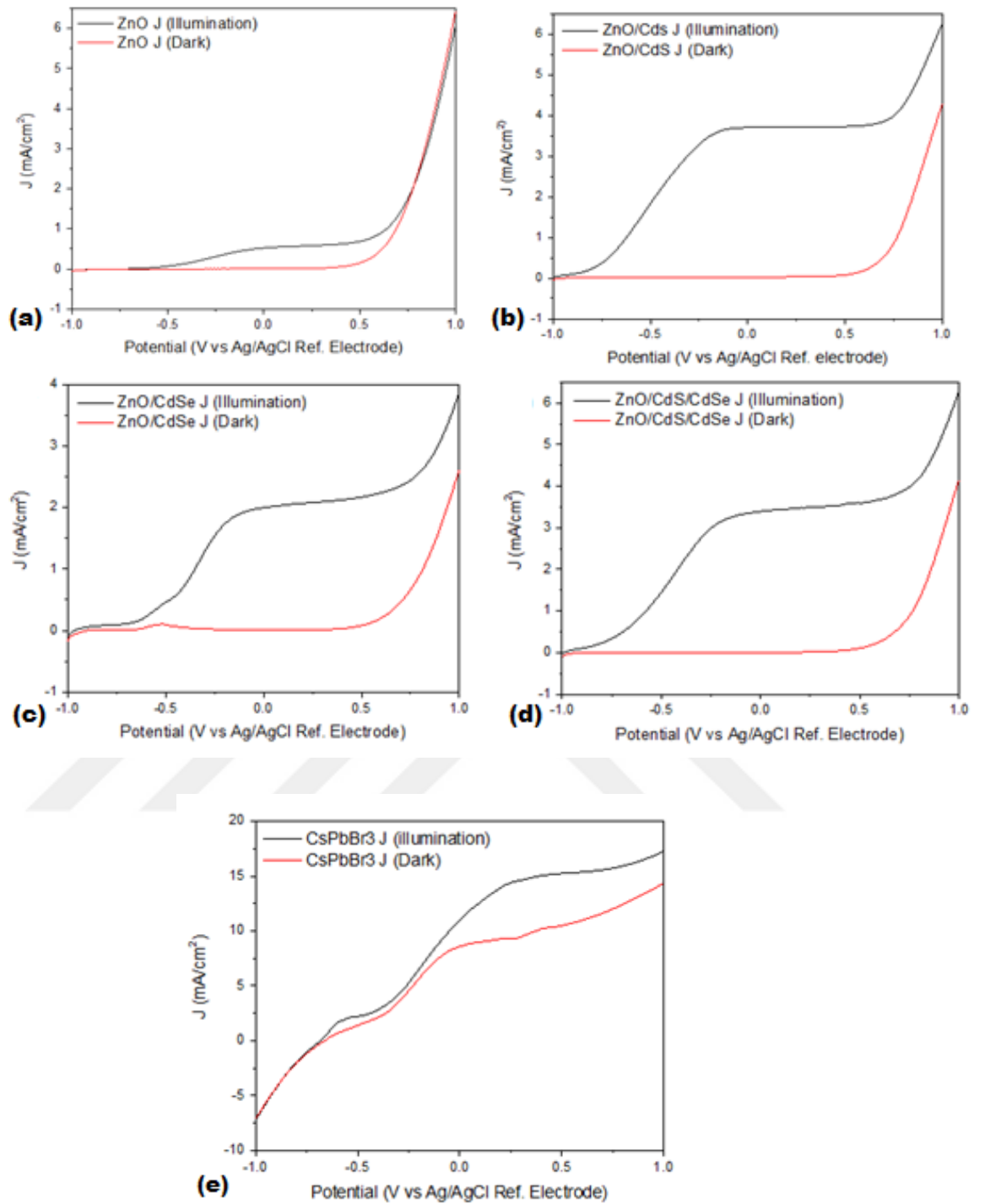


Figure 3.1 The J-V curves of photoanode structures.

Conversion formula from 3.1:

$$E_{ERH} = V_{Ag/AgCl} + 0.59 * PH + E_{Ag/AgCl}^0 \quad (3.7)$$

Figure 3.2 depicts the voltage-dependent conversion efficiency or ABPE efficiency of the films. The obtained yields were calculated by the differences in luminous current densities and luminous dark current densities of photoelectrodes. The formula used for the yields given below:

In this formula,  $V_{Ag/AgCl}$  represents the voltage applied according to Ag / AgCl reference electrode and  $E_{Ag/AgCl}^0$  represent the voltage difference of the reference electrode compared to SHE. 0.05 molar  $Na_2S$  and 0.95 molar  $Na_2SO_3$  pH values used during the measurements were determined as 12.5. The voltage values applied according to Ag/AgCl were calculated according to the SHE and used in the conversion efficiency given in Figure 3.2.

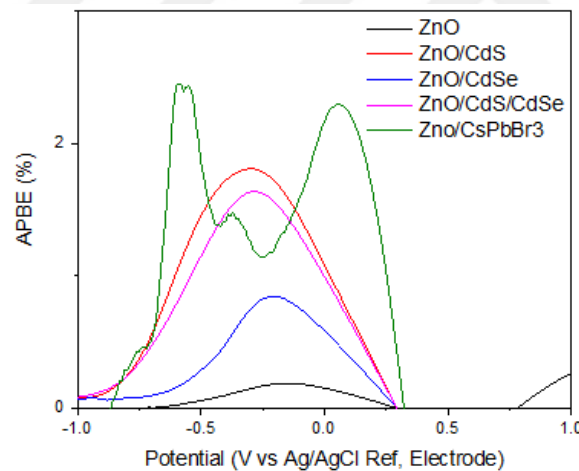


Figure 3.2 The APBE performance of untreated structures.

The performances of different structures have been depicted in figure 3.2, and illumination current density was obtained from photoelectrodes. The  $ZnO/CsPbBr_3$  and  $ZnO/CdS$  structures gave the highest efficiency values. Because for both structures the light absorption occurs in visible region which is the same as the solar spectrum. Figure 3.3 shows the graph of stabilization measurements performed in the 3-electrode configuration and with the same electrolyte solution. In this study, measurements were taken at 0V according to Ag / AgCl reference electrode. At about 7200 s, the current density dropped slightly and then remained



stable. The initial decrease is thought to be due to the accumulation of oxygen gas on the surface and slowing down the reaction kinetics resulting from rapid reactions at the semiconductor/electrolyte interface. After 4000 seconds, it was observed that these kinetics reached a certain equilibrium for all samples.

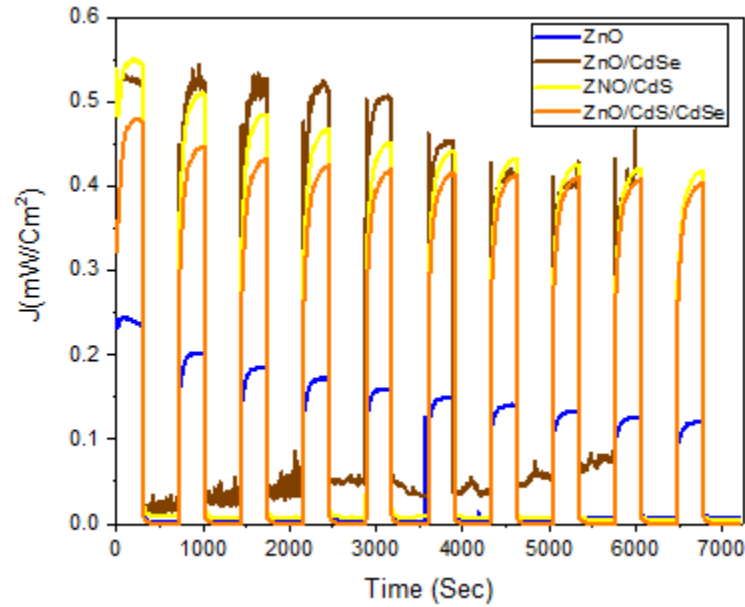


Figure 3.3 The stability of the photoanode structures.

In the end, ZnO/CdS/CdSe was the most damaged structure and after 6000 S the current density becomes minimum. In order to understand the strength of the photoelectrode and the change in the measurement time, measurements were carried out consecutively between -1.1 volts under light and dark, respectively.

#### 3.4. IPCE Results

Figure 3.5 represents the wavelength dependence IPCE action spectrum using formula 3.5 at different monochromatic light wavelengths at 0 V vs Ag/AgCl. IPCE is a significant factor to investigate the PEC activity of photoelectrodes. For the ZnO structure, there is no absorption in the visible region. But, other photoanode structures had important enhance IPCE values with respect to the ZnO structure in the visible light wavelength range from 350 nm to 700 nm. These promotions in the IPCE percentage results from an improved light harvesting ability by CdSe, CdS, and CsPbBr<sub>3</sub>. After loading cadmium chalcogenides on ZnO a broadened IPCE profiles were developed over the visible light wavelength region from 350 nm to 650 nm. The highest IPCE percentage efficiency of the ZnO/CdS photoanode was about 50% at

500 nm, approximately 1.7 times higher than that of ZnO/CdS/CdSe. The enhanced IPCE of the ZnO/CdS structure to ZnO/CdS/CdSe is mainly related to the multi-heterojunctions and thickness of ZnO/CdS/CdSe structure as the visible light absorptions are obviously decreased compared to ZnO/CdS.

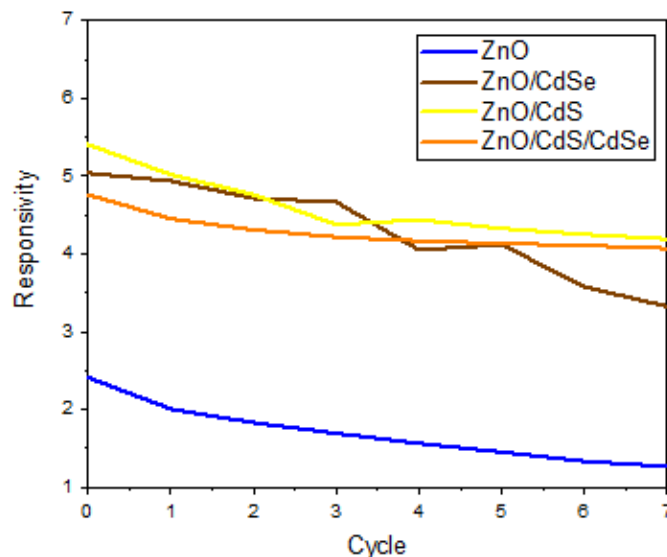


Figure 3.4 The responsivity of the structures.

### 3.5. Results for Heat Treatment Cadmium Chalcogenide Structures

In this section, the heat-treated structures were analyzed and the results represented enhancements in ABPE efficiency and IPCE for ZnO/CdSe and ZnO/CdS/CdSe photoanodes. The reason for the mentioned improvement will be discussed in the x-ray diffraction and crystalline structure discussion section. As depicted in figure 3.6 and 3.7, illumination current density of heat-treated ZnO/CdSe photoanode was increased from 2 ( $\text{mA}/\text{cm}^2$ ) to 3 ( $\text{mA}/\text{cm}^2$ ) and for ZnO/CdS/CdSe photoanode from 3.5 ( $\text{mA}/\text{cm}^2$ ) to 4 ( $\text{mA}/\text{cm}^2$ ). In addition to illumination current density, ABPE efficiency and IPCE also were increased perfectly. As depicted in figure 3.8, ABPE percentage increased from 1% at -0.25 V to 2% at -0.5 V for ZnO/CdSe photoanode, and for multi-junctional ZnO/CdS/CdSe photoanode, it increased considerably from about 1.5 % at -0.25 V to about 5.5% at about 0.5 V. The IPCE also increased dramatically from 25% at 500 nm to 60% at 550 nm and 10% to 55% at 650 nm for ZnO/CdSe, and for multi-junctional structure it rose from 30% at 500nm to about 48% and from 15% to 48% at 550 nm. The increases represent high quality for photoanode structures. For 200°C treated ZnO/CdSe structure, XRD patterns were depicted and compared with the untreated structure in figure 3.11. As can be seen clearly, the crystalline structure of the ZnO/CdSe structure was remarkably promoted. And the intensity of ZnO phase patterns also was decreased.

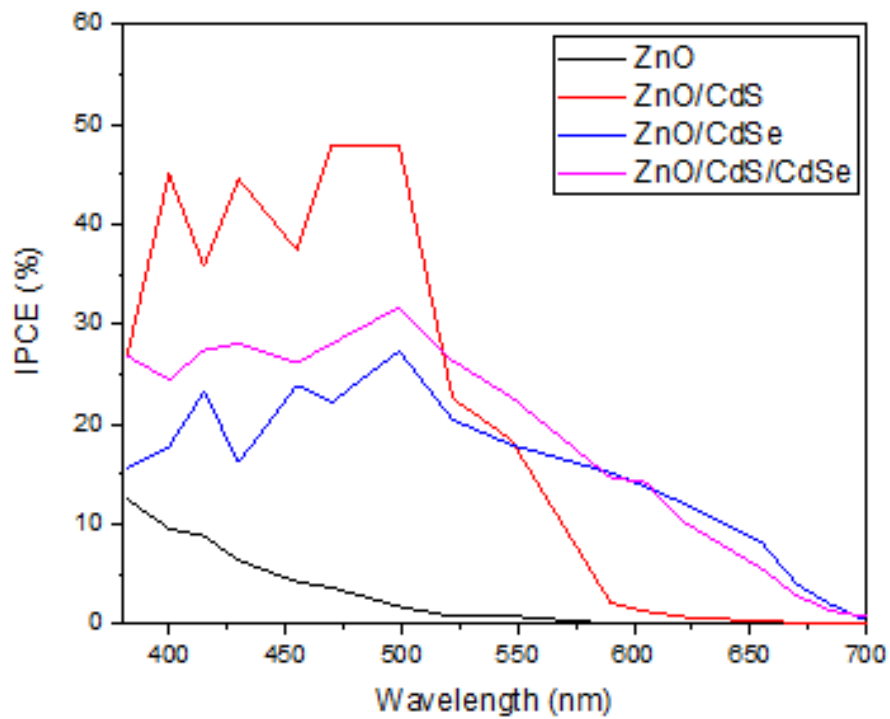


Figure 3.5 The IPCE of untreated structures.

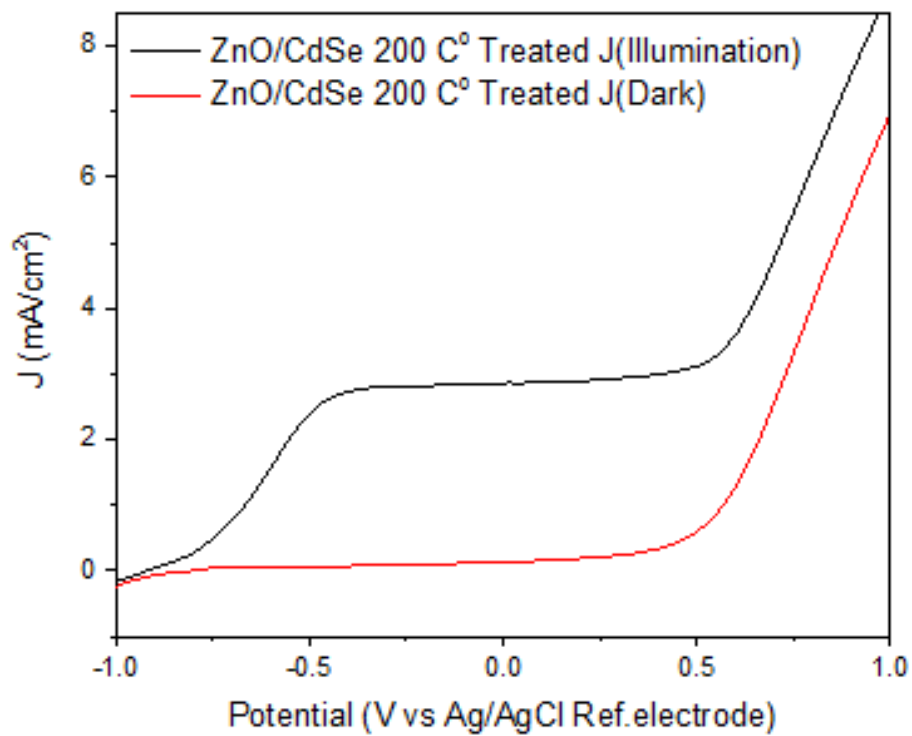


Figure 3.6 The J-V curve of the treated ZnO/CdSe structure.

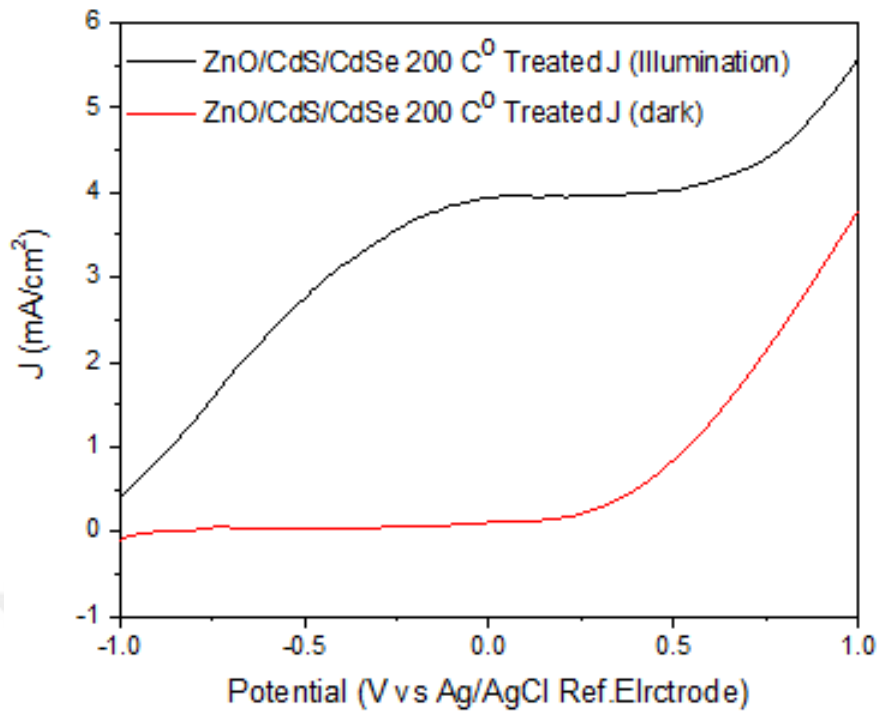


Figure 3.7 The J-V curve of the treated ZnO/CdS/CdSe structure.

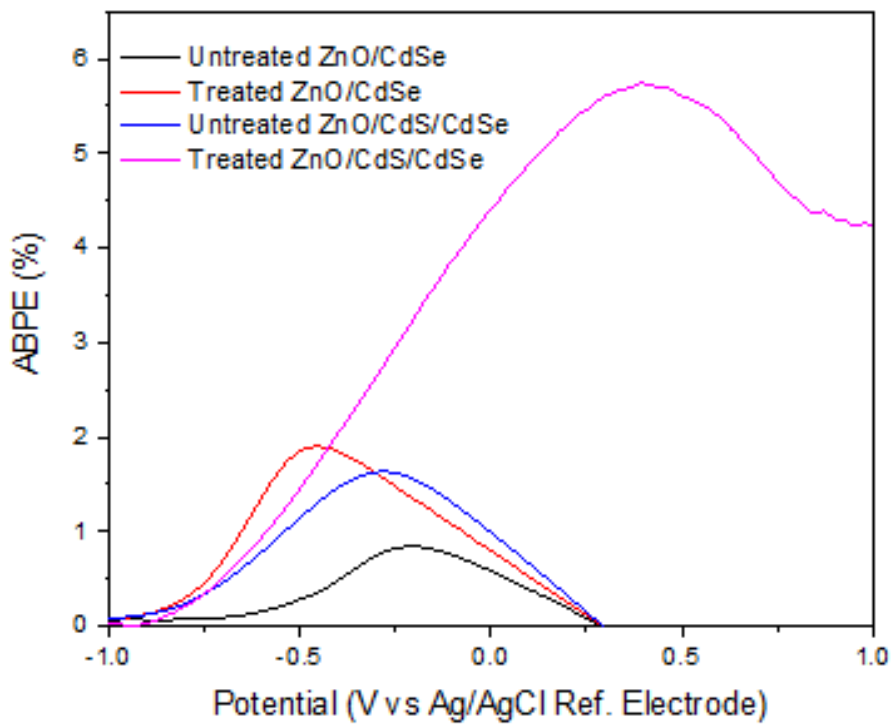


Figure 3.8 The APBE performances of treated structures.

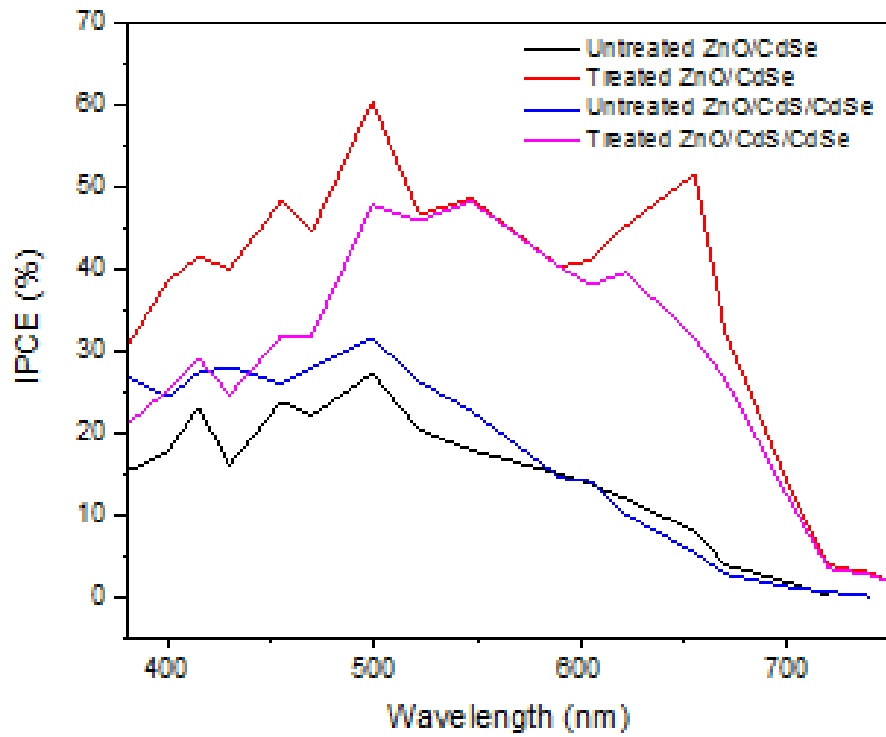


Figure 3.9 The IPCE of the treated structures.

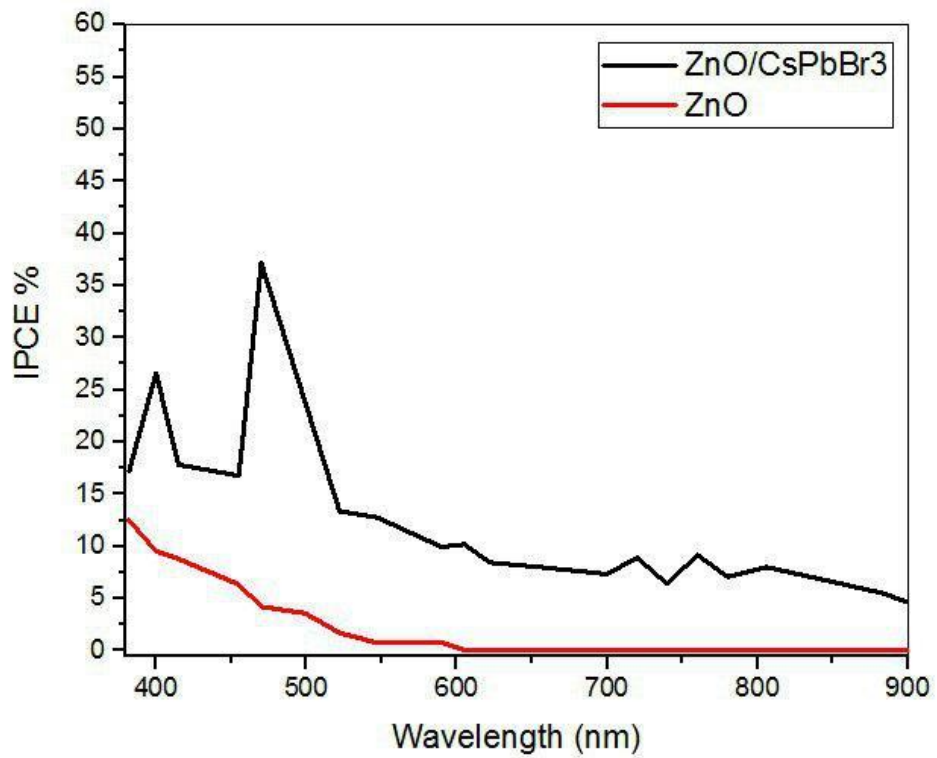


Figure 3.10 The IPCE of the ZnO/CsPbBr<sub>3</sub> structure.

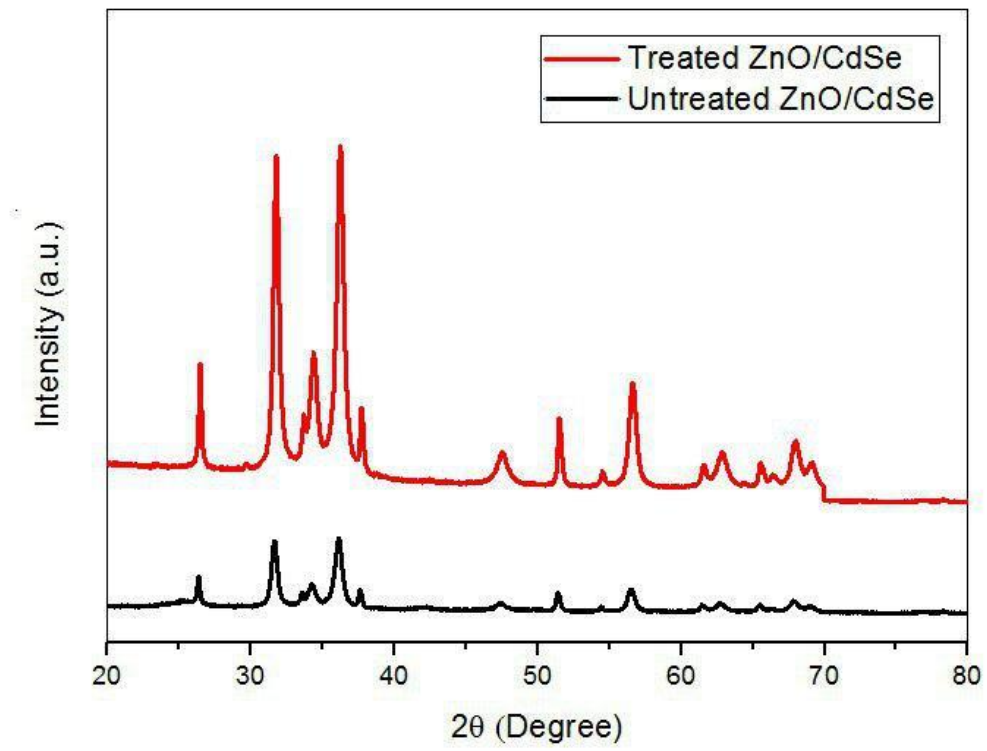


Figure 3.11 The XRD pattern of ZnO/CdSe for treated and untreated structures.

## 4. CONCLUSION

The purpose of this thesis was to study the synthesis and characterization of semiconductors including ZnO, CdS, CdSe, and CsPbBr<sub>3</sub>, then fabrication of photoelectrochemical water splitting device using the semiconductor with hetero-junction structures. Moreover, we have studied the effect of thermal annealing on semiconductors structure and device performance.

In chapter 1, we introduced general physical and chemical properties of ZnO, cadmium chalcogenides, and perovskites semiconductors including optical, catalytic, hydrophobicity, and field emission properties. Then we introduced the potential applications of the semiconductors in different fields including, electrochromic displays, field-effect transistors, sensors, optoelectronic and luminescence devices such as photovoltaics, light-emitting diodes, laser, photodetectors, and photoelectrochemical water splitting. Finally, we provided different synthesis and fabrication methods including chemical bath deposition, colloidal, high-temperature injection, microwave-assisted, sonication, spin coating, and hydrothermal.

In Chapter 2, we introduced spin coating and chemical bath deposition fabrication of thin film and their advantages and disadvantages. The chemical bath deposition is one of the best candidates for the synthesis of semiconductors since it is easy, economics, it can be used in lower temperatures. The spin coating is also simple for the coating of a wide variety of materials with the aim of coating of antireflection, flat screen and conductive oxide layers with controlling the thin film thickness. Then we explained the synthesis of ZnO and cadmium chalcogenides semiconductors with chemical bath deposition method and CsPbBr<sub>3</sub> with spin coating in detail. The hetero-structures ZnO/CdSe and ZnO/CdS/CdSe were thermally annealed at 200 ° C for 3 hours. The synthesized semiconductors were proven by the composition analyze of EDX and XPS. The UV-vis analysis depicted the absorbance of ZnO in the UV region and for hetero-structures in the visible region. The PL of the ZnO represented a strong recombination rate at the UV region, but by deposition of cadmium chalcogenides due to increasing separation of photoinduced charge, the recombination occurred at the visible region. For the ZnO/CsPbBr<sub>3</sub> structure, a very sharp PL peak depicted high quality and pure color emission. The crystalline structure of the samples was analyzed using XRD. Finally,

the nanostructure and urchin- and flower-like morphologies have been illustrated by TEM and SEM, respectively.

In chapter 3, to generate hydrogen gas, the photoelectrochemical water splitting device was set up with the fabricated hetero-structures photoanodes, electrolyte solution, cathode and reference electrode under AM1.5 global tilt of  $1000 \text{ W.m}^{-2}$  solar energy flux. The efficiency and IPCE of the system were measured for the synthesized structures. All structures were depicted in a perfect performance, but thermally annealed structures represented outstanding IPCE and efficiency in the visible region. The reason for high performance was crystalline improvement occurred during thermal annealing. The stability of the structures was also considerable.

The most important topic about using cadmium chalcogenides structures is the presence of cadmium heavy metal which is very toxic and it should be replaced by non-toxic materials including indium sulfide and zinc sulfide. Finally, by combining the synthesized n-type ZnO and cadmium chalcogenide structures with p-type and i-type semiconductors, p-n and p-i-n junction diode structures can be fabricated and used in light-emitting and photovoltaic devices.



## REFERENCES

- [1] Taesoo, D., Leea, A., Ebongb, U., (2016). A Review of Thin Film Solar Cell Technologies And Challenges, *Renewable and Sustainable Energy Reviews*, Volume 70, 1286 -1297.
- [2] Shah, A., Torres, P., Tschanner, R., Wyesch, N., Keppner, H., (1999). Photovoltaic Technology: The Case for Thin-Film solar cells, *Science*, Volume 285, 5428, 692-698.
- [3] Oesch, R., Faber, T., Von Hauff, E., Brown, T.M., Lira-Cantu, M., Hppe, H., (2015). procedures and Practices for Evaluating Thin-Film Solar Cell Stability, *Advanced Energy Materials*, Volume 5, 20, 1501407.
- [4] Chen, Z., Zhao, X., Tang, Y., (2019). Thin Films for Energy Harvesting, Conversion, and Storage, *Coating*, 174.
- [5] Xu, S., Wang, L.Z., (2011). One-Dimensional ZnO Nanostructures: Solution Growth and Functional Properties, *Nano Research*, Volume 4, 11, 1013-1098.
- [6] Yolacan, D., Demirci Sankir, N., (2017). Enhanced Photoelectrochemical and Photocatalytic Properties of 3D-Hierarchical ZnO Nanostructures. *Journal of Alloys and Compounds*, Volume 726, 474-483.
- [7] Verges, M., A., Nifsud, A., Serna, C., J., (1998). Formation of Rod-like Zinc Oxide Microcrystals in Homogeneous Solutions, *Journal of the Chemical Society*, Faraday Transactions, 24, 3527-3780.
- [8] Laudise, R., A., Ballman, A., A., (1960). Hydrothermal Synthesis of Zinc Oxide and Zinc Sulfide, *J. Phys. Chem*, Volume 64, 5, 688-691.
- [9] Lin, D., D., Wu, H., Pan, W., (2007). Photoswitches and Memories Assembled by Electrospinning Aluminum-Doped Zinc Oxide Single Nanowires, *Advanced Materials*, Volume 19, 22, 3968-3972.
- [10] Xu, C., Xu, G., Liu, Y., Wang, G., (2002). A Simple and Novel Route for the Preparation of ZnO Nanorods, *Solid State Communications*, Volume 122, 175-179.
- [11] Chiou, W.-T., Wu, W.-Y., Ting, J.-M., (2013). Growth of Single Crystal ZnO Nanowire Using Sputter Deposition, *Diamond and Related Materials*, Volume 12, 10-11, 1841-1844.
- [12] Hong, J-II., Bae, J., Wang, L., Z., Snyder, R., L., (2009). Room-Temperature, Texture-Controlled Growth of ZnO Thin Films and Their Application for Growing Aligned ZnO Nanowire Arrays, *Nanotechnology*, Volume 20, 8, 085609.
- [13] Heo, Y., W., Varadaeajan, V., Kuafman, M., Kim, K., Nortona, D., P., (2002). Site-Specific Growth of ZnO Nanorods Using Catalysis-Driven Molecular Beam Epitaxy, *Applied Physics Letter*, Volume 81, 16, 3046-3048.
- [14] Yuan, H., Zhang, Y., (2004). Preparation of well-Alligned ZnO Whiskers on Glass Substrate by Atmospheric MOCVD, *Journal of Crystal Growth*, Volume 263, 119-124.
- [15] Yao, B., D., Chen, Y., F., Wang, N., (2002). Formation of ZnO Nanostructures by A Simple Way of Thermal Evaporation, *Applied Physics Letter*, Volume 81, 4, 757-759.

- [16] Wu, J.-J., Wen H.-I., Tseng, C.-H., Liu, S., C., (2004). Well-Aligned ZnO Nanorods Via Hydrogen Treatment of ZnO Films, *Advanced Functional Materials*, Volume 14, 8, 806-810.
- [17] Xu, S., Wei, Y., Kirkham, M., Liu, J., Mai, W., Davidovic, D., Snyder, R., L., Wang, Z., L., (2008). Pattern Growth of Vertically Aligned ZnO Nanowire Arrays on Inorganic Substrates at Low Temperature Without Catalyst, *J. Am. Chem. Soc.*, Volume 130, 45, 14958-14959.
- [18] Xu, S., Adiga, N., Ba, S., Dasgupta, T., Wu, C., F., J., wang, L., Z., (2009). Optimizing and Improving the Growth Quality of ZnO Nanowire Arrays Guided by Statistical Design of Experiments, *Acs Nano*, Volume 3, 7, 1803-1812.
- [19] Tyona, M., D., Osuji, R., U., Ezena, F., I., (2013). A review of zinc oxide photoanode films for dye-sensitized solar cells based on zinc oxide nanostructures, *Advanced in Nano Research*, Volume 1, 1, 43-58.
- [20] Jiang, C., Y., Sun, W., X., Lo, Q., G., Kwong, D., L., (2007). Improved Dye-sensitized solar Cells with A ZnO-Nanoflower Photoanode, *Applied Physics Letter*, Volume 90, 263501.
- [21] Gong, M., Xu, X., Yang, Z., Liu, Y., Liu, L., (2010). Structure, Photoluminescence and Wettability Properties of Well Arrayed ZnO Nanowires Grown by Hydrothermal Method, *J Nanosci Nanotechnol*, Volume 10, 11, 7762-7765.
- [22] Farooq, M., H., Aslam, I., Anam, H., S., Tanveer, M., Ali, Z., Ghani, U., Boddula, R., (2019). Improved photocatalytic performance of reduced zinc oxide (ZnO) novel morphology of astray like microstructure under solar light irradiation, *Material Science for Energy Technologies*, Volume 2, 2, 181-186.
- [23] Wang, Y., Chen, X., Zhang, J., Sun, Z., Li, Y., Zhang, K., Yang, b., (2008). Fabrication of Surface-Patterned and Free-Stanbding ZnO Nanobowls, *Colloids and Surfaces A: Physicochem. Eng Aspects*, Volume 329, 184-189.
- [24] Kong, Y., X., Wang, Z., L., (2003). Spontaneous Polarization-Induced Nanohelices, Nanosprings, and Nanorings of Pizeoelectric Nanobelts, *Nano Letter*, Volume 3, 12, 1625-131.
- [25] Kaur, M., Kailasaganapathi, s., Rangir, N., Datta, N., Kumar, S., Debnath, A., K., Aswal, D., K., Gupta, S., K., (2016). Gas Dependent Sensing Mechanism in ZnO Nanobelt Sensor, *Applied Surface Science*, Volume 394, 259-266.
- [26] Peng, Y., Bao, L., (2008). Controlled-Synthesis of ZnO Nanorings, *Frontiers of Chemistryin China*, Volume 3, s, 458-463.
- [27] Xiang, W., Wei, C., Feng-Yu, q., (2009). Spontaneous Formation of Single Crystal ZnONanohelices, *Chinese Physics B*, Volume 18, 4, 1669-1675.
- [28] Panda D., Tseng, T., Y., (2013). One-Dimensional ZnO Nanostructures: Fabrication, Optoelectronic Properties, and Device Applications, *J Mater Sci*, Volume 48, 6849-6877.
- [29] Wang, X., Summers, C., J., Wang, Z., L., (2004). Large-Scale Hexagonal-Patterned Growth of Aligned ZnO Nanorods for Nano-Optoelectronics and Nanosensor Arrays, *Nano Letters*, Volume 4, 3, 423-426.
- [30] Djurisic, A., B., Chen, X., Leung, Y., H., Chin Ng, A., M., (2012). ZnO Nanostructures: Growth, Properties and Applications, *J. Mater. Chem.* Volume 22, 6526.
- [31] Feng, X., Feng, L., Jin, M., Zhai, J., Jiang, L., Zhu, D., (2004). Reversible Super-Hydrophobicity to Super-Hydrophilicity Transition of Aligned ZnO Nanorod Films, *J. Am. Chem. Soc.* Volume 126, 1, 62-63.

- [32] Hung, C., H., Whang, W., T., (2004). Low-TEMPERATURE solution Approach Toward Highly Aligned ZnO Nanotip Arrays, *Journal of Crystal Growth*, Volume 268, 242-248.
- [33] Matsuu, M., Shimada, S., Masuva, K., Hirano, S., Kuwabara, M., (2006). Formation of Periodically Ordered Zinc Oxide Nanopillars in Aqueous Solution: An Approach to Photonic Crystals at Visible Wavelengths, *Advanced Material*, Volume 18, 12, 1617-1621.
- [34] Mahalingam, T., Lee, M., K., Park, K., H., Lee, s., Ahn, Y., Park, J., Y., Koh, K., H., (2007). Low temperature Wet Chemical Synthesis of Good Optical Quality Vertically Aligned Crystalline ZnO Nanorods, *Nanotechnology*, Volume 18, 3, 35606-35611.
- [35] Sun, X., W., Wang, J., X., (2008). Fast Switching Electrochromic Display Using a Viologen-Modified ZnO Nanowire Array Electrode, *Nano Lett.* Volume 8, 7, 1884-1889.
- [36] Ko, S., H., Park, I., Pan, H., Misra, N., Rogers, M., S., Grigoropoulos, C., P., Pisano, A., P., (2008). ZnO Nanowire Network Transistor Fabrication on a Polymer Substrate by Low-Temperature, All-Inorganic Nanoparticle Solution Process, *Applied Physics Letters*, Volume 92, 154102.
- [37] Al-Hilli, S., Willander, M., (2007). ZnO Nanorods As An Intracellular Sensor for pH Measurements, *Journal of Applied Physics*, Volume 102, 084304.
- [38] Hong, K., S., Xu, H., Konishi, H., Li, X., (2010), direct Water Splitting Through Vibrating Piezoelectric Microfibers in Water, *J. Phys. Chem, Lett.* Volume 1, 6, 997-1002.
- [39] Gaponik, N., Talapin, D., V., Rogach, L., Hoppe, K., Shevchenko, E., V., Kornowski, A., Eychmuller, A., Weller, H., (2002). Thiol-Capping of CdTe Nanocrystals: An Alternative to Organometallic Synthetic Routes, *J. Phys. Chem. B*, Volume 106, 7177-7185.
- [40] Caruso, F., (2003). Colloids and Colloid Assemblies: Synthesis, Modification, Organization and Utilization of Colloid Particles, *Wiley*.
- [41] Jana, D., Vojtech, A., Rene, K., Jaromir, H., (2009). Quantum Dots- Characterization, Preparation and Usage in Biological Systems, *Int. J. Mol. Sci*, Volume 10, 656-673.
- [42] Kulkarni, S., A., Mhaisalkar, S., G., Methews, N., Boix, P., P., (2018). Perovskite Nanoparticles: Synthesis, Properties, and Novel Applications in Photovoltaics and LEDs, *Small Methods*, Volume 3, 1, 1800231-1800247.
- [43] Zhang, w., Eperon G., E., Snaith, H., J., (2016). Metal Halide Perovskites for Energy Applications, *Nat Energy* 1, 16048.
- [44] Dou, L., yang, Y., M., You, J., Hong, Z., Li, G., Yang, Y., (2014). Solution-Processed Hybrid Perovskite Photodetectors with High Detectivity, *Nature Comm* 5, 5404.
- [45] Chen, Q., Marco D., N., Yang, Y., M., Song, T., B., Chen, C., C., Zhao, H., Hong, Z., Zhou, H., Yang, y., (2015). Under the Spotlight: The Organic-Inorganic Hybrid Halide Perovskite for Optoelectronic Applications, *Nano Today*, Volume 10, 355-396.
- [46] Tan. Z., K., Moghaddam, R., S., Lai, M., L., Docampo, P., Higler, R., Deschler, F., Price, M., Sadhanala, A., Pazos, L., M., Credginton, D., Hanusch, F., Bein, T., Snaith, H., J., Friend, R., H., (2014). Bright Light-Emitting Diodes Based on Organometal Halide Perovskite, *Nature Nanotech* 9, 687-692.
- [47] Fujishima, A., Honda, K., (1972). Electrochemical Photolysis of Water at a Semiconductor Electrode, *Nature* 238, 37-38.

- [48] **Hisatomi, T., Kubota, J., Domen, K.,** (2014). Recent Advanced in Semiconductors for Photocatalytic and Photoelectrochemical Water Splitting. *Chem. Soc. Rev.*, Volume 43, 7520.
- [49] **Ezekoye, B., A., Offor P., O., Ezekoye, V., A., Ezeme, F., I.,** (2013). Chemical Bath Deposition Technique of Thin Film: A Review, *International Journal of scientific Research*, Volume 2, 8, 452-456.
- [50] **Djelloul, A., Adnane, M., Larbah, Y., Zerdali, M., Zegadi, C., Messaoud, A.,** (2016). Effect of Annealing on the properties of Nanocrystalline CdS Thin Film Prepared by CBD Method, *Journal of Nano and electronic Physics*, Volume 8, 2, 02005-02012.
- [51] **Soonmin, H., Tahir, M., B.,** (2019). Preparation of Thin Films by SILAR and Spin Coating Method, *Euroasian Journal of Analytical Chemistry*, 165-172.
- [52] **Franinovic, M.,** (2012). X-ray Photoelectron Spectroscopy, University of Ljubljana, 1.



## CURRICULUM VITAE

### Personal Information

Surname, name : FARAJI, Mehrdad  
Citizenship : IRAN  
Date and place of birth : 13.12.1989 IRAN (TABRIZ)  
Marital Status : Divorced  
Telephone : 0 (551) 385 21 89  
e-mail : [mfaraji@etu.edu.tr](mailto:mfaraji@etu.edu.tr)

### Education

Degree	Information	Grad. Date
Master of Science	TOBB Univ. of Economics and Technology	2020
Master of Science	Istanbul Technical University	2018
Bachelor of Science	Islamic Azad University of Ahar	2011

### Foreign Language

Azari (Native)  
Persian (Native)  
English (Fluent)  
Turkish (Fluent)

### Conference

**Demirci Sankir, N., Tuc Altaf, C., Faraji, M., Sankir, M.,** (2019). Lead halide perovskite-3D ZnO based photoelectrodes design for photoelectrochemical water splitting process, E-MRS conference.